FRIEDRICH-SCHILLER-UNIVERSITÄT JENA

Tuning the Corona: Core Ratio of Polyplex Micelles for Selective Oligonucleotide Delivery to Hepatocytes or Hepatic Immune Cells

---

Dissertation

zur Erlangung des akademischen Grades

Doktor der Philosophie (Ph.D.)

vorgelegt dem Rat der Medizinischen Fakultät

der Friedrich-Schiller-Universität Jena

von M.Eng. Wan Ling Foo

geboren am 25.12.1986 in Johor, Malaysia.

GUTACHTER

Prof. Dr. med Michael Bauer

Prof. Dr. rer. nat Britta Qualmann

Prof. Christoph Thiemermann, MD Ph.D.

Tag der öffentlichen Verteidigung: 6 September 2022

Abstract

Targeted delivery of oligonucleotides or small molecular drugs to hepatocytes, the liver's parenchymal cells, is challenging due to the highly efficient reticuloendothelial system (RES) of the liver mainly comprised of Kupffer cells (KC) and specialized sinusoidal endothelial cells (LSEC), efficiently clearing nanocarriers depending on their size and surface properties. Physiologically this non-parenchymal shield protects hepatocytes; these local barriers are, however, unwanted for drug/gene delivery and need to be overcome. The structural properties of nanocarriers such as surface properties, charges, and size strongly influence tissue penetration, *in vivo* pharmacokinetics, and biodistribution profile.

 In this study, we investigated the effect of PEG density, as defined in corona: core ratio (CCR), of a siRNA polyplex micelles in affecting their efficiency in cellular uptake, gene silencing, hepatocytes targeting accumulation and their elimination route. Four polyplex micelles (EN14, EN15, EN60, and EN76) with different corona: core ratio (CCR) were prepared by polyion complexation between small interfering (si)RNA and diblock copolymer polyethylene glycol (PEG)-*b*-poly-allyl-glycidyl ether (PAGE). Raman spectroscopy was carried out to analyse and validate of the CCR and *in silico* dissipative particle dynamic (DPD) simulation techniques was performed to visualize0 the structural morphology of all the siRNA polyplex micelles.

The overall results strongly suggest that modification of the surface properties, in this case, CCR of polyplex micelles significantly alters the cell type-specific uptake in the liver and eventually leads to different elimination routes. Higher CCR polyplex micelles (EN15) allowed the formation of a stable, thick, and intact PEG shell, protecting them from nonspecific uptake *in vivo*, resulted in higher passive accumulation in hepatocytes while avoiding local and systemic RES. On the contrary, polyplex micelles with lower CCR values (EN60 and EN76) displayed a thin and disrupt PEG shell, leading to easy recognition by immune cells. Furthermore, to overcome the limitation of a small field of view by conventional fluorescent microscopy, we developed a new mesoscopy imaging technique to visualise the siRNA polyplex micelles by providing high resolution and detailed anatomical images on whole mice cross-section. The

elimination route of the polyplex micelles were then determined and quantified. The result again supported the finding from intravital microscopy (IVM); high CCR micelles (EN15) preferably follow the hepatobiliary route, confirming the uptake by hepatocytes.
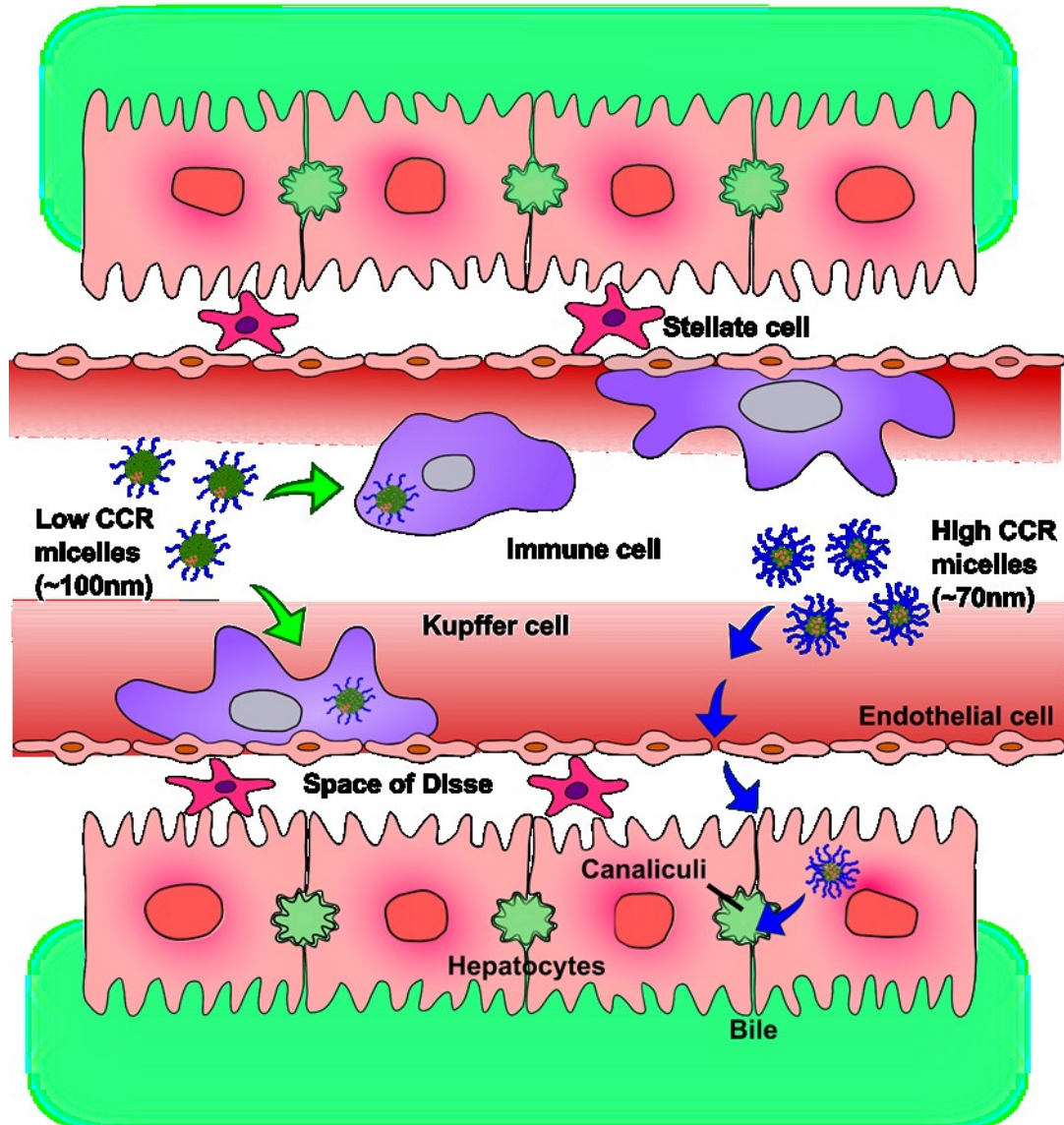
Abstract Figure I. The corona: core ratio (CCR) of siRNA polyplex micelles significantly altered the distribution and uptake profile in the liver. High CCR polyplex micelles with smaller diameter (~70 nm) were protected from taking up by circulating immune cells and Kupffer cells, effectively accumulated in the hepatocytes and eventually eliminated into bile. While polyplex micelles with lower CCR with slightly larger size (~100 nm) were easily recognized and taken up by the circulating immune cells and Kupffer cells in the liver.

Zusammenfassung

Die gezielte Verabreichung von Oligonukleotiden oder niedermolekularen Arzneimitteln in Hepatozyten, die parenchymalen Zellen der Leber, ist eine große Herausfoderung für die moderne Medizin, da das hocheffiziente retikuloendotheliale System (RES) der Leber, bestehend aus Kupffer-Zellen (Kupffer cells, KC) und spezialisierten sinusoidalen Endothelzellen (Liver sinusoidial endothelial cells, LSEC) besteht, Wirkstoffträger in Abhängigkeit von Größe und Oberflächeneigenschaften effizient eliminiert. Durch diesen Mechanismus schützt das RES wie ein Schild die nicht-parenchymalen Hepatozyten vor zum Beispiel Pathogenen wie Viren oder Baktiern. Diese lokale Barriere zu überwinden ist jedoch für die Verabreichung von Nanopartikeln beladen mit Wirkstoffen oder genetischem Material eine Hürde und muss überwunden werden. Die strukturellen Eigenschaften von Wirkstoffträgern wie Oberflächeneigenschaften, Ladungen und Größe beeinflussen stark die Gewebepenetration, die Pharmakokinetik, sowie die Verteilung im Organismus und den Zellen innerhalb eines Organs.

In dieser Arbeit ist die Auswirkung der Oberflächenbeschichtung durch Polyethylenglycol, ein Molekül das die Interaktion zwischen Wirkstoffträgern und dem RES vermindert, an Mizellen zum Transport von Oligoribonukleinsäuren (hier 22 nukleotidlanger, doppelsträngiger short interfering (si)RNA) untersucht. Die Mizellen bestehen dabei aus einem Polmyer mit zwei miteinander verbundenen Blöcken: der Oberfläche (Corona) aus PEG und einem angehängten geladenen Block aus - Polyallyl-Glycidylether (PAGE) (Core) zur Komplexierung der siRNA. Durch die Synthese verschiedener Polymere wird das Corona:Core-Verhältnis (CCR) systematisch variiert und der Transport von siRNA-Polyplexmizellen auf die Effizienz bei der Zellaufnahme, dem Gen-Silencing durch die siRNA eines Reportergens, der Akkumulation in den Hepatozyten und ihrem Ausscheidungsweg hin erforscht. Vier Polyplex-Mizellen (EN14, EN15, EN60 und EN76) mit unterschiedlicher CCR wurden durch Polyionenkomplexierung zwischen kleiner interferierender (si)RNA und dem Diblock-Copolymer Polyethylenglykol-b-Polyallyl-Glycidylether hergestellt. Die Raman-Spektroskopie validierte die CCR und wurde zur Charakterisierung der Oberfläche verwendet und mit *in silico* Simulationstechniken der dissipativen

Partikeldynamik (DPD) korreliert, um die Morphologie aller siRNA-Polyplexmizellen zu visualisieren.

Die Ergebnisse zeigen, dass die Modifikation der Oberflächeneigenschaften, in diesem Fall der CCR von Polyplexmizellen, die zelltypspezifische Aufnahme in der Leber erheblich verändert und schließlich zu unterschiedlichen Eliminationswegen führt. Polyplexmizellen mit höherem CCR (EN15) ermöglichten die Bildung einer stabilen und durchgängigen PEG-Hülle, die sie vor unspezifischer Aufnahme *in vivo* schützt und zu einer höheren passiven Akkumulation in Hepatozyten führte, während eine Interaktion mit den Zellen des RES vermieden wurde. Im Gegensatz dazu wiesen Polyplexmizellen mit niedrigeren CCR-Werten (EN60 und EN76) eine dünne und unterbrochene PEG-Hülle auf, wodurch es vermehrt zu einer Erkennung und Aufnahme in zellen des RES kam. Zusätzlich wurde, durch ein in dieser Arbeit entwickeltes mesoskopisches Fluoreszenzbildgebungsverfahren, der Eliminationsweg der Polyplexmizellen bestimmt und quantifiziert. Das Ergebnis bestätigte erneut, dass die Mizellen mit hohem CCR-Gehalt (EN15) folgen vorzugsweise dem hepatobiliären Weg, was die Aufnahme durch Hepatozyten bestätigt.

Abbreviations

^{1}H-NMR	Proton nuclear magnetic resonance
AGE	Allyl glycidyl ether (AGE)
Ago	Argonaute
APC	Allophycocyanin
AUC	Area under curve
bp	Basepairs
BW	Bodyweight
CaH_2	Calcium hydride
CCD	Charge-coupled device
CCR	Corona: core ratio
COOH	Carboxylic group
CT	Computed tomography
Cy3	Cyanines 3
Cy5	Cyanines 5
DLS	Dynamic light scattering
DMAc	Dimethylacetamide
DMEM	Dulbecco's Modified Eagle's Medium
DMPA	2,2-dimethoxy-2-phenylacetophenone
DMSO	Dimethyl sulfoxide
DNA	Deoxyribonucleic Acid
DOX	Doxorubicin
Dp	Degree of polymerization
DPD	Dissipative particle dynamics
DPPE	1,2-Dipalmitoyl-sn-glycero-3-phosphoethanolamine
ds	Double stranded
dsRNA	Double stranded RNA
EC	European Commission
EDTA	Ethylenediaminetetraacetic acid
EPR	Enhanced permeability and retention effect
EtBr	Ethidium Bromide
FBS	Fetal bovine serum

FDA	United States Food and Drug Administration
FI	Fluorescent intensity
FITC	Fluorescein isothiocyanate
FLD	Fatty Liver Disease
FoV	Field of view
GDB	Global Burden of Diseases, Injuries, and Risk Factors Study
GRA	Gel retardation assay
h	Hours
HBV	Hepatitis B virus
HCC	Hepatocellular carcinoma
HEPES	(4-(2-hydroxyethyl)-1-piperazineethanesulfonic acid)
HSC	Hepatic stellate cells
INT	Iodonitro- tetrazolium violet
IVIS	*In vivo* imaging system
IVM	Intravital microscopy
KC	Kupffer cells
KCl	Potassium chloride
KH	Potassium hydride
LB	Lysis buffer
LDH	Lactate dehydrogenase
LSEC	Liver sinusoidal endothelial cells
MD	Molecular dynamics
MeOH	Methanol
MgCl$_2$	Magnesium chloride
min	Minutes
miRNA	MicroRNA
M$_n$	Number average of molecular weight
MPS	Mononuclear phagocytic system
MRI	Magnetic resonance imaging
MS	Materials Studio 2020
MSOT	Multispectral optoacoustic tomography
M$_w$	Molecular weight
N/P ratio	Amine/phosphate ratio

NA	Numerical aperture
NAD(P)H	Dihydronicotinamide-adenine dinucleotide phosphate
NAFLD	Nonalcoholic fatty liver disease
NaH	Sodium hydride
NH$_2$	Anime group
NIR	Near-infrared range
PAGE	Poly(allyl-glycidyl-ether (AGE))
PBS	Phosphate-buffered saline
PC	Principle component
PCA	Principle component analysis
Pd	Pharmacodynamic
PDI	Polydispersity index
pDNA	Plasmid DNA
PEG	Poly (ethylene glycol)
PEG-b-PAGE	Poly(ethylene glycol)-*block*-poly(allyl glycidyl ether)
Pen/Strep	Penicillin Streptomycin
Pk	Pharmacokinetic
PLys	Polylysine
Ppm	Parts-per-million
RES	Reticuloendothelial system
RISC	RNA-induced silencing complex
RNAi	RNA interference
ROI	Regions of interest
Rpm	Revolutions per minute
RT-qPCR	Reverse-transcription quantitative polymerase chain reaction
SD	Standard deviation
SDS-PAGE	Sodium dodecyl sulphate polyacrylamide gel electrophoresis
SEC	Size exclusion chromatography
shRNA	Short hairpin RNA
siRNA	Small interfering ribonucleic acid
SNIP	Sensitive non-linear iterative peak
ssRNA	Single stranded RNA
TAE	Tris-acetate-EDTA

TEM	Transmission electron microscopy
THF	Tetrahydrofuran
TLR4	Toll-like receptor 4
TLRs	Toll-like receptors
UV	Ultraviolet
v/v	Volume per volume
w/v	Weight per volume

Contents

1.   Introduction

1.1   Liver

1.1.1 Organ structure and functionality

The liver, comprising the vast majority of the reticuloendothelial system (RES) in the human body, consists of various types of cells descending from the monocytes that can sequester and excrete 30 to 99% of all nanoparticles systemically administered. (Wang et al. 2015) Liver is also the largest organ in the body engaged with an enormous number of functions, including exhibiting synthetic (Wolf 1999), blood haemostasis (Trefts et al. 2017), immunology (Abe et al. 1988), metabolism (Gebhardt 1992, Jungermann and Kietzmann 1996) and excretory function (Mitra and Metcalf 2012). The liver is composed of various cell types, such as the parenchymal cell, *i.e.,* hepatocytes and the non-parenchymal cell, including Kupffer cells (KC), liver sinusoidal endothelial cells (LSEC), and hepatic stellate cells (HSC). (Trefts et al. 2017) Each cell type possesses unique functions that cooperatively regulate hepatic function at multiple levels. The liver structure is formed by repeating functional units, lobules in a typically hexagonal shape around the central vein (Figure 1.1). The parenchymal cells arranged in the linear cord, surrounded by the branches of the hepatic artery and portal vein, together with the non-parenchymal cells along the sinusoidal tracts, composes the lobules' structure. The nutrient blood from the portal vein and oxygen-rich blood from the hepatic artery mix in the sinusoid and flow through the cells in the lobule, eventually accumulates into the central vein and leaves the liver through hepatic veins.

Hepatocytes make up 70-85% of the liver cell mass and are responsible for many vital metabolic, endocrine, and secretory functions. These parenchymal cells are often the primary cellular target in treating various kinds of liver diseases. Hepatocytes are separated from the sinusoids by the space of Disse. The liver sinusoid networks are formed by fenestrated capillaries with 5 to 10 μm wide between the linear cords of hepatocytes. (Abe et al. 1988) Liver sinusoidal endothelial cells (LSEC) aligned along the sinusoid are specialized endothelial cells with fenestration pores ranging from 50–

280 nm in mice/rats and 50–180 nm in humans. This characteristic allows the exchange of plasma components within these size limits with various cells o the liver in the space of Disse while still maintaining necessary barrier functions. (Wisse et al. 2008)

Kupffer cells are the macrophages in the liver localized in the lumen of liver sinusoids. Kupffer cells are the most significant component of the resident mononuclear phagocytic system (MPS) in the body and play an essential role in hepatic response towards pathogens and foreign agents. (Dixon et al. 2013) Kupffer cells exhibit the innate immunology response in the liver and are central to remove foreign nanoparticles regardless of size from the organ. (Sadauskas et al. 2007)

Finally, other non-parenchymal cells like hepatic stellate cells (HSCs), located in the space of Disse, are essential in the liver. HSC is activated during liver damage and subsequently secreting collagen to form scar tissue, leading to fibrosis or cirrhosis. Thus HSC is the leading therapeutic target site for treating liver fibrosis. (Beljaars et al. 2002)
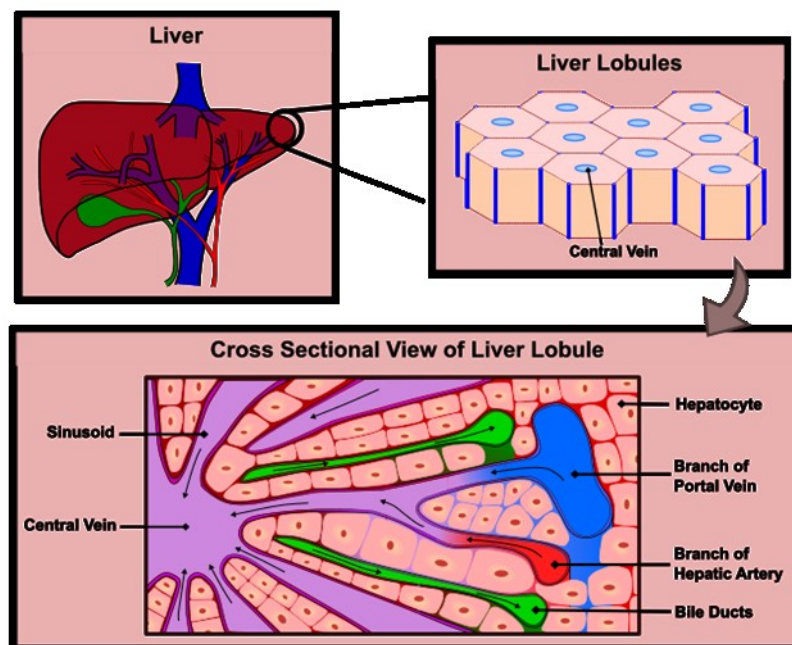

Figure 1.1. The architecture of the liver. Liver consists of repeating unit, lobules in hexagonal shapes around the central vein. In lobules, hepatocytes residues along the linear cord are surrounded by branches of nutrient-rich portal vein and oxygen-rich hepatic artery. The blood from the portal vein and hepatic artery mix in the sinusoid, flow through the different cells in the lobule, accumulate in the central vein, and leave the body through hepatic veins.

1.1.2 Liver disease and therapy

According to the report of the Global Burden of Diseases, Injuries, and Risk Factors Study (GBD) 2017, which develops since 1990, by age, gender, and cause, for 195 countries and territories, cirrhosis and other chronic liver diseases has become a leading aetiology of morbidity and mortality worldwide. (GBD 2018) End-stage diseases such as cirrhosis, life-threatening infections (sepsis), and hepatocellular carcinoma (HCC) contributed to the high mortality rate of liver diseases. (Asrani et al. 2019) Based on the GBD 2017 report, cirrhosis resulted in deaths increased from 1.9% in 1990 to 2.4% of total deaths globally in 2017, approximately1.32 million death annually. (GBD 2018, Marcellin and Kutala 2018, Sepanlou et al. 2020).

Cirrhosis is a late stage of liver fibrosis caused by several mechanisms of liver damage due to various forms of liver disease. Cirrhosis is clinically considered a terminal illness that is invariably leading mortality unless liver transplantation is done. (Tsochatzis et al. 2014) The transition from chronic liver disease to cirrhosis often involves inflammation, fibrogenesis due to activation of hepatic stellate cells, and extinction lesions of parenchymal cells. (Wanless et al. 1995) Several different types of liver diseases are induced by different pathology, for example, hepatitis caused by a virus (main Hepatitis B, HBV) and inherited metabolism diseases such as hypercholesteremia or Wilson disease. In addition, an overdose of drugs, poisons, and overconsumption of alcohol may also lead to a certain level of liver injury, results in hepatic steatosis (fatty liver disease FLD) and non-alcoholic fatty liver disease (NAFLD). Therefore, to prevent or delay liver disease progression into chronic cirrhosis, understand the leading cause of the liver disease and develop appropriate treatment adapted to different types of liver disease remains challenging and worth investigating.

As mentioned in the previous section, numerous liver functions are carried out by parenchymal and non-parenchymal cells, either alone or in cooperation, depending on each function. Delivery of drugs to the liver is challenging because any therapeutic agent that circulated in the blood can only expose to the liver cells with a short duration 9 seconds to minutes). (Huang et al. 2011) Foreign substances that intravenously

injected are instantly filtered by the liver local RES, uptake by the hepatic immune cells, KC or metabolized into nontoxic form, thus losing the therapeutic effect. In consequence, treating patients with chronic liver diseases often apply prolonged treatment with medication. Lacking cell type-specific delivery of the therapeutic agents into the liver limited the drug's effectiveness and may induce unwanted hepatoxicity. Therefore, effective targeted drug delivery platforms are urgently needed to improve drug concentration at the desired site and reduce the off-target drug distribution. (Böttger et al. 2020)

1.2   RNA interference (RNAi) therapy

RNA interference (RNAi) therapy is a therapeutic platform involved in sequence-specific suppression of disease-related gene expression with RNAi modalities, *e.g.* small interfering RNA (siRNA) and microRNA (miRNA). Both RNAs knockdown the expression of the target gene by promoting degradation of the targeted mRNA degradation. siRNA exhibit more efficient and specific gene silencing than miRNA, while one miRNA can simultaneously suppress the expression of several different target genes. (Hu et al. 2020) During the gene silencing pathway, siRNA with only 21-23 nucleotides generally reacts in the cytoplasm after endocytosis. siRNA recruits one or more Argonaute (Ago) proteins and form the enzyme-containing intermediate complex known as RNA-induced silencing complex (RISC) (Figure 1.2). The assembly of RISC leads to an unwinding of the double-stranded siRNA and a stable association between the guide strands (one of the strands) with the Ago effector protein. The guide strands lead the RISC to the complementary RNA target by canonical Watson-Crick base pairing. RISC cleaves the mRNA by endonuclease Ago2, blocking mRNA translation, further degrading the mRNA fragments. (Carthew and Sontheimer 2009)
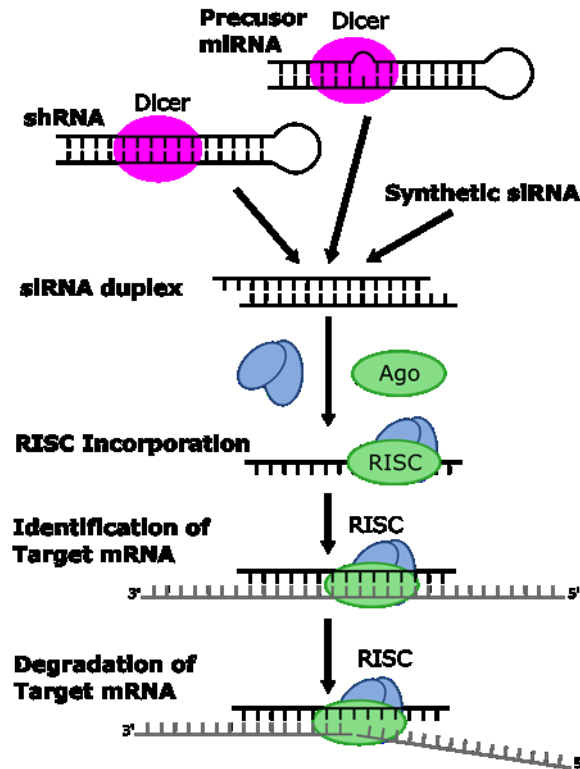
Figure 1.2. The gene interference mechanism of small interfering RNA (siRNA). Precursor microRNA (miRNA) and short hairpin RNA (shRNA) are processed by endonuclease Dicer into short siRNA duplex. siRNA duplex or synthetic siRNA forms RNA-induced silencing complex (RISC) with the helps of Argonaute (Ago) proteins. Ago proteins cleave the sense strands, and active RISC incorporated with antisense is formed. The active RISC identify the target mRNA, followed by cleaving the mRNA, blocking the mRNA translation. Eventually, cleaved mRNA fragments lead to degradation, and the target gene is silenced.

The research on RNAi was first established 20 years ago, providing potential diseases treatment alternatives through silencing the specific target disease gene. The first successful gene silencing on various mammalian cells was achieved in 2001 by Tuschl et al., significantly endorsing the potential of siRNA in disease treatment. (Elbashir et al. 2001) Finally, the development of siRNA therapy had achieved a new era in 2018 when the first the United States Food and Drug Administration (FDA) and the European Commission (EC) approved Alnylam® Pharmaceuticals launched commercial RNAi drug, ONPATTRO® (Patisiran, ALN-TTR02). (Akinc et al. 2019) This drug has proven its safety and effectiveness in treating an adult with polyneuropathies induced by inherited transthyretin amyloidosis. Soon after the great success, another two siRNA-based drugs, Givosiran (Scott 2020), treat acute hepatic

porphyria and Lumasiran for primary hyperoxaluria type 1 (Scott and Keam 2021), also received the approval from FDA. To date, there are still several siRNA drugs undergoing the phase 3 clinical trials and approaching FDA approval. (Zhang et al. 2021)

Even though siRNA possesses excellent potential in therapeutic modality, the development remains challenging due to the unsatisfactory stability and poor pharmacokinetic behaviour of naked and unmodified siRNA. Moreover, the delivery of siRNA towards a specific target site, overcoming the intracellular and extracellular barrier, and avoiding possible off-target effects are also issues in advancing the therapeutic effectiveness of siRNA. (Whitehead et al. 2009)

Theoretically, RNAi therapy can silence any gene of interest as long as the correct nucleotide sequences complemented with the target mRNA are chosen. This characteristic makes excellent advantages for siRNA to treat many diseases that cannot cure by small molecule or antibody drugs. Furthermore, RNAi therapy can be administered quarterly or even longer in a year and still maintaining its therapeutic effects, which is not feasible for other antibody or small molecule drugs. (Hu et al. 2020)

1.3   Nanocarriers for oligonucleotide delivery

In gene therapy or oligonucleotide delivery, the therapeutic effect can only be obtained by delivering a therapeutic gene to the target cells followed by an effective release in their target. Oligonucleotides such as siRNA, mRNA, or microRNA express their cytoplasm functionalities while DNA must be delivered into the nucleus for further transcription and translation. Biological substances like oligonucleotides are fragile, could be rapidly digested and eliminated by the immune system in physiological conditions. (Yin et al. 2014) Thus, systemic administrated naked oligonucleotide could hardly achieve cell internalization. An effective delivery system that can encapsulate and protect the foreign therapeutic oligonucleotide from protein interaction and nuclease attack inside the harsh environment of the human body is mandatory. Gene delivery systems are classified into viral and nonviral vectors. A viral vector, literally a

gene carrier derived from a deactivated virus, exhibits excellent cell internalization ability while having an unavoidable drawback of immunogenicity and inflammatory toxicity. Nonviral vectors, carriers fabricated by lipids or polymers, associated with a low immunogenic response, have intensively investigated translational medicine. (Yin et al. 2014) Research and development of lipid and polymeric gene carrier extensive focus on enhancing endocytosis ability, shielding from immune response, and targetability delivery. In between, polymeric nanocarriers that allow versatile modification for specific functionality exhibits high potential in managing the distribution profile and overcoming the biological barriers. (Cabral et al. 2018) Polymeric nanocarriers or polyplex micelles, as well as lipid nanocarriers liposome often modify with poly(ethylene glycol) (PEG) to avoid possible opsonisation, which could facilitate their recognition by the RES. PEGylation on nanomedicines is essential in prolonged blood circulation and protection of the therapeutic cargos. (Owens and Peppas 2006) Fine-tuning the polymeric nanocarriers' physicochemical properties would help achieve tailored release of the therapeutic cargos on the intended site of action.

1.3.1 Barrier challenges and the cargo interaction

Gene therapy is performed via systemic administration, especially in cancer treatment or treating liver diseases in which local delivery is not possible due to unknown and inaccessible sites of action. In this regard, tailoring nanocarriers for oligonucleotide delivery is essential to overcome biological barriers in circulation, such as nuclease attack, opsonisation, excretion, and phagocytosis. Understanding what the biological barriers are during the delivery allows better optimization in designing the nanocarriers. (Mitchell et al. 2021) When the gene carrier enters the bloodstream, the nanocarriers immediately experiences the shear force from the bloodstream. The shear stress in the bloodstream is varied depending on the blood vessels' diameter, *i.e.,* the different flow rates of the blood. (Ballermann et al. 1998) When the nanocarriers are circulating in the blood vessel, the various shear stress may damage the outer shell of the nanocarriers and deteriorate the cargo's integrity, eventually leading to degradation and shorter circulation time. Nanocarriers are exposed to shear stress, absorbing proteins, immune cells, and suspended enzymes. Delivery of the naked

oligonucleotide often encountered the nuclease attack by the enzyme present in the blood and led to degradation before reaching the target site. Any foreign agents or particles entered into the bloodstream contact the opsonin protein and form protein corona. This process, called opsonisation, increases the recognition of the particles towards macrophages and promotes phagocytosis to degrade and remove the foreign agents from the bloodstream. (Owens and Peppas 2006) Nanoparticles with tailored surface modification enhance the blood circulation profile, and better shielding from phagocytes may reduce the opsonisation. Eventually, they are unavoidably circulating in MPS or RES-rich organ, such as liver and spleen. There, the local macrophages, *i.e.,* Kupffer cells, most likely uptake and sequestrated the nanoparticles. (Li et al. 2020) Biodistribution of nanoparticles without target moiety is often passive and highly dependent on the target site's environment. For instance, accumulation of the nanocarriers in tumours can be promoted by the enhanced permeability and retention effect (EPR) results from the abnormal leaky blood vessels. (Cabral et al. 2018) The uptake of the nanocarriers by different tissues is also highly dependent on their physicochemical properties, including size, shape, surface properties, and targeting ligand conjugation. (Zhang et al. 2016)

Therefore, to facilitate an effective delivery toward targeted tissue, the liver in this work, investigation on the effect of physicochemical properties of the siRNA nanocarriers toward biodistribution profile is essential.

1.3.2 Diblock copolymer: Poly(ethylene glycol)-*block*-poly(allyl glycidyl ether) (PEG-*b*-PAGE)

Block copolymers are one of the most researched non-viral vectors for drug and gene delivery since a few decades ago. (Kataoka et al. 2001) In between, diblock copolymers synthesized with PEG and another functionalized polymer have been investigated extensively as a versatile platform for siRNA delivery. (Kataoka et al. 2005) Poly-allyl-glycidyl ether (PAGE) is a biocompatible and biodegradable polymer utilized in combination with PEG in drug and siRNA delivery system. (Wang et al. 2013, Barthel et al. 2014a, Zhang et al. 2015, Rietscher et al. 2016, Cunningham et al. 2020) PAGE is often used as a linker between PEG and another biodegradable polymer like

PLGA, PLA for drug delivery. (Wang et al. 2013, Barthel et al. 2014b, Zhang et al. 2015, Rietscher et al. 2016) The allyl group in allyl-glycidyl ether (AGE) provides a convenient platform for functionalization, such as modification by thiol-ene click reaction to introduce primary amine (NH_2) or carboxylic group (COOH). (Barthel et al. 2012, Wang et al. 2013) Cunningham et al. have reported that siRNA polyplex (153 nm to 200 nm) forming by cholic acid conjugated PAGE-*b*-PEG exhibit an improvement in cell uptake and gene silencing in Hela cells. (Cunningham et al. 2020) Hoang et al. also found a similar result with Guanidinium conjugated PAGE-*b*-PEG siRNA micelles. (Hoang et al. 2020) In addition to siRNA delivery, PAGE has been utilized by several groups in combination with PEG and another polymer to form triblock polymers for delivering the anticancer drug, Doxorubicin (DOX). (Hrubý et al. 2005, Wu et al. 2013, Zhang et al. 2015) By conjugating with different targeting ligands, these research groups were able to demonstrate good drug release and cell profile in 2D cell culture and 3D tumour models.

Even though many research group has published the excellent ability of PEG-*b*-PAGE as a drug/gene delivery system in drug conjugation, drug release, siRNA encapsulation, gene silencing, low cytotoxicity and promising *in vitro* cellular uptake, there is still lacking reports on *in vivo* siRNA delivery by PEG-*b*-PAGE. Thus, it is worth evaluating and discovering this polymer's efficiency in delivering siRNA through systemic injection and biodistribution profile.

1.3.3 Physicochemical effect on nanocarrier's pharmacologic distribution

Compared to liposomes, polymer-based nanocarriers exhibit advantages in their versatility in properties modification. Polymeric nanocarriers can be customized modified into desired functionally based on specific site distribution or targeting delivery requirements. Physicochemical properties of the nanoparticles, such as surface properties, size, and shape, are the critical parameters in influencing the nanoparticles' pharmacokinetics. As mentioned in the previous section, delivery naked siRNA is risky and inefficient due to the nuclease presented in the blood, which degrades the siRNA. The siRNA delivery system platforms recently utilized in the newly FDA approved commercials siRNA drug are lipid nanoparticles with surface

modification of PEG. (Akinc et al. 2019, Scott 2020, Scott and Keam 2021) In the first approved drug, ONPATTRO® (Patisiran, ALN-TTR02), PEGylation was performed on the siRNA liposome with PEG_{2000}-C-DMG [α-(3′-{[1,2-di(myristyloxy) proponoxy] carbonylamino} propyl)-ω-methoxy. (Onpattro 2018, Akinc et al. 2019, Zhang et al. 2021) The PEG surface modification on the lipid nanoparticles assists it from evading the MPS and prolonging circulation time. The ratio of the PEG modification on the lipid nanoparticles is optimized to ensure the delivery to the hepatocytes. PEG surface modifications can create a shielding layer to reduce the recognition by phagocytes. However, too dense or highly grafting of PEG may increase the nanocarriers' size, thus resulting in difficulties for cell internalization and hindering the cargo release. Several works have been reported on plasmid carrier (polyplexes) complexed by PEG-polylysine (PLys) with different lengths of the PLys. (Tockary et al. 2013, Dirisala et al. 2014) The results show that increase PEG crowdedness significantly prolonged the blood retention profile of the polyplexes. Reducing the length of PLys to increase further the PEG crowdedness resulted in a larger particles size over 200 nm and deteriorated the cellular uptake ability and transfection efficiency. Both Fisher *et al.* and Walkey *et al.* introduced PEGylation onto solid inorganic nanoparticles, *i.e.*, gold nanoparticles and quantum dots. They discovered that increasing the PEG density on the nanoparticles' surface inhibits the uptake of the nanoparticles by circulating immune cells and Kupffer cells. (Fischer et al. 2010, Walkey et al. 2012) Moreover, Mosquiera et al. also demonstrated a study on the effect of covalently conjugated PEG on nanocapsules. The results strengthened the theory of PEGylation on reducing the nanoparticle's clearance from the blood and pointed out the importance of fine-tuning the PEG content ratio to alter the distribution. (Mosqueira et al. 2001)

Besides the stealth effect against immune and endothelia cell interactions, PEG surface modification can also protect the cargo from shear stress inside the bloodstream. The works done by this research group indicated that polyplexes would lower PEG density and lose their integrity after encountering higher shear stress. Thicker PEG outer shell worked better in maintaining the intactness of the polyplex. (Takeda et al. 2017b) Recently, Yin *et al.* examined the shear stress effect towards oligonucleotide polyplex with different PEG molecular weights. The researchers

further proved that aggregate and cargo exposure happened when the PEG layer could not form an intact layer. (Yin et al. 2020)

In addition, size is one of the most discussed and important parameters in designing a carrier platform. Pharmacokinetic and distribution of the nanocarriers is to a large extent affected by the size. Different organs possess individual tendencies in taking up the foreign particles in a different size. For instance, large nanoparticles (>200 nm) stand out to the immune system and are rapidly eliminated (Mitchell et al. 2021), while nanoparticles with sizes less than 10 nm are generally accumulated in the kidney and excreted out through urine. In addition, nanocarriers with over 150nm without any targeting moiety are challenging to take up by hepatocytes because the fenestrae pore size of LSECs is around 100 nm-150 nm. Any particles above the range tend to be captured by the resident macrophages, Kupffer cells. (Zhang et al. 2016) Some insights into this hepatic cellular distribution were published by Popielarki *et al*. through investigating nanoparticles with 50 nm and 140 nm, both with and without ligands. Regardless of similar surface charge and targeting moiety, 50 nm nanoparticles are primarily accumulated in hepatocytes whereas, even with conjugated ligands, the counterpart with 140 nm are taken significantly by Kupffer cells. The results showed that nanoparticle size is upfronting the affinity of the ligand towards the receptor target cells. (Popielarski et al. 2005)

Despite easier extravasation due to the EPR effect, the size-dependent distribution of nanoparticles in cancer therapy is still challenging. Nanocarriers for cancer treatment are designed based on the nature and location of the tumour. For instance, treatment for stroma-rich tumours such as pancreatic cancer often required smaller nanoparticles to penetrate through the thick fibrotic layer and reach the target cells. Studies reported on investigating the size-dependent effect of an anticancer drug carrier for pancreatic cancer were carried out. The result strongly suggested that nanoparticles with sub 100 nm exhibit greater penetration ability than the counter larger particles. (Cabral et al. 2011) Despite the effect on distribution, varying size may also influence the pharmacodynamics of the cargo. Nuhn lutz et al. proved that the diameter of the siRNA-loaded nanogel particles greatly influenced their silencing ability. 40 nm nanoparticles possessed a better cellular uptake and gene interference ability than a larger size with 100 nm. 40 nm nanogel particles also show lower

lysosomal accumulation, and thus it can maintain a knockdown over a longer duration. (Nuhn et al. 2014) In combination with the effect of nanoparticles size towards specific accumulation and cargo release, this publication reported the gene transfection and tumour penetration ability of two polyplexes with different sizes and shapes formed by double-stranded (ds) DNA. They denatured single-stranded DNA with the same PEG-PLys platform. dsDNA polyplex with a size of 100 nm in rod shape exhibited better gene transfection efficiency *in vitro*. While, with a smaller size of sub-50 nm, spherical ssDNA polyplex micelles showed significantly higher tumour suppression ability in a thick fibrotic tumour. Smaller and spherical polyplex enhanced the penetration through the fibrotic layer and increase accumulation in the tumour cells, thus leading to a better *in vivo* gene transfection ability. (Tockary et al. 2019)

Both size and shape are crucial in affecting the distribution profile. Several research works have reported that the shape and aspect ratio of the nanoparticles influence the uptake by phagocytic cells. For example, Rod nanoparticles experience more uptake than spherical nanoparticles by macrophages. (Xie et al. 2017) Dias *et al.* further reported that, compared to rod shaped nanoparticles, the spherical gold core-mesoporous silica shell nanoparticles give more homogeneous distribution and better penetration in tumour spheroids model. (Dias et al. 2016) While other researchers found out that macrophages tend to uptake spherical nanoparticles more than their rod counterparts. (Geng et al. 2007, Arnida et al. 2011) even though the finding outcome is varied, all these studies come to a consistent conclusion that the shape of the nanoparticles affects the cellular uptake. The possible reason for distinct outcomes is attributed to the differences in all the other properties of the nanoparticles, *i.e.,* surface charge, size, surface modification, ligand conjugation, and varied target site and administration approach in this study.

Surface charges also play an essential role in varying the uptake of the nanocarriers by immune cells. Oligonucleotide or plasmid nanocarriers (polyplex) often form by complexation between cationic charges polymer and negative charge nucleotides at a certain N/P ratio. Polyplex formed at low N/P ratios carry an almost neutral charge that creates aggregation, while a higher N/P ratio generates more cationic surface charges. Souris et al. have concluded that nanoparticles with positive surface changes increased hepatobiliary clearance kinetic. (Souris et al. 2010) Research has found that

hepatocytes uptake the cationic charged nanoparticles preferably while anionically charged nanoparticles tend to uptake by Kupffer cells. (Cheng et al. 2012) Negatively charged nanoparticles might encounter difficulties in contact with cell surface due to repulsive force. While nanoparticles with highly positive charges may induce cytotoxicity by damaging the cell membrane. (Blanco et al. 2015, Mitchell et al. 2021)
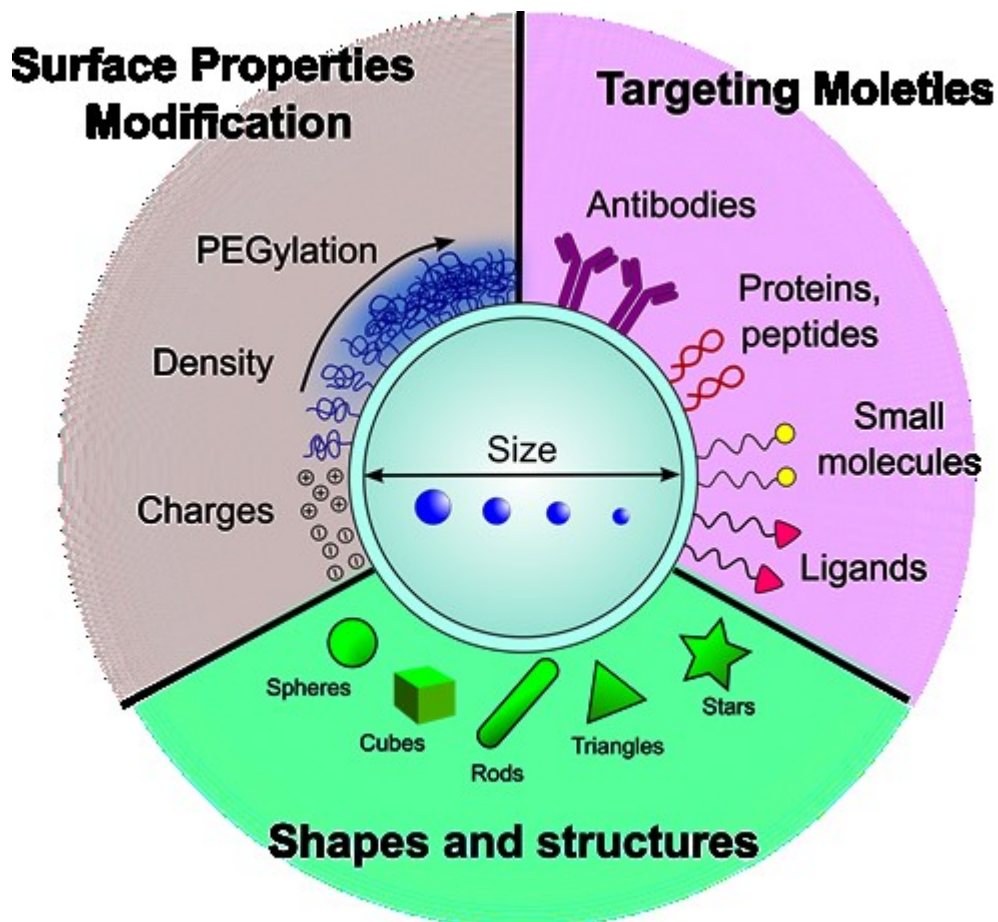

Figure 1.3. Physicochemical properties of nanoparticles. The surface properties, size, shape, and targeting moiety contribute in altering the pharmacologic distribution of nanoparticles. All attributes of nanoparticles can be modified in intelligent designs to facilitate a platform for the specific application. Different combinations of these properties provide numerous permutations of nanoparticles features and platforms.

1.4 Elimination pathway of nanoparticles

Understanding how nanoparticles or foreign agents are eliminated from the body is critical for their clinical application in the drug delivery system. Systemic administrated

drug circulates in the bloodstream until they are degraded and eliminated out from the body. However, excessive accumulation of nanoparticles in the body may induce severe toxicity and inflammation. (Choi et al. 2011) Elimination pathway of injected nanoparticles often follows the hepatobiliary or renal route. Besides, injected foreign agents will also be recognized and remove by the innate immune system.

The liver, being the most significant MPS system in the body, sequesters most foreign nanoparticles. Thus, the hepatobiliary route is a common clearance pathway to eliminated injected drugs. Nanoparticles are taken up by hepatocytes and transported to the bile duct via bile canaliculi, flowing into the gastrointestinal tract and eventually excreted through faeces. (Ogawara et al. 1999) However, non-parenchymal cells in the liver are the primary barrier to prevent nanoparticles from entering the hepatobiliary route. LSEC in the liver has the fenestration pore around 50-180 nm in humans (Wisse et al. 2008); thus, smaller nanoparticles have a better chance to enter into space of Disse and undergo hepatobiliary elimination. Besides, the resident macrophages Kupffer cells can also identify and take up the nanoparticles, further blocking the nanoparticles in accessing Disse's space and taking up by hepatocytes. (Poon et al. 2019) Thus, nanoparticles with better stealth effect against Kupffer cells and LSEC may increase the uptake in hepatocytes and better facilitate hepatobiliary clearance. Fine-tuning the physicochemical properties of nanocarriers enables researchers to alter the distribution in the liver.

Furthermore, the conjugating targeting moiety can also alter the clearance pathway of nanoparticles. Press et al. have shown that the elimination of nanoparticles can be altered by conjugated with different dyes. (Press et al. 2017a)

Another common elimination pathway of nanoparticles is renal clearance through glomerular filtration in the kidney and urine excretion from the body. Researchers have found that nanoparticles smaller than 5.5 nm eliminate rapidly through the renal route due to the filtration pore size limit in glomerular of 8 - 10 nm. (Choi et al. 2007, Du et al. 2018, Poon et al. 2019) However, this is not always the case. Several researcher groups have discovered the accumulation of nanoparticles in kidneys with a size above 60 nm. (Choi et al. 2011, Zuckerman et al. 2012, Zuckerman and Davis 2013, Guo et al. 2017, Wang et al. 2019b) First, Choi et al. have discovered that, even though

PEGylated gold particles with a size around 75 nm did not pass through pore size limit of glomerular capillaries, the nanoparticles significantly accumulate in the mesangial cell of the kidney. (Choi et al. 2011) Zuckerman et al. further proved transient accumulation in the glomerulus of siRNA encapsulated nanocarriers assembled by electrostatic force through siRNA and polymer (CDP/AD-PEG). The glomerular basement membrane dissembles these nanocarriers and the nanoparticles are then taken up by the glomerulus. The findings from Zuckerman et al. group bring another new aspect to the clearance mechanism of nanoparticles that form by polyion complexation through electrostatic force between cationic components and anionic nucleic acids. (Zuckerman and Davis 2013)

Furthermore, Wang et al. reported that their PEGylated nanoparticle with a size of 90 nm and 75 nm show significant kidney accumulation. (Wang et al. 2019a) The findings from different research groups suggested that nanoparticles with a size smaller than 100 nm are primarily taken up by the kidney's mesangial cells. However, due to the fenestration diameter of glomerular endothelial capillaries of 80-150 nm, nanoparticles with sizes larger than 100 nm tend to be restricted by mesangial cells uptake. Zuckerman et al. concluded that sub-100 nm nanoparticles are readily accumulation in the mesangium of mice. (Zuckerman and Davis 2013)

Therefore, carefully designing the physicochemical properties of nanoparticles could extensively affect the fate of the nanoparticles.

1.5 Conventional fluorescence characterization for *in vivo* distribution of drug delivery system.

In the field of translational medicine, fluorescent tags are applied to investigate the biodistribution profile and to evaluate the targeting ability of drug delivery systems such as quantum dots (Probst et al. 2013), nanoparticles (Priem et al. 2015), micelles (Cabral et al. 2018), or liposomes (Press et al. 2021) . Fluorescent tracers are also utilized in (bio)medicine to identify tumour metastases, inflammation, cell death, or organ functions in various tissues. (Kunjachan et al. 2013, Press et al. 2014, Priem et

al. 2015, Press et al. 2017a, Joshi et al. 2018) However, visualization and quantification of fluorescent markers in a biological sample like cells and tissues is always challenging.

Light and fluorescence microscopy, performed generally on excised tissue sections, have been well established in providing detailed tissue information at a cellular and subcellular level. Characterizing biological samples using fluorescent microscopy requires tedious pre-processing steps, such as tissue slicing, fixation, permeabilization of the tissue section, multiple washing steps, and several antibody-staining procedures to introduce the fluorescent probe. (De Matos et al. 2010) Most of the fluorescence microscopy imaging techniques are optimized to obtain high-resolution images in scanning the region of interest within the tissue slices. Scanning within the small region of interest allows viewing detailed information down to the intracellular level.

Even though conventional fluorescent microscopy offers high-resolution images, it often suffers with the tedious processes when it comes to more significant number of specimens that may be processed to gain enough field of view (FoV). (Földes-Papp et al. 2003, Graves et al. 2003) During the evaluation of drug delivery systems, uneven distribution or specific accumulation of drug carriers in certain organs often occurs. (Kulkarni and Feng 2013, Press et al. 2017b) Dreher et al. have reported that the distribution profiles of their nanocarriers in tumours differed within varied molecular weights of the nanocarriers. Lower molecular weight (Mw) nanoparticles could penetrate deeply into the tumour (greater than 35 μm) with homogeneous distribution, whereas the larger Mw particles penetrated shallowly and accumulated near the vascular surface. (Dreher et al. 2006) Thus, instead of the whole tumour, examining in a small area from the partial tumour slices in high magnification with fluorescent microscopic may overlook the overall distributions of the carrier inside the whole tumour. In order to access a large FoV on the tumour, large numbers of tumours slices at different partition is required, followed by numerous works on pre-processing the tissue slices for microscopy characterization.

Nevertheless, various techniques are available in scanning large FoV and providing information in tomographies, such as ultrasound imaging and magnetic resonance imaging (MRI). In recent years, Multi-spectral Optoacoustic Tomography (MSOT) advances in its advantages in providing tomographic 3D imaging and cross-sectional images in deep tissue with a non-invasive imaging manner. The whole animals or tissue section are illuminated in a temperate controlled water chamber with 360° laser ring illumination. MSOT provides a 270° detection of the acoustic signal on complete cross-sectional views of the animal, but sensitivity and image resolution at certain areas without a detector are still challenging. (Joseph et al. 2015) Besides, the selection of the markers or contrast agents is always limited to a substance with a longer excitation wavelength due to the working principle of acoustics imaging, *i.e.,* excitation in the (near-) infrared (NIR) region and detection of acoustic frequency alterations. The tracers feasible in MSOT application require working laser wavelength ranging from 680 to 980 nm with low quantum yield and solid acoustic signal. Thus, NIR probes are often applied in MSOT, limiting the feasibility for signal validation with fluorescent microscopy.

Another technique with 3D tomographic reconstruction for both fluorescence and bioluminescence, *in vivo* Imaging Systems (IVIS) is used intensively to characterize drug pharmacokinetics and pharmacodynamics in cancer research. (Koo et al. 2006, Mir et al. 2017) IVIS excite fluorescent markers or bioluminescence in two modes, trans-illumination (light source located at the bottom of the sample) and epi-illumination (light source located at the same planar with the camera, illuminate the sample from the top). However, this imaging technique is unable to provide cross-sectional images, and the sensitivity is usually limited. Thus, it is challenging to provide precise marker distribution with detailed anatomy information. (Joshi et al. 2018) In comparison to MSOT, IVIS could provide characterization with a broader range of fluorescence probes. Still, both techniques are suffering from low image resolution, problems with light attenuation in deep tissues, and difficulties in quantifying the fluorescent intensity.

Therefore, a method for tracing fluorescence markers that can access large area scanning at organ's level, without losing image resolution and detailed anatomy information, is worth investigating.

1.6   Aim of study

With the rising mortality rate, liver disease has become a huge burden of global health. (GBD 2018, Marcellin and Kutala 2018, Sepanlou et al. 2020) . Hepatocytes, having the largest cell population in the liver, are the main target of several chronic liver diseases. (Sehgal et al. 2013, Asrani et al. 2019) Being the main reticuloendothelial system in the body, the liver residing macrophages Kupffer cells clear out most of the foreign particles. (Owens and Peppas 2006, Li et al. 2020, Press et al. 2021) Therefore, effective hepatocytes targeting siRNA delivery platforms are crucial for maintaining the therapeutic effect and reducing off-target distribution. siRNA therapy shows its great potential in treating liver disease with a lipid-based delivery platform. (Akinc et al. 2019, Scott 2020, Scott and Keam 2021, Zhang et al. 2021) However, liposomes are still suffering from their complicated synthesis process, induction of immune response and concern of long term storage. (Whitemore et al. 1999, Judge et al. 2005, Simões et al. 2005, Roberts 2020) PEGylation on liposomes or a polymeric platform might be able to overcome these problems. Thus, in this study, we are aiming to achieve passive hepatocytes targeting delivery by establishing a series of diblock copolymer PEG-*b*-PAGE as a siRNA delivery platform. In previous research, we have reported that the surface charges, structural properties, and the interaction between cargo and carriers during encapsulation drastically affect the micelle formation as well as their cargo distribution and drug release profile. (Press et al. 2014, Rinkenauer et al. 2015) Based on the previous finding, we focus on investigating the effect of corona: core (PEG: PAGE) ratios (CCR) of siRNA polyplex micelles in altering their affinity in passive hepatocytes targeting.

In addition, we aim to develop a new automated imaging system that allows multi-sectional imaging on tracing the fluorescent probes and tissue anatomy on evaluating

the siRNA micelles distribution in every organ. A high-resolution cross-sectional image of the whole animals can be obtained with different organs visible in the same planar cross-section. With this automated imaging system, the siRNA polyplex micelles' biodistribution profile and elimination pathway over several organs will be examined.

We hypothesized that with higher CCR, the siRNA polyplex micelles would facilitate a more extended blood circulation profile due to the higher PEG density and can avoid recognition from Kupffer cells, further increase the accumulation in hepatocytes. To examine the effect of CCR, *in vivo* pharmacokinetics of these polyplex micelles and their distribution profile specific to hepatocytes are characterized.

2.   Materials and Methods

2.1   Materials

Poly (ethylene glycol) monomethyl ether (M_w of PEG_{42} = 2000 g mol^{-1}, M_w of PEG_{114} = 5000 g mol^{-1}), NaH (95%), CaH_2 (95%), 2,2-dimethoxy-2-phenylacetophenone (99%, DMPA), and allyl glycidyl ether (99%, AGE) were purchased from Sigma Aldrich. Cysteamine hydrochloride (98%) was obtained from Carbolution Chemicals (Sankt Ingbert, Germany). Potassium hydride (KH) was purchased from Acros Organics (ThermoFisher Scientific, Darmstadt, Germany) and purified by washing with dry cyclohexane under an argon atmosphere. All deuterated solvents for NMR measurements were received from Deutero. Regenerated cellulose membranes (Spectrum, Inc., Spectra/Por® 6 pre-wetted dialysis tubing) with a nominal molecular weight cut-off of 1 kDa were used to purify polymers *via* dialysis. Materials utilized in cell culture are Dulbecco's Modified Eagle's Medium (DMEM, Gibco), fetal bovine serum (FBS, ThermoFisher Scientific, Darmstadt, Germany), Penicillin Streptomycin Solution (Gibco, Thermo Fisher Scientific, Darmstadt, Germany).

2.2   Preparation of siRNA

All single strand oligonucleotides are provided by Eurofins Genomics (Ebersberg Germany) (Table 2.1). In house annealing were done by dissolving the single-stranded oligonucleotides into 1 mmol L^{-1} with 5X annealing buffer contained 300 nmol L^{-1} KCl, 30 nmol L^{-1} Hepes and 2 mmol L^{-1} $MgCl_2$. 10 µl of sense oligonucleotide was annealed with 10 µl of antisense oligonucleotide by adding 4 µl annealing buffer. The mixed solution was heated at 90 °C for 1 min followed by 1 hour incubation at 37 °C. The annealed oligonucleotide was then diluted to desire concentration for micelles preparation.

Table 2.1. The Oligonucleotides are utilized to form polyplex micelles that used in all physicochemical properties characterizations, *in vitro* and *in vivo* evaluation.

Oligonucleotide		Sequence (5' to 3')	Modification	Target
Toll-like receptor 4 (TLR4)	Sense (22 bp) $T_m = 54°C$	[2OMeU]CAUAUUCAAAGAUACACCCCC	5'-O-methyl-U	*TLR4,* NM_13855 4.4
	Antisense (22 bp) $T_m = 54°C$	[2OMeG]GGGGUGUAUCUUUGAAUAUGA	5'-O-methyl-G	
Cy3-Scum	Antisense (22 bp) $T_m = 58.4°C$	[CY3] TCAAACGTACGTTACGGGTCTT	5'-Cy3	
Cy5-Scum	Antisense (22 bp) $T_m = 58.4°C$	[CY5] TCAAACGTACGTTACGGGTCTT	5'-Cy5	None
Scum	Sense (22 bp) $T_m = 58.4°C$	AAGACCCGTAACGTACGTTTGA	-	
	Antisense (22 bp) $T_m = 58.4°C$	TCAAACGTACGTTACGGGTCTT	-	

All oligonucleotides are provided by Eurofins Genomics (Ebersberg Germany); * Cy: Cyanine; 2OMe: 2'-O-Methylation

2.3 Animals

All animal experiments were approved by the local government authority of Thuringia, Thüringer Landesverwaltungsamt, and performed according to the approved guidelines. FVB/N mice (at least 8 weeks old) were used in this entire study. All mice were housed under specific pathogen-free environments in the animal facility of the Jena University Hospital under artificial day-night cycles (12 h light-dark cycles) at a temperature of 23 °C room, the humidity of 30–60% with free access to standard rodent chew, acidified, sterile drinking water, and enrichment . All experiments were carried out on mixed populations of males and females.

2.4 Polymer Synthesis

All the diblock polymers PEG$_{42}$-*b*-PAGE and PEG$_{114}$-*b*-PAGE synthesised with different Mw of PEG are provided by Professor Schacher's group, University Jena. The PEG-*b*-PAGE synthesis and their amine functionalization processes are described in the following sections.

2.4.1 PEG$_{42}$-*b*-PAGE Synthesis and Amine Functionalization

EN15_poly, EN60_poly and EN76_poly are synthesized with Poly (ethylene glycol) (DP=42, 2000 g mol^{-1}) with a varied number of PAGE chains. PEG (approx. 500 mg) was melted at 110 °C and deprotonated with a spatula tip of sodium hydride (approx. 1.2 eq.). Allyl glycidyl ether (AGE) was added after 2 h, and the mixture was stirred for 24 h. The polymerization was quenched with MeOH (0.5 mL) and cooled to room temperature. The crude polymer was dried in a vacuum at 110 °C to afford PEG$_{42}$-*b*-PAGE. The yields are presented in Table 2.2.

Table 2.2. Synthesis yield and molecular characteristics of the synthesized diblock copolymers PEG$_{42}$-*b*-PAGE.

Polymer	PEG	AGE	Yield	M$_n$ (g·mol^{-1})[a]	Đ[a]	DP[b]
EN15_poly	0.493 g	0.5 mL (16.1 eq.)	0.963 g	2,600	1.15	15
EN60_poly	0.508 g	2.1 mL (65.6 eq.)	2.483 g	4,500	1.25	60
EN76_poly	0.504 g	2.5 mL (78.7 eq.)	2.835 g	5,000	1.24	76

[a] SEC (HCCl$_3$) using PEG calibration. [b] Determined by ^{1}H NMR (250 MHz, CDCl$_3$, δ, ppm) 6.0-5.8 (-OCH$_2$C*H*=CH$_2$), 5.4-5.1 (-OCH$_2$CH=C*H*$_2$), 4.1-3.9 (-OC*H*$_2$CH=CH$_2$), 3.8-3.3 (backbone). ^{13}C NMR (63 MHz, CDCl$_3$): δ = 70.2, 72.4, 78.9, 117.1, 135.1 ppm.

The synthesized PEG$_{42}$-*b*-PAGE were then modified through thiol-ene click reaction to introduce amino (-NH$_2$) groups. PEG$_{42}$-*b*-PAGE (approx. 200 mg), cysteamine hydrochloride (3.0 eq.) and 2,2-dimethoxy-2-phenylacetophenone (0.3 eq.) were dissolved in a 1:2 mixture of tetrahydrofuran (THF) and methanol (MeOH). The solution was degassed by flushing with Ar for 10 min and irradiated with UV light for 2 h under stirring. UV-Irradiations were carried out using a Hoehnle UVACUBE 100 equipped with a 100 W mercury-vapour lamp (λ = 365 nm). The polymer was purified by dialysis against THF, a 1:1 mixture of THF and water, and water to afford PEG$_{42}$-*b*-PAGE$_{NH2}$ after freeze-drying by Alpha 1-2 LDplus device. The yields of the resulting polymers PEG$_{42}$-*b*-PAGE$_{NH2}$ are presented in Table 2.3.

Table 2.3. Synthesis yield and molecular characteristics of the functionalized diblock copolymers PEG$_{42}$-*b*-PAGE$_{NH2}$

Polymer	PEG$_{42}$-*b*-PAGE	Thiol	DMPA	Yield	M$_n$ (g·mol^{-1}) [a]	Đ[a]	DoF[b]
EN15_poly	0.200 g	0.501 g	0.088 g	0.218 g	5,800	1.06	>99%
EN60_poly	0.204 g	0.669 g	0.096 g	0.242 g	7,600	1.09	>99%
EN76_poly	0.208 g	0.657 g	0.096 g	0.260 g	11,300	1.16	>99%

[a] SEC (DMAc) using PEG calibration. [b] Determined by ^{1}H NMR (250 MHz, MeOD-d_4, δ, ppm) 3.8-3.4 (backbone), 3.25-3.1 (-C*H$_2$*-NH2), 2.95-2.8 (-S-C*H$_2$*-CH$_2$-NH$_2$), 2.8-2.6 (-C*H$_2$*-S-), 2-1.8 (-C*H$_2$*-CH$_2$-S-) ppm.

2.4.2 PEG$_{114}$-*b*-PAGE Synthesis and Amine Functionalization

EN14_poly was synthesized with PEG (DP=114, 5000 g mol^{-1}). During the synthesis, PEG (1 eq., 250 mg), potassium hydride (1.2 eq., 3 mg) and dibenzo-18-crown-6 (1.5 eq., 35 mg) were placed in a 10 mL microwave vial, dissolve in 1 mL ethyl benzene, and stirred at 70°C. After 2.5 h allyl glycidyl ether, AGE was added to the turbid mixture, which turned clear after the addition of AGE. After 48h, the reaction was terminated by the addition of MeOH and the product was isolated by dialysis against THF/DCM and precipitation in diethyl ether. The yield of synthesized PEG$_{114}$-*b*-PAGE is shown in Table 2.4.

Table 2.4. Synthesis yield and molecular characteristics of the synthesized diblock copolymers PEG$_{114}$-*b*-PAGE

Polymer	PEG	AGE	Yield	M$_n$ (g·mol^{-1}) [a]	Đ[a]	DP[b]
EN14_poly	250 mg	0.1 mL (15 eq.)	133 mg	5400	1.07	14

[a] SEC (HCCl$_3$) using PEG calibration. [b] Determined by ^{1}H NMR (300 MHz, CDCl$_3$, δ, ppm) 6.0-5.8 (-OCH$_2$C*H*=CH$_2$), 5.4-5.1 (-OCH$_2$CH=C*H$_2$*), 4.1-3.9 (-OC*H$_2$*CH=CH$_2$), 3.8-3.3 (backbone) ppm.

The synthesized PEG$_{114}$-*b*-PAGE (1 eq., 100 mg), 2,2-dimethoxy-2-phenylacetophenone and cysteamine hydrochloride in the amine functionalization

process were placed in a 5 mL microwave vial and dissolved in 1.5 mL THF and 1 mL MeOH to give a reddish solution, which was degassed with Ar for 10 min. The mixture was then irradiated in the UV cube for 2 h to give a colourless solution. UV-Irradiations were carried out using a Hoehnle UVACUBE 100 equipped with a 100 W mercury-vapour lamp (λ = 365 nm). Finally, the product was purified by dialysis against water and THF, concentrated under reduced pressure and dried. The yield of the resulting PEG$_{114}$-b-PAGE$_{NH2}$ is shown in Table 2.5.

Table 2.5. Synthesis yield and molecular characteristics of the functionalized diblock copolymers PEG$_{114}$-b-PAGE$_{NH2}$

Polymer	PEG$_{114}$-b-PAGE	Thiol	DMPA	Yield	M$_n$ (g·mol^{-1}) [a]	Đ [a]	DoF [b]
EN14_poly	100 mg	86 mg	14 mg	99 mg	7200	1.03	100

[a] SEC (HCCl$_3$) using PEG calibration. [b] Determined by ^{1}H NMR (300 MHz, MeOD, δ) 3.8-3.4 (backbone), 3.3-3.15 (-CH_2-NH2), 2.95-2.8 (-S-CH_2-CH$_2$-NH2), 2.8-2.65 (-CH_2-S-), 2-1.8 (-CH_2-CH$_2$-S-) ppm.

2.5   Size Exclusion Chromatography

Size exclusion chromatography (SEC) analysis of PEG$_{42}$ -b-PAGE was performed in chloroform on a Shimadzu system equipped with an LC-10AD VP pump, a RID-10A detector, and a PSS SDV guard/linear S (5 µm particle size) column. A 94:2:4 mixture of chloroform, isopropanol, and triethylamine was used as eluent, and a flow rate of 1 mL per min at 30 °C was applied. Size exclusion chromatography (SEC) analysis of PEG$_{114}$-b-PAGE was performed in dimethylacetamide (DMAc) on an Agilent 1200 series equipped with a G1310A pump, a RID G1362A detector, and a PSS GRAM guard/1000/30 Å (10 µm particle size) column. DMAc with 0.1 g L^{-1} of lithium chloride as additive was used as eluent and a flow rate of 1 mL per min at 40 °C was applied. Both systems were calibrated using PEG standards from PSS (M$_n$ = 1.470 to 42.000 g mol^{-1}).

2.6   Nuclear Magnetic Resonance Spectroscopy

^{1}H NMR spectra were measured on a 300 MHz Bruker AC spectrometer at 298 K using the residual solvent resonance as an internal standard. The chemical shifts are given in ppm. All deuterated solvents used in ^{1}H NMR characterization were purchased from Deutero (Kastellaun, Germany).

2.7   Cell Culture

Hela cells were cultured in cell culture flasks at 37 °C, 5% CO_2 (HeraCell CO_2 Incubator, Heraeus, Germany). Dulbecco's Modified Eagle's Medium (DMEM, Gibco) with 10% fetal bovine serum (FBS, ThermoFisher Scientific, Darmstadt, Germany) and 1% Penicillin Streptomycin Solution (Gibco, Thermo Fisher Scientific, Darmstadt, Germany) was used as a culture medium. Cells were passaged at approximately 70% confluency by trypsinization.

2.8   Polyplex Micelles Preparation

Polyplex micelles encapsulated with siRNA were prepared by polyion complexation. All polymers were dissolved in Type 1 water with a concentration of 1 mg ml^{-1} for *in vitro* and 10 mg ml^{-1} for *in vivo* experiments. siRNA solution was prepared in nuclease-free water with a concentration of 200 ng µL^{-1}. Polyplex micelles were complexed by fast mixing of the polymer solution with siRNA solution at N/P ratio 5 (N/P ratio is defined as the residual molar ratio of amine (N) groups of polymers to the phosphate (P) groups of siRNA).

2.9   Gel Retardation Assay

Polyplex micelles were generated by using the method described above (section 2.8). A total volume of 20 µL for each polyplex micelle was prepared with a final concentration of siRNA at 20 ng µL^{-1} at different N/P ratios. Polyplex micelles were then stabilized by incubation at 4°C for 15 min. Agarose gel (2% w/w) was prepared by using 1X Tris-acetate-EDTA (TAE) buffer (Thermo Fisher Scientific, Darmstadt, Germany), comprised of 40 mmol L^{-1} Tris, 20 mmol L^{-1} acetic acids, 1 mmol L^{-1} EDTA.

Polyplex micelles with different N/P ratios were loaded into a pre-prepared agarose gel. Naked siRNA (20 ng μL^{-1}) was loaded as control while 100 base pair (bp) DNA ladder (Zymo Research GmbH, Freiburg im Breisgau, Germany) was also added as a size indicator. Samples-loaded gel was electrophoresed at 100 V using Owl Horizontal Electrophoresis Systems (Thermo Fisher Scientific, Darmstadt, Germany) for 45 minutes. The gel was then examined under an ultraviolet gel documentation system (Syngene, Maryland, USA) for visualization of the migrated siRNA bands.

2.10 Ethidium Bromide Assay

siRNA solution (200 ng μL^{-1}) was pre-incubated with 0.4 μg ml^{-1} ethidium bromide (EtBr) at 4°C for 15 min. EtBr containing siRNA solution was used to prepare polyplex micelles at a final siRNA concentration of 10 ng μL^{-1} with different N/P ratios by using the micelles complexation method mentioned above (section 2.8), followed by incubation at 4°C for 15 min. Measurement of EtBr fluorescence intensity in polyplex micelles solution was carried out on a fluorescence microplate reader (EnSpire, Perkin Elmer, Hamburg, Germany) with a dichroic filter at excitation and emission wavelength of EtBr ($\lambda_{Ex, max}$ = 530 nm, $\lambda_{Em, max}$ = 600 nm). The fluorescent intensity of each polyplex micelles was normalized with the EtBr intercalated siRNA solution (10 ng μL^{-1}) fluorescent intensity without polymer complexation.

2.11 Dynamic Light Scattering and Zeta Potential

All polyplex micelles were prepared by using the micelles complexation method mentioned above (section 2.8) in Type 1 water. The hydrodynamic radius and zeta potential of all polyplex micelles were measured by Zetasizer (Nano ZS, Malvern Instruments, Kassel, Germany). All micelles solutions were equilibrated for 3 min at 25 °C before measurement. The measurements were conducted for 3 × 20 runs (10 s per run) with a 633 nm light source and a detection angle of 173°. The measurements were analysed according to the cumulative analysis method to determine the mean hydrodynamic diameter and polydispersity index (PDI). (Danaei et al. 2018)

2.12   Transmission Electron Microscopy

10 µL of polyplex micelle solutions were dropped onto Quantifoil grids (Quantifoil, Jena, Germany, R2/2) and leave for 5 min. The excess solutions were removed by filter paper, leaving a thin polyplex micelles layer on the grid. After air drying, the grid was then transferred to FEI Tecnai G² 20 system (ThermoFisher Scientific, Darmstadt, Germany) for imaging at an acceleration voltage of 200 kV.

2.13   Reverse-Transcription Quantitative Polymerase Chain Reaction

The gene silencing efficacy of every polyplex micelles was evaluated by using one-step reverse-transcription quantitative (RT-q) polymerase chain reaction (PCR) with Toll-Like Receptor 4 (*TLR4*, NM_138554.4) as a target gene. HeLa cells were cultured in a 24-well plates (50,000 cells per well) with a culture medium (DMEM containing 10% FBS and 1% Penicillin Streptomycin Solution) and incubated overnight before transfection. Cells were then transfected with TLR4 siRNA (siTLR4) loaded polyplex micelles (200 nmol L^{-1} siRNA) with an NP ratio of 5 and positive control Lipofectamine™ 3000 (100 nmol L^{-1} siRNA) (ThermoFisher Scientific, Darmstadt, Germany) in Opti-MEM reduced serum media. Transfected cells were harvested at 3 time points (12, 24, 48 hours). RNA isolation was done by using Direct-zol RNA MicroPrep with TRI Reagent (Zymo Research GmbH, Freiburg im Breisgau, Germany). Reverse transcription and the quantitative PCR were carried out using the GoTaq 1-Step RT-qPCR System (Promega, Walldorf, Germany) on the RotorGene Q system (Qiagen, Hilden, Germany). *TCF7L2* gene (Wang and Xia 2016) was used as an endogenous housekeeping gene. The sequence of the primers used to amplify the *TLR4* target gene are AGCCGCTGGTGTATCTTTGA (forward) and TCGTCTCCAGAA GATGTGCC (reverse). Eurofins Genomics, Ebersberg Germany). The mRNA expression level was calculated based on the comparative C_t method ($2^{-\Delta\Delta Ct}$). (Livak and Schmittgen 2001)

2.14   Lactate Dehydrogenase Assay

According to the protocol described above, Hela cells were cultured and transfected with polyplex micelles. (Section 2.13). Non-transfected cells served as a control. The

polyplex micelles' cytotoxicity was determined by quantifying the lactate dehydrogenase (LDH) amount in culture supernatant medium after 24 h. The LDH assay was carried out using CytoTox96 Non-Radioactive Cytotoxicity Assay kits (Promega, Walldorf, Germany). 50 µL of the supernatant medium from the transfected cell was transferred to a 96-wells plate, followed by a 50 µL CytoTox96 reagent solution. After incubating for 30min, 50 µL of the stop solution was added to each well. The absorbance signal of LDH was measured by microplate reader (EnSpire, Perkin Elmer, Hamburg, Germany) at wavelength 490 nm. The result was normalized with the maximum LDH absorbance value obtained by 100% cell lysis.

2.15 Cellular Uptake

Hela cells were cultured and transfected with polyplex micelles in 12-well plates (50,000 cells per well) followed the protocol described above (section 2.13). Polyplex micelles were complexed with fluorescence cyanine (Cy) 3 ($\lambda_{Ab, max}$ = 554 nm, $\lambda_{Em, max}$ = 568 nm) labelled siRNA (Cy3-siRNA), allowing the tracking of the cellular uptake of polyplex micelles. The polyplex micelles' cellular uptake was evaluated after 1, 4, 12, and 24 h of incubation. Transfected cells were washed twice with PBS in order to remove the remaining polyplex micelles from the cell surface. The cells were detached by flushing them with a 5% ETDA PBS solution. The fluorescence signal of Cy3 in cells was measured by Flow Cytometer BD Accuri C6 Plus (Becton Dickinson, Heidelberg, Germany).

2.16 Raman Spectroscopy

All neat polymers and siRNA solutions (200 ng µL^{-1}) were prepared in nuclease-free water. All polyplex micelles with consistent siRNA concentrations of 200 ng µL^{-1} and N/P ratio 5 were prepared followed the protocol mentioned above (section 2.13). An upright micro-Raman system (CRM 300, WITec GmbH, Ulm, Germany) was utilized in the evaluation, equipped with excitation at 785 nm (200 mW laser power) and detection of Raman signal through a 300 g mm^{-1} grating and a Deep Depletion CCD camera (DU401 BR-DD, ANDOR, 1024 x 127 pixels). Measurement was carried out on CaF$_2$ substrate with 1 µL sample drop. An average of 15 spectra were taken at several positions for each sample using a 100x LD objective NA 0.75 (Carl Zeiss, Jena,

Germany) by integrating signals over 0.05 s per spectrum. The raw Raman spectra were pre-processed in R (version 4.0.2) (Rossiter 2012, Team 2013) by using in-house built algorithms to remove cosmic spikes. Pre-processing procedures included spectral background correction by using sensitive non-linear iterative peak (SNIP) algorithm (Ryan et al. 1988) and vector normalization. Principal component analysis (PCA) was evaluated by GNU R (version 4.0.2 or higher, package FactoMineR) (Lê et al. 2008) to visualize the differences present within different sample groups. All Raman spectra and PCA graphs were plotted using GNU R with ggplot2 plugin. (Wickham 2011) Peak area ratio was calculated to validate the CCR for each polyplex micelles. The quantification method is provided in Appendix 7.1 Figure A2.

2.17 Molecular Dynamic Simulation - Dissipative Particle Dynamic

The program Materials Studio 2020 (MS) and its modules are used for all the simulations. (BIOVIA 2020) The Visualizer and Amorphous Cell modules (Akkermans et al. 2013) were applied to construct atomistic models, and the Forcite module (Mo and Xu 2014) was utilised to optimize the structures further. All the above steps were performed with COMPASSII force field. (Sun et al. 2016) In addition, the Mesocite module was adopted for DPD simulations. (Ruiz-Morales and Romero-Martínez 2018) DPD simulations are performed by using coarse-grained models with beads. The simulation systems presented in this work consisted of siRNA, PEG-b-PAGE$_{NH2}$ block copolymers, and solvent water. The detailed procedures of DPD for every polyplex micelle are provided in Appendix 7.2.

2.18 Intravital Microscopy

FBV/N mice were given 1/5 mg kg^{-1} body weight (BW)$^{-1}$ Meloxicam (Melosus 0.5 g L^{-1}, CP-Pharma, Burgdorf, Germany) orally for pain relief before the experiment. Both Laparotomy on the left lateral abdomen and tail vein catheter insertion was performed under general isoflurane anaesthesia. The liver was gently flattened and fixed onto the cover glass, ensuring sufficient exposure area for imaging. Mice were placed on a heating pad with the controlled temperature at 37 °C throughout the experiment. Intravital microscopy imaging was carried out on LSM-780 (Carl Zeiss, Jena, Germany) with the specification of air-corrected 20x plan-apochromatic numerical aperture (NA)

0.8 (Carl Zeiss, Jena, Germany). Liver tissue was detected by NAPDH autofluorescence with excitation from 375 nm to 405 nm and emission from 410 nm to 485 nm. After 1 min of imaging, 30 µg of Cy3-siRNA encapsulated polyplex micelles were injected through a tail vein catheter. Time-lapsed images were acquired at every minute for a total of 45 min at 7 different positions. After the time-lapsed imaging, approximately 10 µg Fluorescein isothiocyanate (FITC)-labelled F4/80 (Clone: BM8) antibody and 6 µg of Allophycocyanin (APC)-labelled CD54 (Clone: YN1/1.7.4) antibody (both from Biolegend, USA) were administrated through the catheter to visualize Kupffer cells (the local liver macrophage population) and endothelial cells respectively. Images were taken using an air-corrected 40x plan-apochromatic objective NA 0.95 (Carl Zeiss, Jena, Germany). After all experiment procedures, animals were euthanized by cervical dislocation under the status of general anaesthesia.

2.19 Mesoscopic Imaging

Mice were injected intravenously with Cy5-siRNA loaded polyplex micelles (30 µg). The injected mice were sacrificed after 15 min and 45 min of injection. Euthanized mice were shaved thoroughly on the whole abdomen and back using commercial hair removal cream and then frozen in TissueTek (OCT Compound, USA). The episcopic imaging system was set up on the cryo-microtome (CM3050 S Cryostat, Leica Biosystems, Wetzlar, Germany), allowing cross-section imaging of the whole mouse. Mice tissue sections was excited with a LED light source at 625 nm wavelength (M625L4, Thorlabs, Newton, New Jersey, USA) through a 1" bandpass filter with center wavelength of 630 nm and FWHM of 20 nm (ET630/20x, Chroma, Bellows Falls, VT, USA). Cy5 fluorescence signal was observed through a 2" bandpass filter with center wavelength of 670 nm and FWHM of 30 nm (ET670/30m, Chroma, Bellows Falls, VT, USA). Images were taken by a monochrome camera with 4500 x 3600 pixels with a pixel size of 6 µm (MicroLine ML16200, FLI Instruments, Lima, N.Y., USA) and 1:1 lens with 89 mm focal length using f/4.8 (XENON-ZIRCONIA 2.8/89, Schneider Bad Kreuznach, Germany). RGB images were acquired by sequentially illuminating the sample with a ring of red, green and blue LEDs (24x SK6812RGBW-WS, Opsco, Guangdong, China).

2.20 General Statistics

GNU R version 4.0.2 or higher was used in all data processing, analysis and visualization. The packages and plugins used were the following: stringr, tidyverse, purrr, concatenate, Rmisc, dplyr, ggplot2, readr, readxl, grid, hyperSpec, stats, graphics, cluster, e1071, MASS, klar, peaks, ellipse, plotrix, klaR, FactoMineR. Images were analysed and visualized with Fiji distribution of ImageJ 2.0.0-rc-69/1.52p, Inkscape 1.0, and in-house developed software CIAnalyzing version 1.7 © Leibniz-Institute of Photonic Technologies, Jena, Germany. The Wilcoxon rank sum test evaluated statistical significance using pairwise comparisons since normal distribution and equal variances were not present in all datasets. In the case of multiple comparisons on a dataset, the false discovery rate had been controlled by applying the Benjamini-Hochberg procedure. (Benjamini and Hochberg 1995) The testing methods applied are stated in the figure captions. Detailed information on replicates of each experiment is provided in Appendix 7.1 Table A1.

3. Results

3.1 Corona: core ratios of polyplex micelles varied by the different combinations of diblock copolymer

In the gene delivery system, polymers complexed with oligonucleotides to form polyplex micelles. In this work, siRNA loaded polyplex micelles EN14, EN15, EN60 and EN76 were prepared by polyion-complexation between the cationic block copolymers PEG-*b*-PAGE with anionically charged oligonucleotide (siRNA) at nitrogen to phosphate (N/P) ratio of 5. The N/P ratio here is defined by the ratio of moles of the primary amine groups of cationic polymers to anionic phosphate groups in the RNA-backbone of the siRNA. The corona: core ratio (CCR) of each polyplex micelles are represented in the ratio of the number average of molecular weight (Mn) between PEG block and PAGE chains from the corresponding neat polymers (Table 3.1 & Figure 3.1 a). At the same N/P ratio, the amount of every neat polymer required to complex with the constant amount of siRNA is different due to varying amounts of cationic charges from the PAGE chain. This results in higher PEG ratio, *i.e.,* CCR, in EN14 and EN15 with the shorter PAGE chains, more PEG-*b*-PAGE is needed to complex siRNA. Between EN14 and EN15, EN14 possess even higher CCR due to the increased molecular weight on the PEG block (5000 g mol^{-1}). With longer PAGE chains, E60 and EN76 shows lower PEG content on the corona, thus lower CCR (Figure 3.1 b). The CCR determines the PEG surface density and therefore may have influences on the polyplex micelles' pharmacological properties.

Table 3.1. Corona: core ratio (CCR) of each complex calculated by the ratio between the number averaged molecular weight (Mn) of the PEG corona and Mn of PAGE core with various degrees of polymerization of PAGE chain.

Polyplex Micelles	Mn of PEG (g mol^{-1})	DP of PAGE	Mn of PAGE (g mol^{-1})	Mn ratio PEG:PAGE (CCR)
EN14	5033	14	2674	1.88
EN15	1865	15	2808	0.66
EN60	1865	60	11458	0.16
EN76	1865	76	14579	0.13
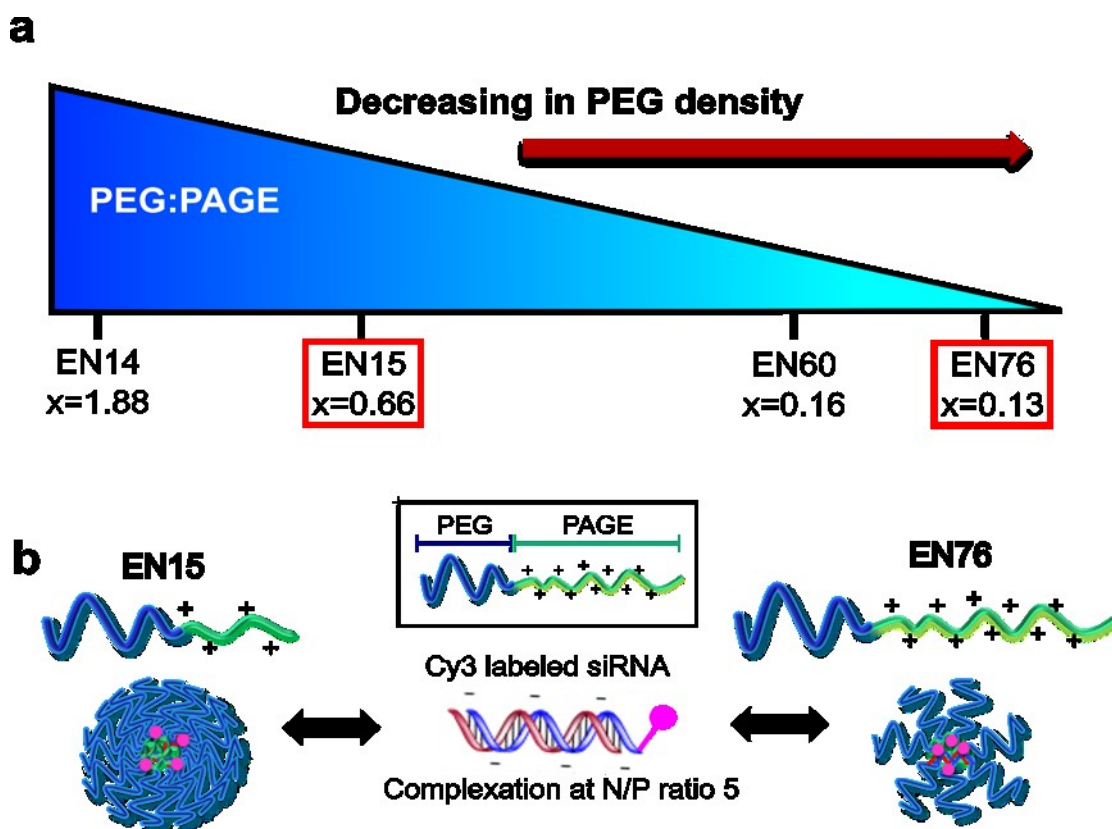
Figure 3.1. Schematic graph of corona: core ratio (CCR) of siRNA polyplex micelles forms by different diblock copolymers. (a) CCR of each polyplex micelles was calculated by the ratio between the number averaged molecular weight (Mn) of the PEG corona and Mn of PAGE core with various degrees of polymerization of PAGE chain. **(b)** Illustration of polyion complexation between Cy3-siRNA and diblock copolymer EN15_poly and EN76_poly results in EN15 and EN76 polyplex micelles at N/P ratio 5.

3.2   PEG-*b*-PAGE as a carrier platform for siRNA delivery

In order to alter the CCR on polyplex micelles, we synthesized a series of diblock copolymer PEG-*b*-PAGE with varied degrees of polymerization of PAGE on two different molecular weight PEG blocks (2000 g mol^{-1} and 5000 g mol^{-1}). All the diblock copolymers were synthesized by sequential anionic ring-opening polymerization of allyl glycidyl ether (AGE) with deprotonated poly (ethylene glycol) (PEG) monomethyl ether as macro-initiator. (Barthel et al. 2012) PAGE blockchains with different degrees of polymerization were modified with cysteamine through thiol-ene click reaction to receiving functional amino (-NH$_2$) groups. The synthesized polymers were characterized by size exclusion chromatography (SEC) and ^{1}H NMR spectroscopy.

The degree of functionalization with amine groups was determined by ^{1}H NMR spectroscopy through the decrease in intensity of the characteristic signals for the pendant double bonds of PAGE at 5.9 and 5.3 ppm compared to the backbone signal at 3.8 to 3.4 ppm (Figure 3.2 b, c, d). The polymers EN14_poly was synthesized by PEG with molecular weight of 5000 g mol^{-1}, while PEG with 2000 g mol^{-1} was used for EN15_poly, EN60_poly and EN76_poly. The degree of polymerization of PAGE chains on EN14_poly (14 repeating units) and EN15_poly (15 repeating units) was considered as similar value. All functionalized diblock copolymers carry cationic charges from the amine groups that were clicked onto the PAGE chain.
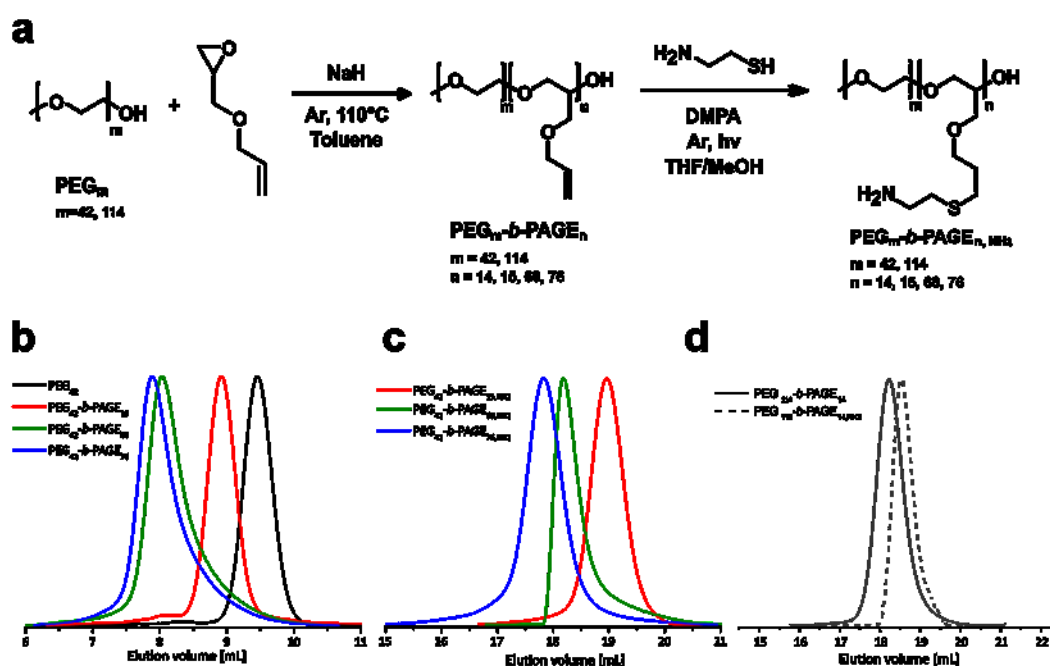
Figure 3.2. Polymer synthesis scheme and Size exclusion chromatography (SEC) characterization. (a) Schematic representation of the preparation of PEG$_m$-*b*-PAGE$_{n,NH2}$ (m=42, 114 and n=14, 15, 60, 76) by ring-opening polymerization. **(b)** The characterization of SEC on the synthesized PEG$_{42}$-*b*-PAGE$_n$ (n=15, 60, 76) and amine groups functionalized **(c)** PEG$_{42}$-*b*-PAGE$_{n,NH2}$ (n=15, 60, 76), *i.e.,* EN15_poly, EN60_poly and EN76_poly. **(d)** PEG$_{114}$-*b*-PAGE$_n$ and PEG$_{114}$-*b*-PAGE$_{n,NH2}$ (n=14), *i.e.,* EN14_poly.

3.3   Diblock copolymer achieved complete complexation with siRNA

In order to facilitate an efficient gene delivery system, the cargo, *i.e.,* siRNA in this case, have to be fully encapsulated or complexed within the carrier systems, *i.e.,* diblock copolymers here. Therefore, ethidium bromide (EtBr) and gel retardation

assay (GRA) assay that widely used in characterizing the full complexity of polyplex micelles were carried out to confirm the degree of encapsulation of the siRNA in polyplex micelles.

EtBr exhibits intense fluorescence signals when intercalating with oligonucleotide. Complexation between oligonucleotide with cationic polymers would decrease EtBr fluorescent intensity, implying that the sites of EtBr intercalation are replaced by polymer complexation. In this assay, polyplex micelles with different N/P ratios are prepared by complexation of the same amount of siRNA with varying polymers. The concentration of siRNA and EtBr in each sample remains constant. EtBr containing siRNA only solution, *i.e.,* without any polymers complexation (N/P ratio of 0) served as a control sample. The fluorescent intensities (FI) of each micelle are normalized with the FI of control samples. The result shows a dramatic decrease in EtBr fluorescence intensity in all diblock copolymers when complexed with siRNA at N/P ratio 1 and remains low fluorescent intensity even with increasing the N/P ratio (Figure 3.3 a).

All the polyplex micelles loaded with 22-nucleotides double-stranded siRNA at varied CCR were run on 2% agarose gel and visualized by ultraviolet illumination. The electrophoretic mobility of each sample was examined to evaluate the degree of siRNA entrapment. Naked siRNA solution, *i.e.,* N/P ratio of 0, was used as a reference. DNA maker ladder (100 bp) was also loaded as a size indicator. From Figure 3.3 b, a slight smear of siRNA trace on the gel at N/P ratio 1 was observed in polyplex micelles EN14 and EN15 with high CCR, indicating possible incomplete complexation of siRNA with these polymers with short PAGE chains of 14, 15 and even 60. While polymers with longer PAGE chains of 76, *i.e.,* lower CCR, showed complete complexation even at N/P ratio of 1.

Both GRA and EtBr assay proved that all the diblock copolymers established a stable and complete complexation with siRNA at N/P ratio 5 in an aqueous environment. Thus, all the polyplex micelles that are used in the following *in vitro* and *in vivo* experiments are complexed at N/P ratio 5.
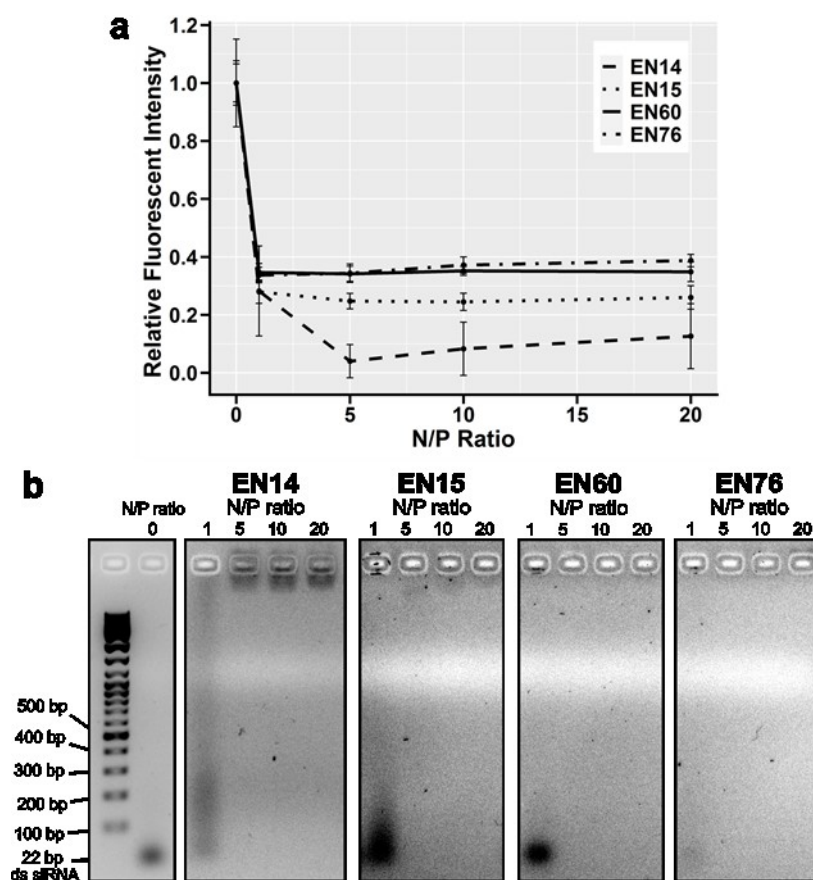
Figure 3.3. Complexation of siRNA with a diblock copolymer of varying corona: core ratio (CCR). (a) Ethidium bromide assay (EtBr) of all siRNA polyplex micelles by different diblock copolymer at different N/P ratios. N/P ratio of 0 represents the control samples, *i.e.,* only siRNA with EtBr without complexation with polymers. The difference of N/P ratios is obtained by complexing the consistent amount of siRNA with varying polymers. The relative fluorescence intensity (FI) is calculated by dividing the FI of the sample with the FI of the control samples, *i.e.,* N/P ratio 0. Complexation of siRNA with polymer leads to the replacement of EtBr intercalation with siRNA resulting in a decrease in FI. The graph is plotted with the mean ± SD of 3 duplicates. **(b)** Gel retardation assay is performed in 2% agarose gel at 100 V for 45 min to evaluate polyplex micelles complexation with dsRNA. N/P ratio of 0 represents the control samples, *i.e.,* siRNA without complexation with polymers. The contrast of the images was adjusted to improved visualization. The first lane of the gel represents the DNA marker ladder (100 bp) with the first 5 bands labelled.

3.4 Characterization of determined physicochemical properties of polyplex micelles

3.4.1 The architecture (hydrodynamic sizes, shapes) and surface properties (zeta potentials)

The hydrodynamic size and zeta potential of the polyplex micelles are characterized by dynamic light scattering. Polyplex micelles complexed with lower PEG Mw (2000 g mol^{-1}) diblock copolymer, *i.e.,* EN15, EN60 and EN76 obtained a narrow polydispersity index (PDI) with a value between 0.23 to 0.25, indicating a uniform size distribution of these micelles. While micelles complexed with high PEG Mw (5000 g mol^{-1}) EN14 showed larger PDI at 0.51, implying possible aggregation of polyplex micelles are formed (Figure 3.4 a). EN15 polyplex micelles possess the most minor hydrodynamic diameter at 70 nm. Both EN60 and EN76 possess a similar size at 100 nm. However, EN14 micelles complexed with higher PEG Mw polymers showed a larger size at around 350 nm, respectively, which further proves possible aggregation between polyplex micelles. With an excess amount (N/P ratio 5) of cationic polymer forming the polyplex micelles, all micelles possess cationic zeta potential ranging from 10 to 30 mV (Table 3.2). The cryo-TEM images further confirmed the spherical shapes of all the micelles (Figure 3.4 b).

Table 3.2. The table of hydrodynamic diameters, PDI values, and zeta potentials of different micelles used in this study

Micelles	Size d_h (nm)	PDI	Zeta Potential (mV)
EN14	357	0.51	+10
EN15	71	0.25	+24
EN60	104	0.23	+29
EN76	101	0.23	+30
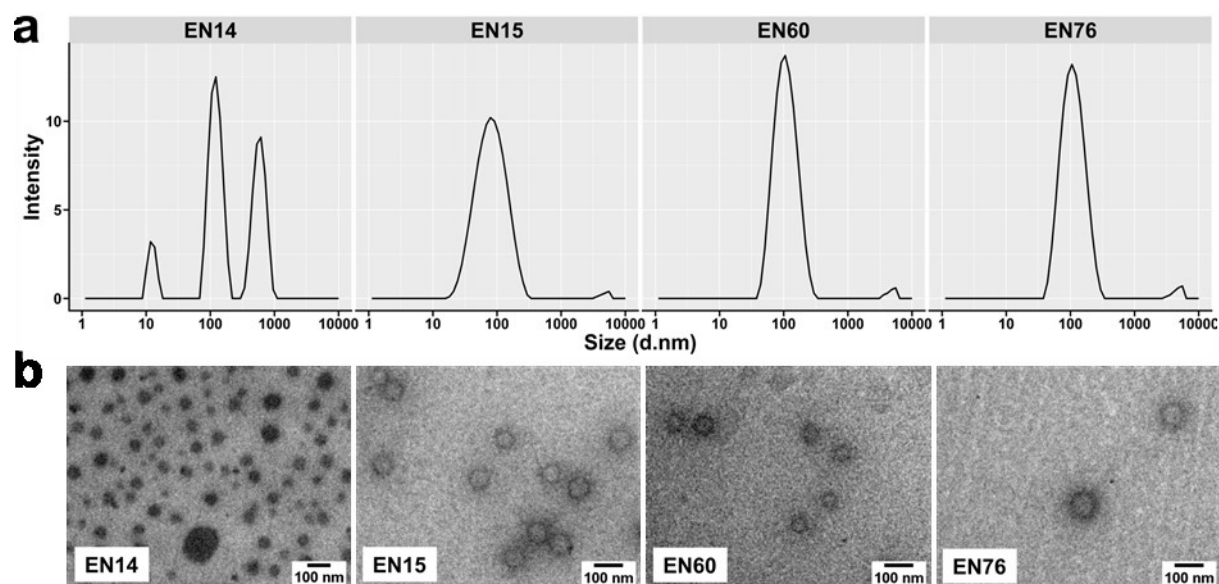
Figure 3.4. Characterization of siRNA complexes with different corona:core ratios (CCR). (a) Representative dynamic light scattering (DLS) with number weighted characterization for different polyplex micelles. EN15, EN60 and EN76 show relative uniform size distribution, while EN14 exhibits 3 peaks with large size distribution. **(b)** TEM imaging suggests a spherical shape of all polyplex micelles. The nonuniform size of EN 14 shown in the TEM images further confirmed the DLS data.

3.4.2 Structural fingerprint revealed by Raman spectroscopy

We further performed Raman spectroscopy on each polyplex micelle with unlabelled scum siRNA (22 bp) and their neat diblock copolymers without any complexation to investigate the relationship between polyplex micelles with different corona: core ratios. As a result, all the polyplex micelles were prepared at the same N/P ratio 5 with the constants concentration of block copolymers. Raman spectroscopy is commonly used in providing structural fingerprints to identify different molecules by determining the vibrational modes of atomic bonds. (Castiglioni et al. 1993) The wavenumber at which the vibration occurs is specific to the type and interacting molecules but also is highly environmental dependent, *i.e.,* able to reflect the complexation of each particular bond. Thus, molecular bonds in a macromolecule that is highly complexed by its environment will hardly contribute to the Raman signal, but if the same bond in this macromolecule is free to vibrate, it will strongly contribute to the Raman signal. On this basis, an in-depth analysis of the micellar confirmation is obtained and compared between different micelles.

In the characterization of neat polymers, EN14_poly and EN15_poly exhibited a strong Raman signal at vibration peak 1480 cm^{-1}, attributed to the CH$_2$ stretching from PEG blocks (Figure 3.5 *). (Press et al. 2017b) While spectra of EN60_poly and EN76_poly showed a stronger, more substantial vibration peak at 651 cm^{-1} (Figure 3.5 **), the C-S stretching contributed from PAGE blocks due to the long PAGE chains on these three polymers. The same phenomenon was observed when those neat polymers are complexed with the siRNA formed micelles. This result reveals that EN14 and EN15 with higher CCR exhibit strong Raman signal contributed from PEG block (Figure 3.5 *), confirming PEG shell contributed significantly more than PAGE blocks on these micelles. In contrast, PAGE vibration peak 651 cm^{-1} was more expressed in micelles with lower CCR, *i.e.,* EN60 and EN76 (Figure 3.5 **), indicating PAGE core of these micelles are more pronounced.
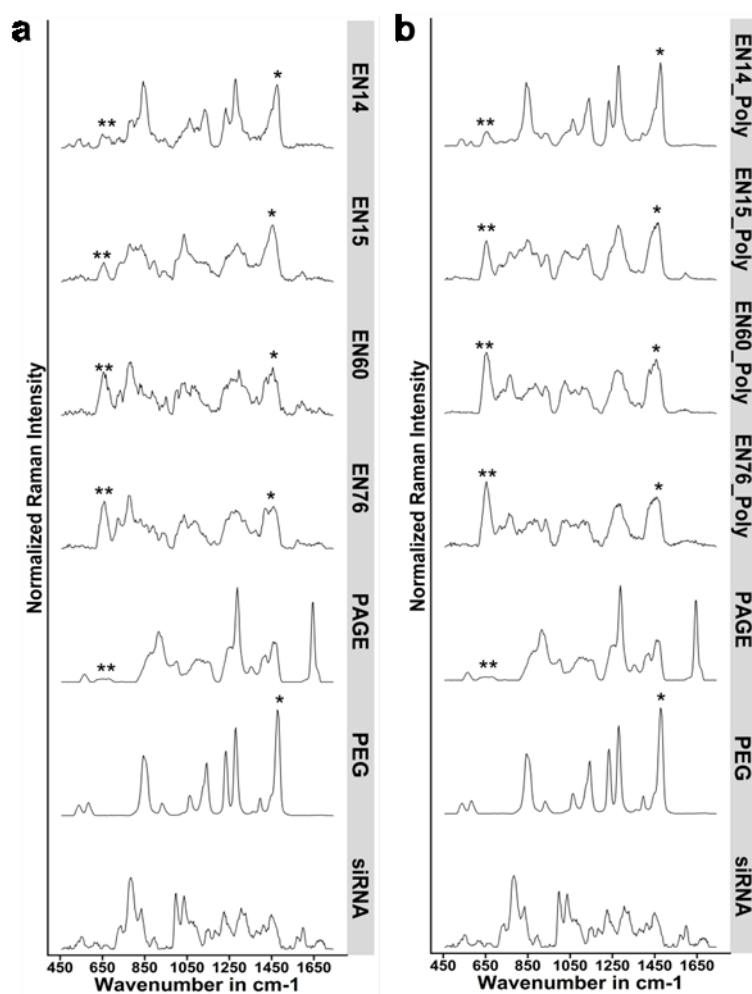
Figure 3.5. Mean Raman spectra obtained from Raman Spectroscopy characterization on different (a) polyplex micelles and (b) their corresponding neat polymers. Polyplex micelles are labelled with "EN" and the number of repeating units of polyethylene oxide. The neat polymer carries the addition "Poly". Raman spectra of monomers (poly allyl glycidyl ether, PAGE and polyethylene glycol, PEG), as well as the pure siRNA, are given as a reference. * are the vibration peak at 1480 cm^{-1} attributed to PEG; ** represent the PAGE vibration peaks at 651 cm^{-1}.

3.4.3   Principle component analysis and validation of CCR of polyplex micelles

We subjected all spectra to an unsupervised principal component analysis (PCA) to extract significant differences between every polyplex micelle and their corresponded neat polymers (Figure 3.6). By selecting different combinations of principal components (PC), the spectra' classification can be easily done with a new coordinate system. The resulting PC1 and PC2 demonstrated a clear differentiation within all materials. Both polyplex micelles and polymers are clustered in a similar trend. EN14

(and EN14_poly) is differentiated significantly with the other two clusters, EN15 (and EN15_poly), as well as EN60 and EN76 (and EN60_poly and EN76_poly) (Figure 3.6 a, b). The clustering results are also consistent with the calculated CCR ratio that can also be grouped into three distinct groups, *i.e.,* 1.88 (EN14), 0.66 (EN15), 0.16 (EN60) and 0.13 (EN76). The contribution of different Raman peaks for the classification in PC1 and PC2 are given in Figure 3.6 c. The significant contributed vibration peaks in PC1 are 781 cm^{-1}, 843 cm^{-1}, 1277 cm^{-1}, 1480 cm^{-1} which are attributed to the CH_2 stretching of PEG blocks, the corona shell (Table 3.4). (Press et al. 2017b) The differentiation in PC2 is mainly contributed (around 5%) by the vibration at 651 cm^{-1}, a result of C-S stretching, which can be exclusively attributed to the PAGE block, *i.e.,* the PAGE core (Table 3.4). (Press et al. 2017b) Further contributions at vibration peaks 1036 cm^{-1} and 1143 cm^{-1} (Gong et al. 2009) to the differentiation had been assigned to ribose stretching and phosphate group from the siRNA molecule. All significant contribution peaks for PC1 and PC2 are summarized in Table 3.4.

The Raman peak area is interpreted as the signal strength. The ratio of most contributed PEG (1480 cm^{-1}) and PAGE (651 cm^{-1}) peak area was quantified to validate the theoretical CCR ratio further. The quantification method is explained in Appendix 7.1 Figure A2. The calculated peak area ratios (Table 3.3) report a similar value with the theoretical CCR ratio obtained from the molecular weights of the individual PEG and PAGE blocks for different micelles. The peak area ratio of EN15, EN60 and EN76 is similar to with the theoretical CCR ratio. At the same time, EN14 shows slight variation from the expectation, which could also be explained by high PDI from DLS results, probably owing to the aggregation of the micelles and uncomplexed free polymers. The differences in CCR and the highly different Raman vibrational fingerprints of all micelles, depicted in the PCA, suggest distinct structural properties of the investigated micelles give rise to a distinct structural property of micelles.

.
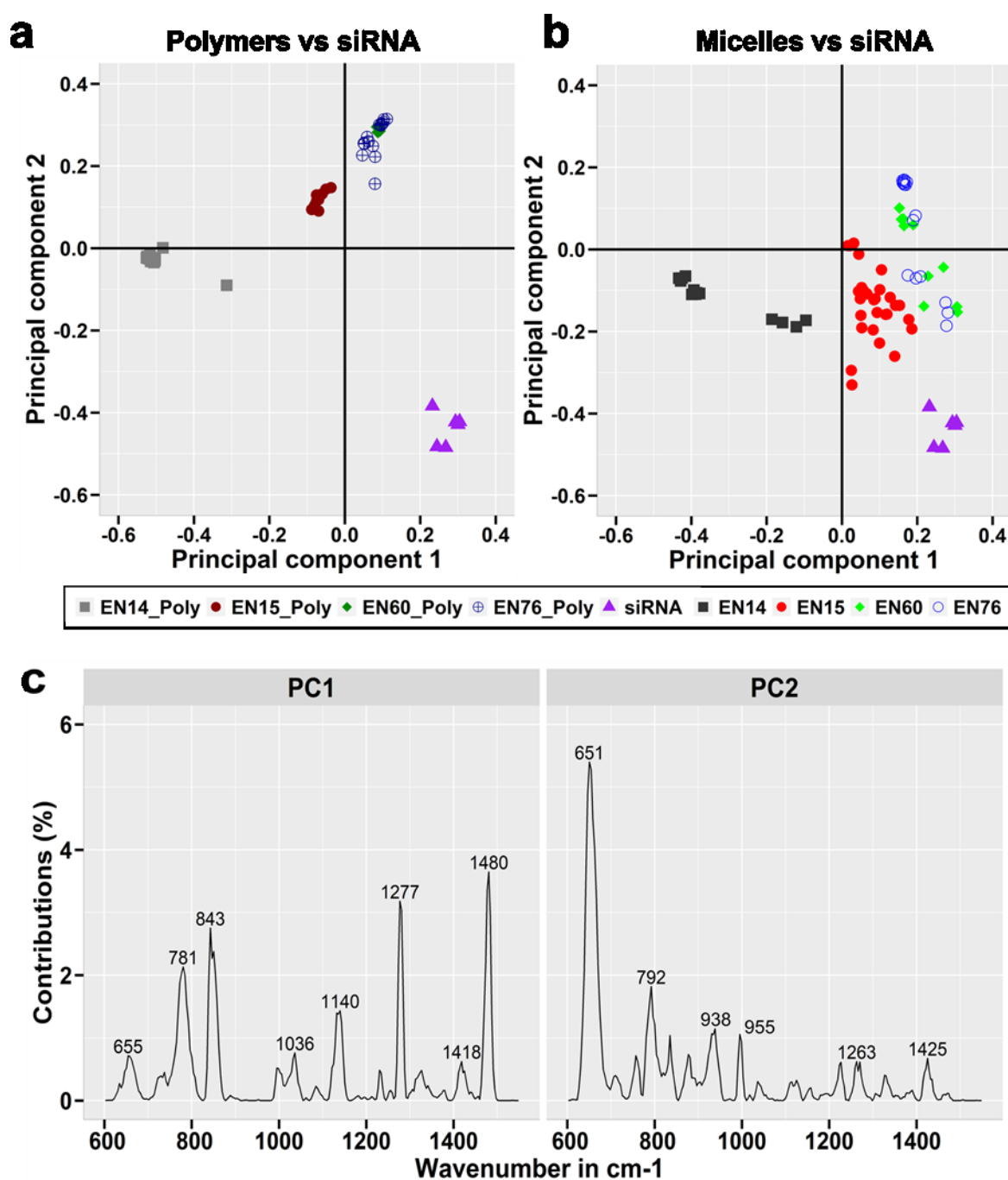
Figure 3.6. Principle component analysis (PCA) was performed with two dimensions (PC1 and PC2) in all the spectra of polyplex micelles and their corresponded neat polymers. PCA was carried out in comparison of the spectra from all polyplex micelles and neat polymers. Even though the PCA results of **(a)** neat polymers and **(b)** polyplex micelles are plotted into separate graphs for easy comparison, both are at the same scales and the results are comparable in both PC1 and PC2 axis within two graphs. **(c)** The contribution percentage of PC1 and PC2, presented in the wavenumber (cm $^{-1}$).

Table 3.3. The peak area ratio between PEG (1480 cm^{-1}) and PAGE (651 cm^{-1}) in different CCR polyplex micelles.

Polyplex Micelles	Peak Area Ratio (PEG:PAGE)	Normalized AUC Ratio (PEG:PAGE)	Theoretical calculated Mn ratio (PEG:PAGE)
EN14	4.44	**0.52**	1.88
EN15	5.59	**0.66**	0.66
EN60	1.39	**0.16**	0.16
EN76	1.35	**0.16**	0.13

Table 3.4. The vibrational assignment of the significant Raman peaks in dimensions PC1 and PC2 is displayed in Figure 3.6 c.

Raman peaks in PC1 (cm^{-1})	Raman peaks in PC2 (cm^{-1})	Raman peak assignment
655	651	C-S stretch
781		CH$_2$ rocking in methylene chain
	792	RNA
843		skeletal str polymer
	938	PAGE
	995	RNA
1036		polymer, ribose
1140	1125	C-O-C stretch PEG, phosphate
1277	1263	CH$_2$ torsion of PAGE and PEG
	1327	RNA vibrations
1418	1425	CH$_2$ deformation, C-O-H bending
1480		CH$_2$ scissor gauche, in-plane bending CH$_2$ (PAGE and PEG)

3.4.4 Polyplex micelles inner structures obtained by dissipative particle dynamic simulation

The detailed information of the internal structures and the mechanism of complexation of micellar gene delivery system occurring in the temporal scale remain unclear. (Luo and Jiang 2012, Hao et al. 2019) In this regard, computer simulation has often been identified as a powerful tool to help in understanding the formation mechanism of the micelles and further to visualize the internal structures. As a result of this, we investigated the structural morphology of all the polyplex micelles with different CCR by applying a dissipative particle dynamic (DPD) simulation, which has been effectively used in simulating amphiphilic block copolymers at the mesoscale. (Hoogerbrugge and Koelman 1992) DPD simulation results of reveals different final structures of all the polyplex micelles. The modelling-compartment depicts a random distribution at the beginning of simulation of all polyplex micelles. As the simulation proceeds further, all polyplex micelles gradually formed a layer structure with PEG molecules formed an outer corona. PAGE beads accumulated around the siRNA as a core, driven by the polyion interactions between siRNA and the neat polymers. After 10000 steps, the micelle structure was observed stable and maintained its stability in the next 10000 steps (20000 steps for the whole simulation) (Figure 3.7 a). After 20000 steps, EN14 and EN15 formed an entire PEG corona, while only an interrupted PEG corona with PAGE core was observed in EN60 and EN76. The sectional view of the compartment shows a significant thicker PEG corona of EN14 than EN15. PEG corona layer became thinner with increasing the PAGE chain. The siRNA molecules are stably compacted in the core of the EN14, EN15 and EN60 micelle. However, the modelling compartment of EN76 showed that the siRNA molecule was pushed out of the polyplex micelle (Figure 3.7). The simulation results confirmed that all the neat diblock copolymers could form micelle structures complexing with siRNA, but only EN14, EN15 and EN60 nicely encapsulated siRNA in the inner core and surrounded with an intact PEG shell.
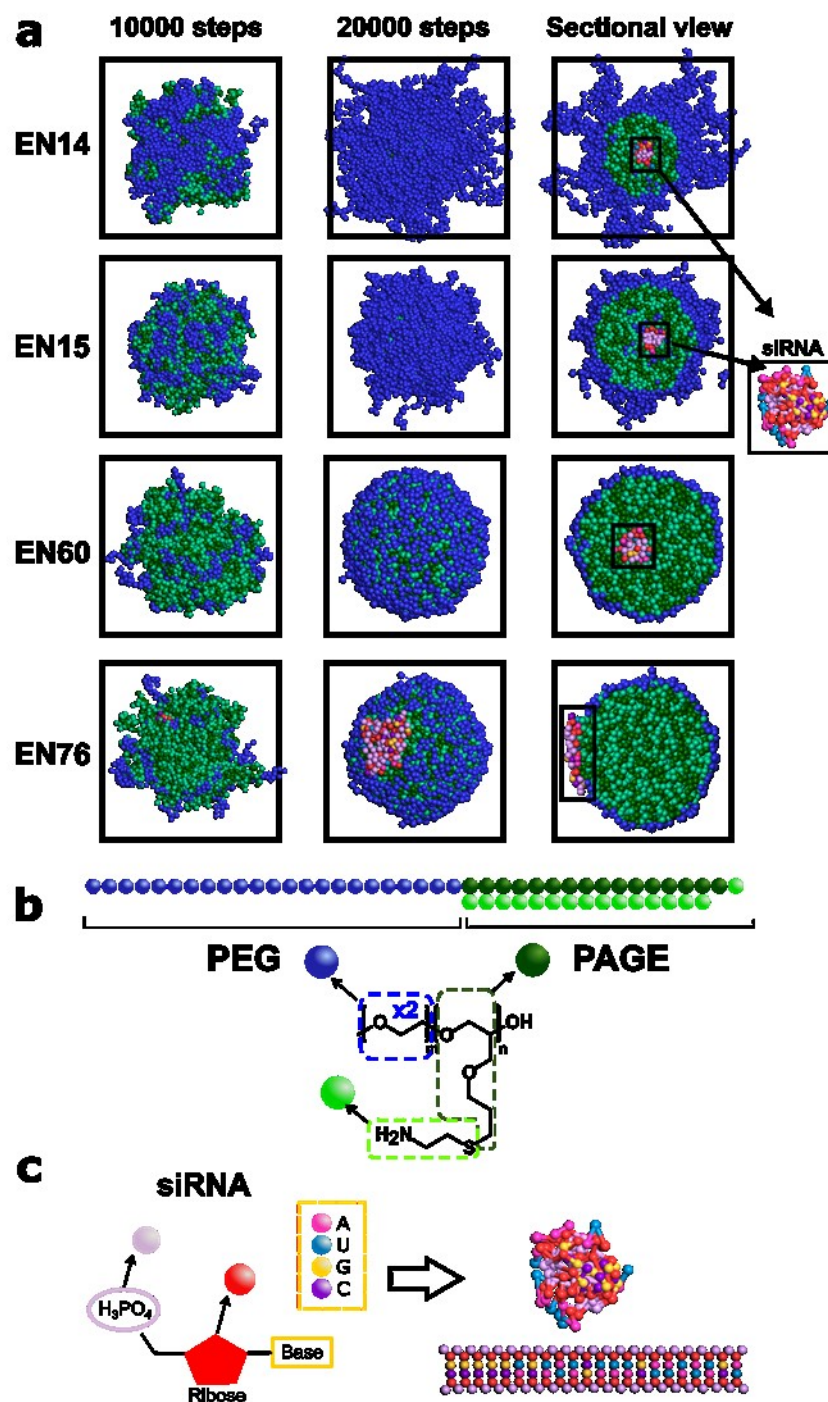
Figure 3.7. Dissipative particles dynamic (DPD) simulation reveals the different inner structures of polyplex micelles based on the CCR. (a) Snapshots of the configurations of EN14, EN15, EN60 and EN76 with siRNA (water beads were hidden) after 10000 and 20000 steps. Further, the sectional views exposed the location of siRNA (indicated in squared box) inside each polyplex micelle. **(b)** The coarse-grained structures of PEG-*b*-PAGE diblock copolymer and **(c)** siRNA.

3.5 Polyplex micelles with different CCR exhibit different behaviour in *in vitro* pharmacokinetics and pharmacodynamics (PK/PD)

The biocompatibiliy of nanocarrier is a very crucial issue in designing a drug/gene delivery system. Thus, characterization of cytotoxicity of each polyplex micelles was carried out to confirm the low toxicity of the PEG-*b*-PAGE platform. Lactate dehydrogenase (LDH), a stable cytosolic enzyme present in many different cell types, is released into the cell culture medium upon damage of the plasma membrane. Hence, an LDH assay was performed on Hela cells to examine the cytotoxicity of polyplex micelles. LDH released from the cell to the culture supernatants results in converting a tetrazolium salt (iodonitro-tetrazolium violet; INT) in the reagent into a red formazan product. The intensity of the generated colour is directly proportional to the number of lysed cells. The absorbance value of the resulted solution were measured at wavelength 490 nm. Lower values as compared to untreated micelles proves the insignificant cytotoxicity of all the polyplex micelles (Figure 3.8).
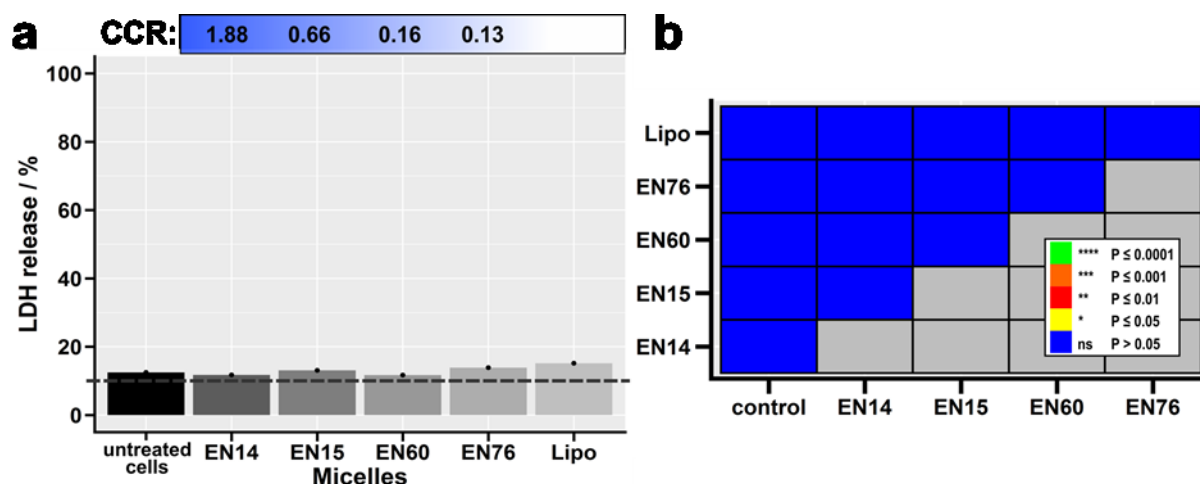
Figure 3.8. All polyplex micelles with different CCR exhibited insignificant cytotoxicity compared to the untreated cells. (a) Lactate dehydrogenase assay of all CCR micelles and positive control Lipofectamine^{TM} 3000 (Lipo) with a concentration of 200 nmol L^{-1} and 100 nmol L^{-1} in Hela cells for 24 hours. Results were obtained from at least three duplicates. The horizontal line indicates 10% of LDH release. **(b)** Statistics heatmap evaluated from Pairwise Wilcoxon (Rank Sum) test, alpha = 0.05, Benjamin-Hochberg Test correction. Significance level, ****P≤0.0001

Cellular uptake evaluation of the micelles was performed over a series of time points to investigate their ability to facilitate cell internalization, effectively deliver their cargo,

and further induce RNAi. Micelles formulated with Cy3-labelled siRNA (Cy3-siRNA) had been transfected into Hela cells. Flow cytometry investigated the quantification of Cy3 fluorescent signal in the cells after 1, 4, 12, and 24 h. Figure 3.9 depicts the mean fluorescent intensity of each micelle in Hela cells at different time points after transfection. EN76 and EN60 with a low CCR ratio, i.e., interrupted PEG corona (as shown in DPD results in Figure 3.7), exhibited higher uptake by Hela cells, comparable to the positive control, Lipo (Figure 3.9). Whereas EN14 and EN15 with the higher CCR show a lower mean fluorescent intensity in Hela cells. Overall, even though the efficacy of cellular uptake of all the polyplex micelles varied, they are capable of cell internalization.
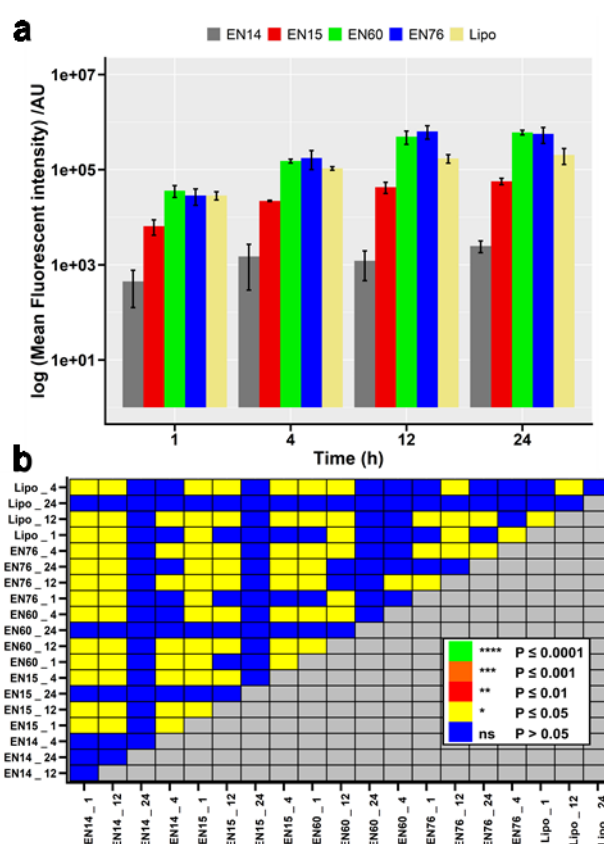
Figure 3.9. Corona: core ratio (CCR) significantly influenced the cellular uptake efficacy of the Cy3-siRNA micelles. (a) The cellular uptake ability of all polyplex micelles and positive control Lipofectamine^{TM} 3000 (Lipo) complexed with Cy3-siRNA. These micelles were transfected with 200 nmol L^{-1} (polyplex micelles) and 100 nmol L^{-1} (Lipo) into Hela cells for 1, 4, 12, and 24 hours. The value was represented in mean ± SD with at least three duplicates. **(b)** Statistics heatmap plotted from the outcome of Pairwise Wilcoxon (Rank Sum) test, alpha = 0.05, Benjamin-Hochberg Test correction. Significance level, ****P≤0.0001

Cellular uptake is only one step in the delivery process of siRNA into the cytosol. To further verify whether the polyplex micelles are efficient in facilitating the therapeutic pathway, we quantified the gene silencing ability of these polyplex micelles using Toll-Like Receptor 4 (TLR4) as a marker gene for the RNAi efficacy. HeLa cells transfected with the micelles complexed with a siRNA against *TLR4* were harvested and analysed after 12, 24, or 48 h. The mRNA expression was quantified using a one-step RT-qPCR. First, the mRNA expression of *TLR4* was normalized to the expression of *TCF7L2* as the reference gene (Wang and Xia 2016, Zhou et al. 2017) which had been identified from a reference gene screening of different gene (*HMBS*). The knockdown is then expressed as a $\log_2$-fold change in comparison to untreated controls. Transfection with commercial Lipofectamine^{TM} 3000 (Figure 3.10, Lipo) served as a positive control. EN15 micelles showed nearly 50% reduction of mRNA expression at all times, even at the first time points 12 hours, indicating a fast release and gene interference property of EN15. RNAi for EN60 and EN70 was more pronounced than for EN15, which might result from the reduced uptake due to a better PEG-shielding in EN15 (Figure 3.10). EN14 showed only slight gene silencing efficacy at all three-time points. The outcome of EN14 may be due to the larger distribution (DLS results in Figure 3.4) of the particle size, as indicated in PDI value (Table 3.2), which results in less uptake of more giant aggregation, lowering the gene delivery capability. The qPCR results confirmed the effective gene delivery and interference ability of EN15, EN60 and EN76, knockdown from 1 to 3 $\log_2$ fold change.
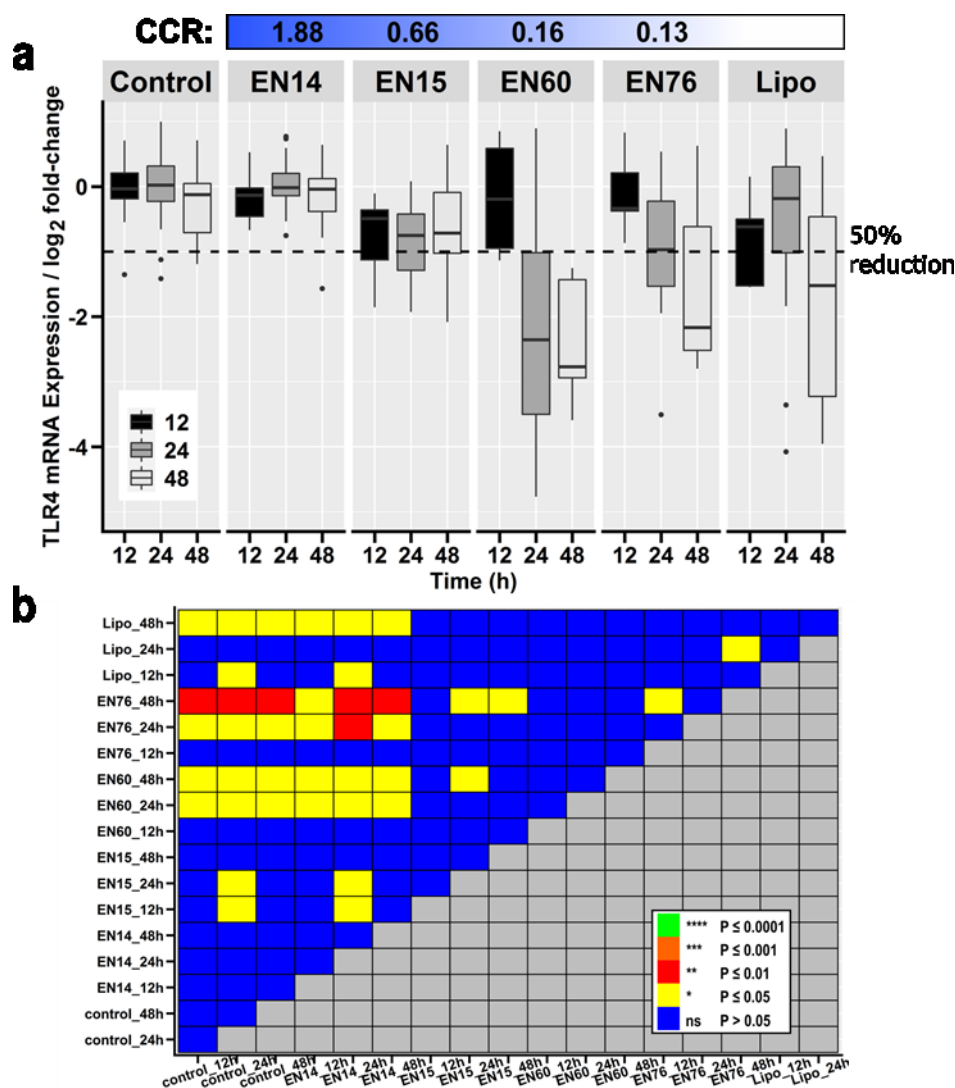
Figure 3.10. *In vitro* comparison of the RNA interference performance between polyplex micelles with different corona:core ratios (CCR) (a) *TLR4* mRNA expression evaluating in HeLa cells at different time-points after their transfection with EN14, EN15, EN60, or EN76 loaded with a siRNA against *TLR4* (siTLR4). Gene expression was normalized against a *TCF7L2* as a reference gene and compared to non-transfected controls. Lipofectamine[TM] 3000 (Lipo) served as a positive control. The quantification of *TLR4* mRNA was done in at least 5 replicates in each sample group, and the expression changes were presented as a Tukey-box plot. The precise number of replicates is given in Appendix Table A1. **(b)** A significance level of the *TLR4* mRNA expression analysis was evaluated in HeLa cells at different time points after transfection of all micelles and Lipo. Statistics heatmap obtained from Significant test by Pairwise Wilcoxon (Rank Sum) Test, alpha = 0.05, Benjamin-Hochberg Test correction. Significance level, ****$P \leq 0.0001$.

3.6 Altering CCR influenced the *in vivo* biodistribution profile and elimination route of siRNA polyplex micelles

Besides the parenchymal cells hepatocytes, the non-parenchymal cells, particularly LSEC and KC, make up the most considerable fraction of the liver's reticuloendothelial system (RES). Together these cells may trigger a local or systemic immune response to protect the hepatocytes from foreign bodies. To investigate all polyplex micelles' passive targeting and biodistribution profiles with different CCR, we performed intravital microscopy (IVM) imaging on FVB/N mice's liver. Micelles complexed with Cy3-labelled siRNA were injected intravenously to the mice after 1 min of baseline image acquisition, followed by 45 min time-lapse imaging. Hepatocytes were identified by their autofluorescence (blue), giving rise from NAD(P)H at 405 nm illumination, while vessels are recognized as the dark region at the same illumination wavelength. IVM images depict that EN14 and EN15 with higher CCR accumulate passively in hepatocytes within 15 min. EN60 and EN76 with lower CCR ratio were recognized and captured by circulating immune cells and KC (Figure 3.11 a). Two features determine the hepatocellular uptake: (1) an overlay of the Cy3 fluorescence with the NAD(P)H autofluorescence of hepatocytes; (2) the appearance of line-patterns in between hepatocytes, resembling canaliculi, a duct of approximately 1 μm in diameter (Boyer 2013) and also the first section of the biliary system, which hepatocytes use to eliminate endo- and xenobiotics. Circulating immune cells were identified in time-lapse images by their movement, while KC remained immobile within the imaging period (Figure 3.11 b). The hepatocellular fluorescence was quantified by an automated image algorithm that segments the tissue through its autofluorescence, subtract the canalicular line patterns, and analyse Cy3 fluorescence over time (Appendix 7.3). The area under the curve (AUC) of Cy3 fluorescence intensity in hepatocytes was calculated for each kinetic curve (Figure 3.12 a) over 30 min. The AUC, *i.e.*, the uptake of Cy3 micelles in hepatocytes, reveals a descending trend with lowing micelles CCR (Figure 3.12 b). EN60 and EN76 show significant lower uptake than EN15.

Further increasing the CCR from EN15 (CCR = 0.66) to EN14 (CCR= 1.88) do not show any significant increase in accumulation of the micelles in hepatocytes. Moreover, the maximum Cy3 fluorescence intensity captured in hepatocytes from the

kinetic curves was lower in EN76 with a low CCR than EN15 (Figure 3.12 c). In the analysis of Kupffer cells uptake, the same kinetic curve as hepatocytes was evaluated (Figure not shown), and the quantification of the AUC over 30 min were also calculated (Figure 3.13 a). The AUC result on KC kinetic curve reveals a higher mean fluorescent intensity of EN76 in KC than EN15 and the lowest at EN14, indicating the higher CCR of the polyplex micelles significantly prevented the uptake by KC and circulating immune cells.

Liver sinusoids could be recognized by the dark region between hepatocytes with strong NAD(P)H autofluorescence. Thus, the retention profile of each polyplex micelles in sinusoids could also be quantified with the automated image algorithm. The AUC value measured in vessels over a time duration of 45 min indicated EN15 possessed a longer circulating time in the blood (Figure 3.13 b). While EN76 exhibited a shorter plasma half-life, implying higher uptake of these polyplex micelles by circulating immune cells or KC. However, the same phenomenon as hepatocytes uptake observed on EN14, further increasing the CCR, does not significantly enhance the blood retention profile.
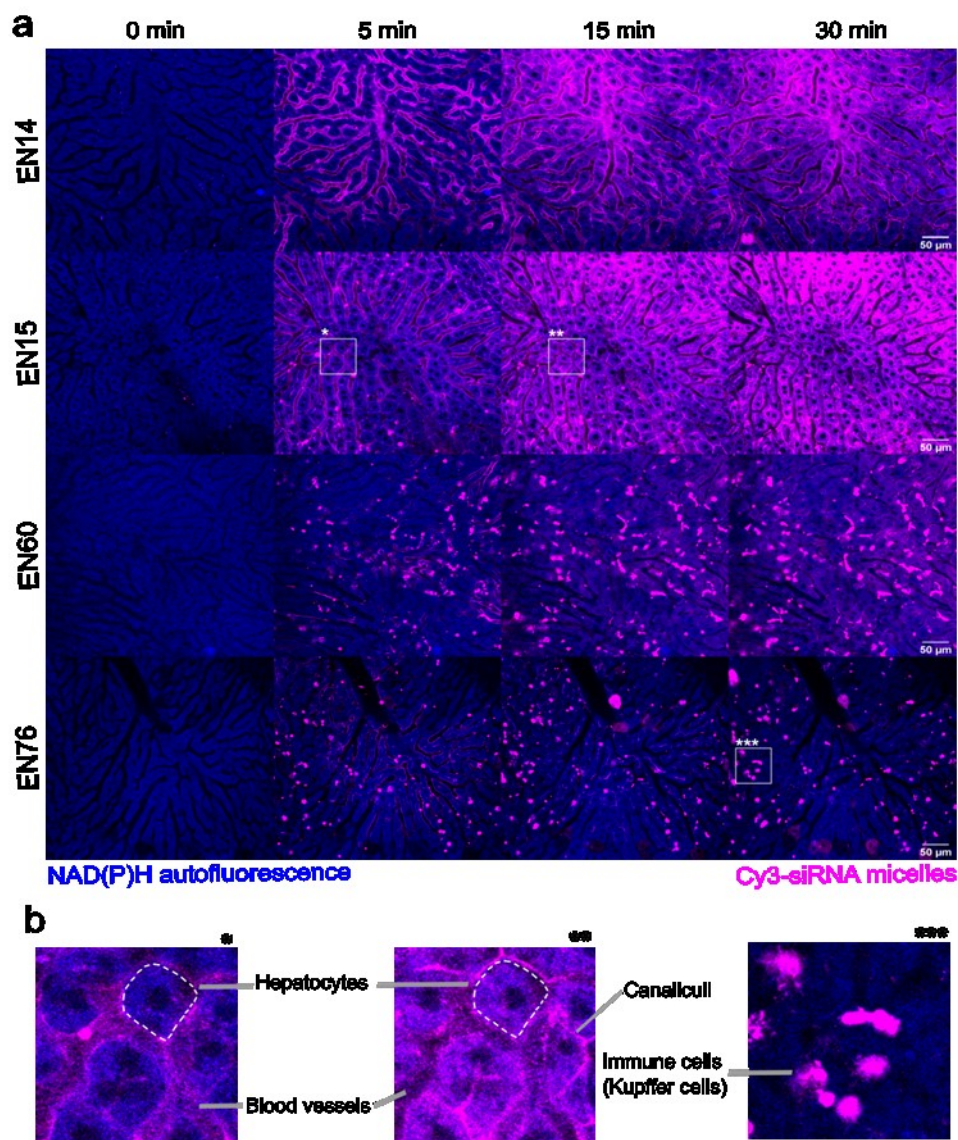
Figure 3.11. The corona: core ratio (CCR) affects the accumulation profile of the Cy3-siRNA polyplex micelles in the liver. (a) Intravital microscopy imaging of the liver. All polyplex micelles were complexed with Cy3-labelled siRNA and are injected through a tail vein catheter. A representative set of images from a time series (0 min, before injection to 30 min after injection) is presented. Hepatocytes are identified by their strong NAD(P)H autofluorescence (blue). Cy3-siRNA micelles are displayed in magenta. Images show a distinct distribution profile of different polyplex micelles in the liver. Different cell types in the liver took up Cy3-siRNA micelles with different CCR. EN14 and EN15 exhibit a preferably hepatocytes uptakes and accumulation in canaliculi, while EN60 and EN76 were captured mainly by Kupffer cells. **(b)** Magnification of some representative aerials in the images, depicting hepatocytes, blood vessels (sinusoids), the post-hepatocellular canaliculi (indicating elimination of Cy3), and immune cells in particular Kupffer cells (local macrophages).
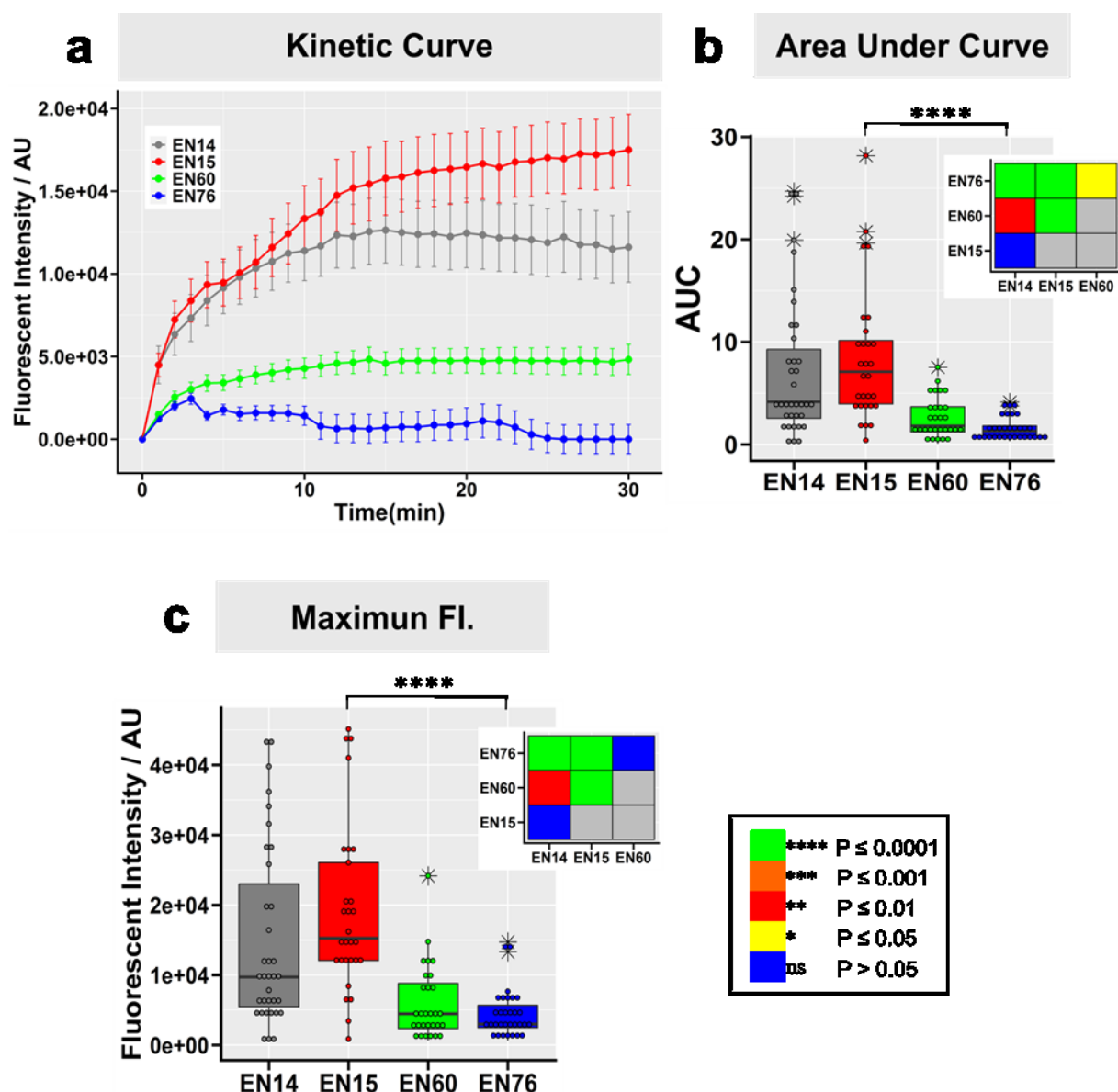
Figure 3.12. The corona: core ratio (CCR) controls passive targeting of Cy3-siRNA polyplex micelles towards hepatocytes. Image analysis of intravital time-lapse microscopy on hepatocytes using the automated algorithm (Appendix 7.3) (a) Kinetic curve of Cy3-siRNA signal captured in hepatocytes for 30 min. Data are depicted as mean ± SD. **(b)** The area under the curve (AUC) is calculated from the kinetic curve. **(c)** Maximal Cy3 fluorescence intensity in hepatocytes. The maximal fluorescence intensity was reached after roughly 30 min. All the experiments were performed at least five animals in duplicates for each polyplex micelles. Inset figures show the significant level between every sample. The significant test is performed using Pairwise Wilcoxon (Rank Sum) Test. Significance level, ****P≤0.0001
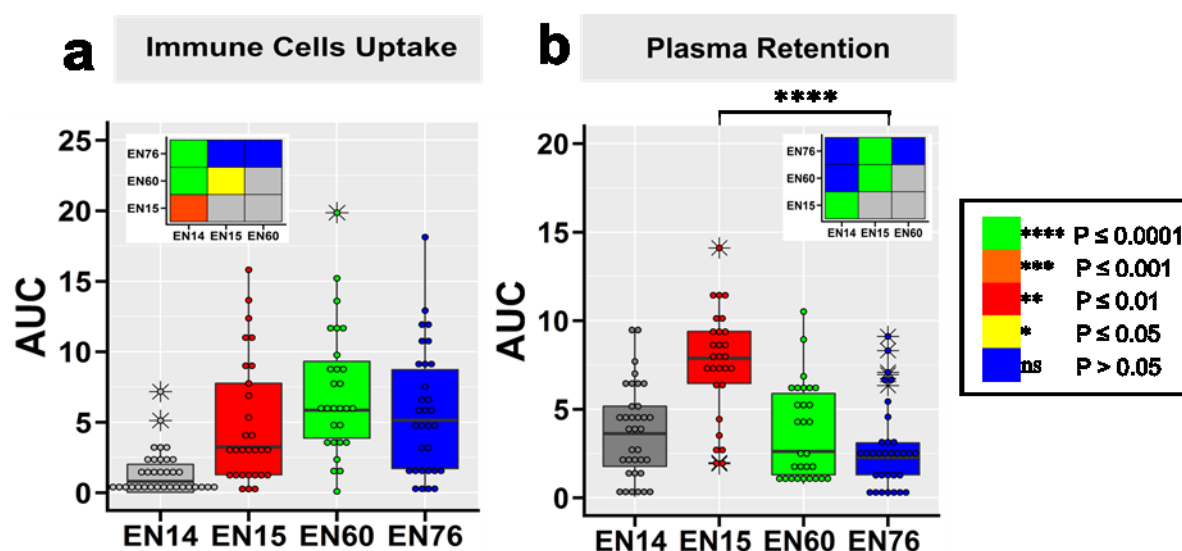
Figure 3.13. The blood circulation profile of Cy3-siRNA polyplex micelles and their recognition by immune cells are strongly influenced by the CCR. Quantification of the Cy3 fluorescent signal in immune cells and retention in blood circulation were analysed using the same automated algorithm (Appendix 7.3). Data were presented in the area under the curve (AUC) (a) AUC of Cy3-siRNA signal in by immune cells (Kupffer cells) for 30 min. **(b)** The plasma retention of Cy3-siRNA micelles is given as AUC over 45 min. All the experiments were performed at least three times in duplicates. The significant level of each sample is displayed in the inset figures. The significant test is performed using Pairwise Wilcoxon (Rank Sum) Test. Significance level, ****$P \leq 0.0001$

3.7 Mesoscopic cryo-imaging as a new method in tracking fluorescent markers

3.7.1 Development of an automated multi-colour mesoscopic imaging technique

Confocal fluorescent microscopy provides high-resolution images in evaluating the biodistribution profile of polyplex micelles down to intracellular levels. (Section 3.6) However, it is still difficult to conclude the accumulation profile of polyplex micelles across different organs. Picturing several organs using IVM concurrently with one administration of polyplex micelles is impossible due to conventional fluorescent microscopy's limited field of view (FoV). Thus, we developed an automated mesoscopic imaging system that allows multi-sectional imaging of whole mice.

This mesoscopic add-on is equipped with a monochrome charge-coupled device (CCD) camera with 4500 x 3600 pixels, 6 μm pixel size, and fair NIR quantum efficiency of 30% at 800 nm (Figure 3.14). The high-resolution camera and all the filter sets are mounted on a self-designed stage which can be easily attached and removed from the cryo-microtome. The lens and camera were constructed on a motorized stage which the focus plane on the sample could be easily controlled by the in-house developed acquisition software. The software was designed to control the camera and cryo-microtome through the Arduino Mega 2560 Rev3 microcontroller. The optical focus were optimised by adjusting the yaw and pitch control of the motorized stage. The acquisition software could also provide instructions for fine-tuning through calculating the focal plane angles from three preselected positions on the samples. The camera lens with a ± 58 μm depth of field (using f/4.8 and assuming 6 μm as acceptable circle diameter of confusion) combined with 34 mm field-of-view diameter require a very straight alignment between the lens and the samples.

After adjusting the focus, high-resolution fluorescent and white light imaging were done concurrently during the cryo-sectioning procedure, without extensive pre-processing, tissue slicing, and mounting for fluorescent microscopy imaging. The whole process was controlled by the acquisition software and ran automatically. The complete automated process eased the process of imaging large sample blocks. Hundreds of images could be taken unattended without the intervention of the user. The cross-sectional view of the whole mouse with different organs on the same planar was observed under this mesoscope. The analysis and visualization of biomarkers in various organs are done within one single image and further improved the accuracy of fluorescent signals' quantification. This mesoscopic imaging system can investigate a wide range of fluorescent probes by replacing the filter set on the mesoscope. Two LED light sources were equipped on this system, allowing imaging fluorescence in visible and near-infrared (NIR) ranges.
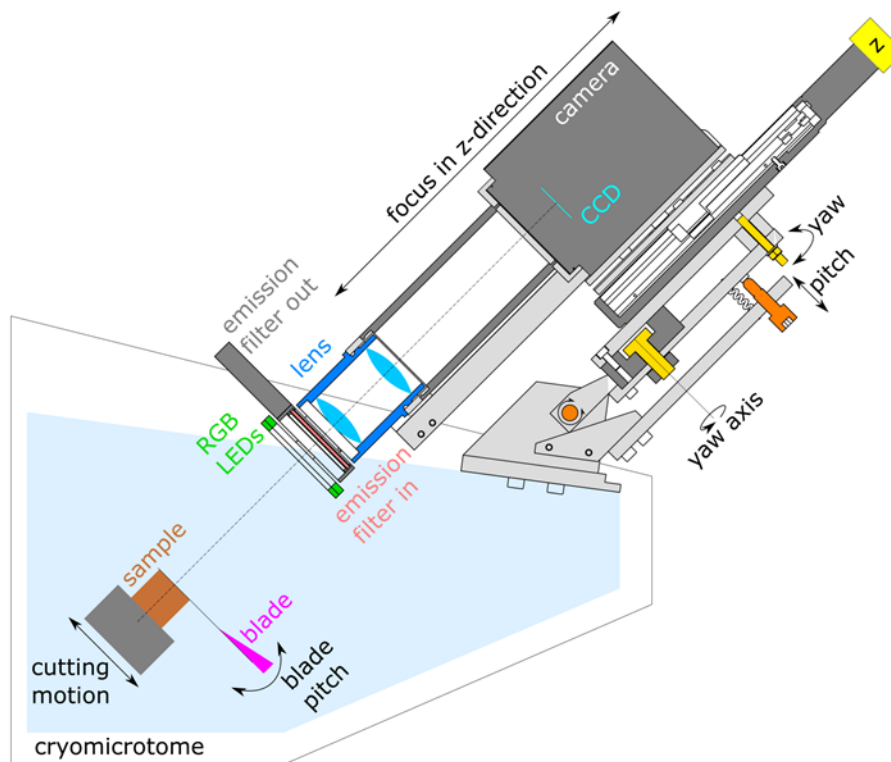
Figure 3.14: Schematic drawing of the mesoscopic imaging instrument set up in a graphically depicted cryomicrotome. The mesoscopic imaging system is composed of a monochrome CCD camera (sensor cyan) with 16 M pixel; a 1:1 macro lens with 89 mm focal length using f/4.8 ≈ 0.10 NA (blue), a switchable emission filter (red), an RGB LED ring for colour images (green), a filtered high power LED for fluorescence excitation (not shown), a focus motor stage (yellow z-nob), a self-made base with pitch (orange) and yaw adjustment (golden). Customized fabricated segments are displayed in light grey, and commercial purchased parts are shown in dark grey. The cryo-microtome (a chamber in light blue) features a blade (magenta) and the motorized sample holder with the sample (brown). Arrows indicate the possible direction of movement.

Once the frozen mice samples were mounted on the cryostat, the software fully automated cryo-sectioning and imaging. All image acquisition variables, including sequencing of imaging, numbers of images taken, and brightness of RGB channel, are changeable using the software. Focus and brightness were optimized before the cutting and could be maintained throughout the whole cutting loop. RGB images with high-resolution taken from different sections of the mouse are displayed in Figure 3.15. All main organs of the mouse, such as the heart, liver, lung, stomach, intestines, spleen, kidney and bladder, can be visualized from the cross-sectional views. Smaller tissue, including the trachea, blood vessels, bone, and gallbladder, can also be

observed easily from the anatomy images (Figure 3.15 inset figure * & **). Furthermore, detailed structures in the organs are well captured, for instance, the microvascular in fat tissues, the intestinal villi and the red/white pulp of the spleen (Figure 3.15 inset figure *** & ****). The high-resolution images can also image the inner structure of the kidney (cortex) and stomach (rugae) (Figure 3.15 c).

.
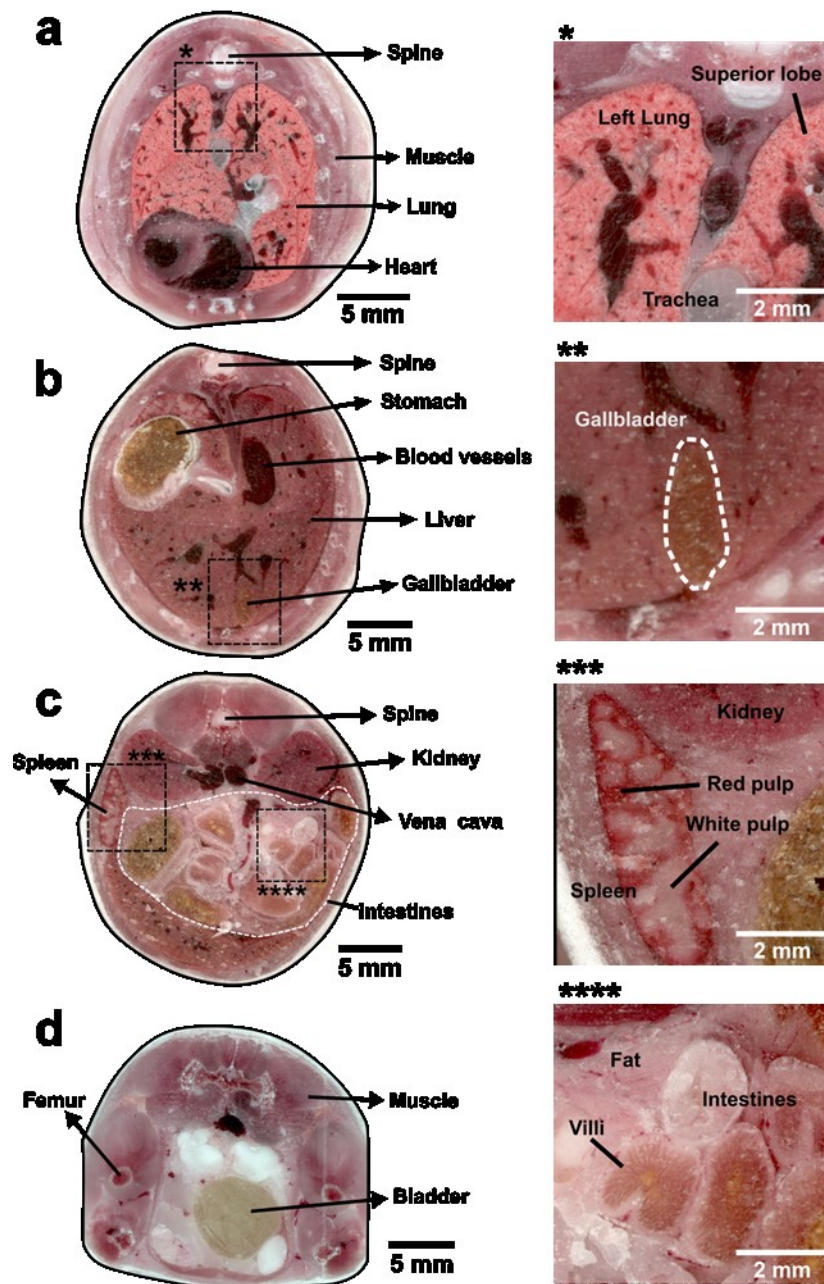
Figure 3.15. The mesoscope imaging system well resolves the anatomy of a mouse. Continuous anatomical cross-sections were imaged automatically during cryo-sectioning. Images depict cross-section views of different mouse's organs to elucidate the resolution. **(a)** Thorax of a mouse, displaying the lung and heart surrounded by the rid bones. *Enlarged regions depict the lung and trachea. **(b)** This mesoscopic camera captures the upper abdomen with the main organ, *i.e.*, stomach and liver and the hepatic artery are visible in the liver; **Zoomed figure shows a clear gallbladder filled with bile acid. **(c)** Lower abdomen with various organs, kidneys, intestines, spleen and vena cava. ***White and red pulp of the spleen can be differentiated. **** Villi in the small intestines and smaller blood vessels inside the fat tissue surrounding the intestines are resolved. **(d)** In the pelvic region, the image displays a urine-filled bladder.

3.7.2 Mesoscopic imaging with advanced benefits in tracking fluorescent markers in different organs and provides high-resolution anatomical images

This automated multicolour mesoscopic imaging system supports direct tracking and imaging fluorescent dyes and markers in various organs on a large scale. Thus, to further confirm the *in vivo* distribution profile and investigate the clearance pathway of the polyplex micelles, we utilized this mesoscopic imaging technique in tracking the elimination route of EN15 and EN76, which have shown the most significant differences in IVM. Cy5-siRNA was selected in this experiment to complex micelles with both diblock copolymers due to overlapping of Cy3 fluorescence signal with the autofluorescence of bile acids and mice food in the stomach. 15 and 45 min after the intravenous injection of Cy5-siRNA complexed EN15 and EN76 polyplex micelles, and mice were euthanized and frozen. In order to trace the signal of Cy5, a filter set with excitation at 625 nm and emission at 670 nm was used to visualization the accumulation profile of Cy5-siRNA complexed polyplex micelles. Besides the fluorescent images, RGB images on the tissue anatomy were acquired to confirm the areas of fluorescent signal (Figure 3.16). Cross-sectional images were acquired at desired sections including thorax, upper and lower abdomens for at least 15 slices, with a thickness of 100 μm for each slice, quantifying the fluorescent signal over organ segment with the thickness of at least 1.5 mm.

The quantification of Cy5 fluorescence intensity on the images revealed that EN15 polyplex micelles significantly accumulated in the gallbladder and kidney, implying the preferable elimination of this micelle through both hepatobiliary and renal routes. However, the Cy5 fluorescence signal in liver tissue was low compared to the fluorescence in the gallbladder and intestine. The low signal may be due to polyplex micelles' distribution on a big liver mass during biotransformation, while the Cy5 signals are relatively concentrated in the bile and intestine during elimination (Figure 3.16 & 3.17). A substantial increase in the Cy5 fluorescence signal was observed in the urinary bladder while the reduced signal in kidney over the time. Cy5-fluorescence signal was barely observed in other RES rich organs, such as spleen and lung tissue when injecting both EN15 and EN76 (Figure 3.16 & 3.17).

In contrast, EN76 micelles exhibit only little accumulation in the hepatobiliary system (liver, gallbladder, intestine) and no elimination through the renal system (*i.e.*, kidney and urinary bladder) (Figure 3.17). Therefore, a relatively homogenous increase in fluorescence intensity in most tissues is observed in the images (Figure 3.17), supporting the observations from IVM that EN76 is rapidly captured by circulating and tissue-resident immune cells. Furthermore, the fluorescent intensity ratio between liver and kidney for EN15 and EN76 at 15 min and 45 min confirmed the previous outcomes in which EN15 was eliminated mainly by the hepatobiliary clearance pathway (Appendix 7.1 Figure A1).
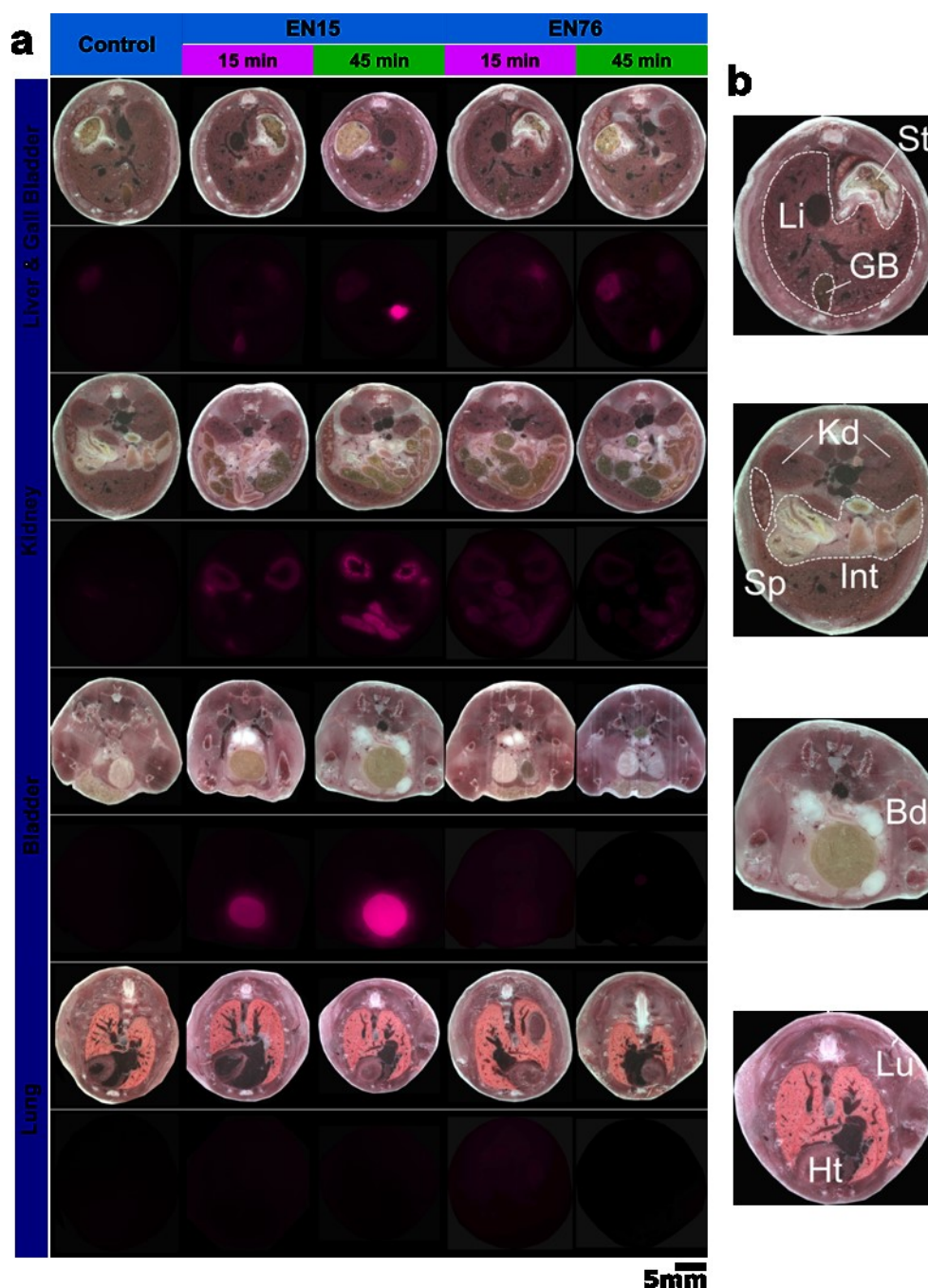
Figure 3.16. The corona:core ratio (CCR) significantly altered the clearance pathway of Cy5-siRNA micelles. (a) Cross-sectional anatomical RGB and full fluorescence images of different mice sections from cryo-imaging. EN15 and EN76 complexes with Cy5-labelled siRNA are injected through a tail vein catheter. Mice were euthanized at 15 and 45 min after injection of the Cy5-siRNA polyplex micelles. The accumulation profile of the EN15 and EN76 in different organs is identified by the Cy5 fluorescence signal (magenta). EN15 shows preferably accumulation in gallbladder and kidney, clearly follow hepatobiliary and renal clearances pathway. The Bladder of mice injected with EN15 shows a robust Cy5 signal after 45min. **(b)** Representative anatomical RGB-images of different mouse cryo-sections with annotation of St: stomach, Li: Liver, GB: Gallbladder, Kd: Kidney, Int: intestines, Sp: Spleen, Bd: bladder, Lu: lung, Ht: heart
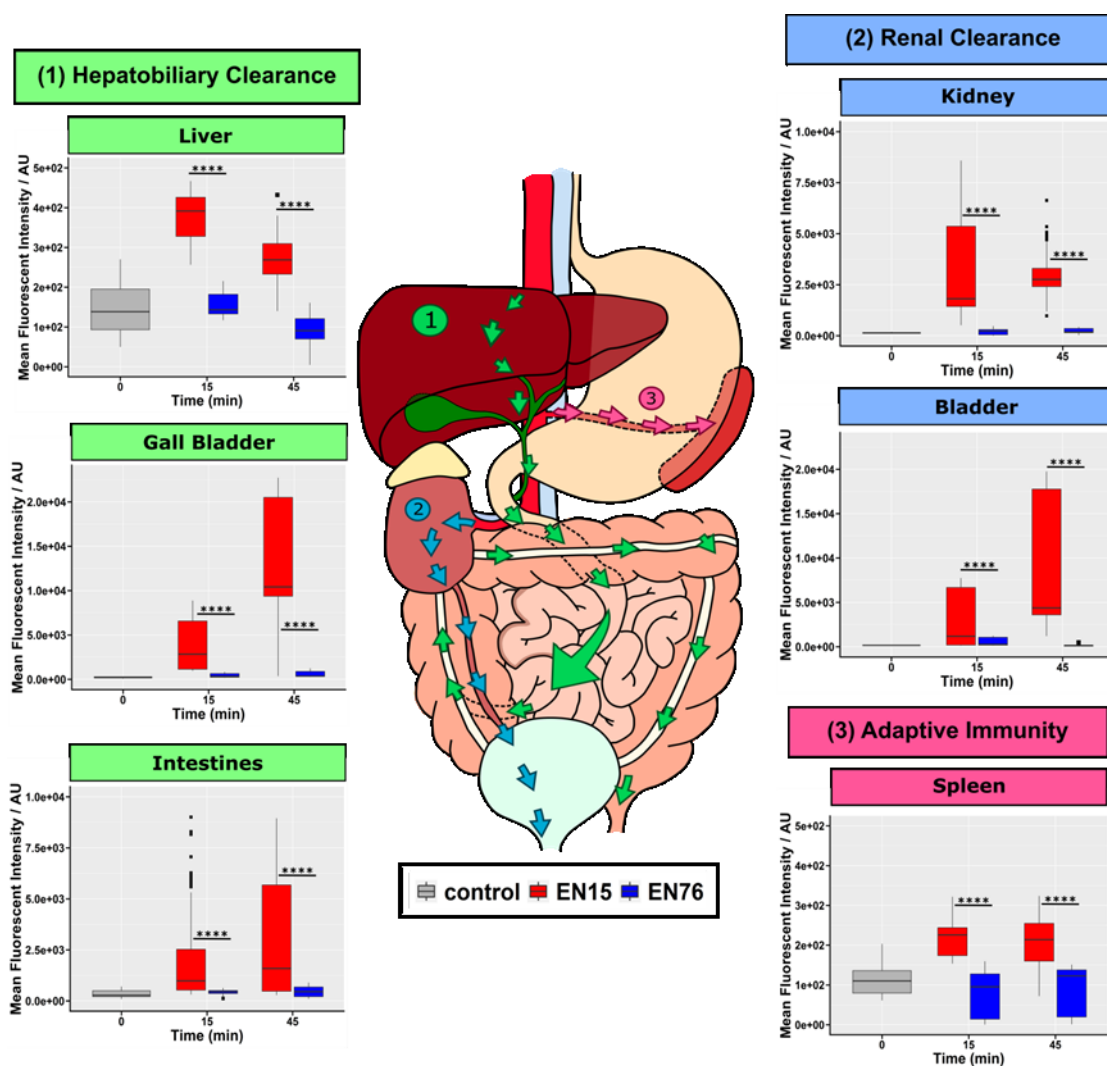
Figure 3.17. Quantification of the Cy5 mean fluorescence intensity in significant organs involved in the sequestering and excretion of nanocarriers. The schematic graph illustrates the general elimination route of nanoparticles after intravenous administration. (1) Hepatobiliary clearance pathway (liver, gallbladder, intestine). **(2)** Renal clearance (kidneys, urinary bladder). **(3)** Sequestering by cells of the adaptive immune system (spleen). The significant test is done by Pairwise Wilcoxon (Rank Sum) Test. Significance level, ****$P \leq 0.0001$

4.   Discussions

The mortality rate caused by liver diseases is now accounted for more than 3.5% of all global deaths, which have risen intensively between the years 2000 and 2020. (GBD 2018, Böttger et al. 2020) Liver diseases have recently become a significant global health burden with approximately 800 million cases per year worldwide. (Byass 2014, Marcellin and Kutala 2018) However, the therapeutic approaches and active target sites for drug or therapeutic genes are often varied depends on the different liver diseases. Liver parenchymal cells, *i.e.,* hepatocytes, are the primary cellular target to treat viral hepatitis (mainly HBV) (Asrani et al. 2019) as well as metabolic derangements, covering a broad range of diseases from rare inborn errors of metabolism to, *e.g.* hypercholesteremia (Sehgal et al. 2013) and life-threatening infections (sepsis (Press et al. 2021)). At the same time, non-parenchymal hepatic stellate cells (HSC) are the leading target site for a chronic liver disease characterized by accumulation of extracellular matrix and fibrosis. (Bauer et al. 2013) Thus, without cell type-specific delivery, the effectiveness of the drugs or therapeutic genes may compromise and induce unwanted hepatoxicity.

Among all kinds of treatments for liver diseases, RNAi therapy has been developing extensively in recent decades as a new candidate of therapeutics gene to interfere with the expression of disease-related genes. Synthetic siRNA has been reported in successful silencing towards various target genes *in vivo* for a broad range of liver diseases, for example, cirrhosis (Sato et al. 2008, Whitehead et al. 2009), HBV (Morrissey et al. 2005), and acute hepatic porphyria (Agarwal et al. 2020, Balwani et al. 2020) . RNAi therapeutics has been proven as a high potential therapeutic approach for liver diseases. The applicability and efficacy of RNAi as an effective clinical drug have been further confirmed when the first FDA approved siRNA drug ONPATTRO® (Patisiran, ALN-TTR02) by Alnylam Pharmaceutical was launched in 2018. (Morrison 2018, Mullard 2018, Akinc et al. 2019)

Up to date, the siRNA drugs that are commercially available on the market or undergoing clinical trials are mainly fabricated by lipid platform with PEGylation.

(Morrison 2018, Mullard 2018, Akinc et al. 2019, Zhang et al. 2021) Conventional liposomal nanocarriers, the most extensively studied and applied drug/gene delivery system in the past few decades, often accompanies by the limitation of precise and multiple-step synthesis process as well as least versatility in chemical modification. The production of lipid nanoparticles usually requires time-consuming procedures, including catalyst removal, solvent exchange, chemical deprotection, and purification. (Simões et al. 2005) Moreover, some evidence has also suggested that lipid modulated siRNA carriers might induce unwanted innate immune responses, *e.g.* reflected by increased cytokine release. (Whitemore et al. 1999, Judge et al. 2005) Despite the well-established lipid-based gene delivery systems, polymeric carrier systems with PEGylation reflect as another promising nanocarriers system for delivering genes. Polymeric carrier systems with PEGylation, in recent years, have been shown to effectively reduce the undesirable opsonisation that could further increase the stealthiness and retention ability of the nanoparticles in the bloodstream. (Mosqueira et al. 2001, Tockary et al. 2019)

Polymeric micelles prepared by self-assembly of block copolymers with therapeutic genes reflect promising nanocarrier systems for DNA/RNA delivery. The delivery efficiency of polymeric micelles depends on their physicochemical properties, which govern the interaction between nanocarriers and local tissue environments. Extended circulating profile, or more precisely, low recognition and clearance by immune-competent cells, is a measure that determines delivery efficacy. (Li et al. 2020) The gene delivery system's size, shape, and surface charges play an important role in determining the circulation profile after systemic administration. (Zhang et al. 2016, Cabral et al. 2018) The power of such effects is crucial for the formulation and translation of polymeric micelles. It might be even explored to achieve a passive targeting based on conformational effects, which resulted from varying protein-adsorption to the nanocarriers (protein-corona). (Chen et al. 2020) In general, the liver will eventually clear nanocarriers with unfavourable properties. Therefore, targeting delivery to the liver is often misunderstood as an easy-to-reach goal. In the liver, nanoparticles are mostly recognized immediately by the immune-competent local macrophages, the Kupffer cells and LSEC, which otherwise protect the hepatocytes from pathogens and nanocarriers. (Li et al. 2020) Thus, to facilitate an effective

nanocarrier for therapeutic siRNA in selective targeting hepatocytes behind this high effective reticuloendothelial barrier, design intelligently the physicochemical properties of the nanocarriers is crucial.

We have previously demonstrated that the structural properties, surface charges, and the interaction between carrier and cargo during encapsulation significantly influence the formation of nanocarriers and further their drug release and distribution profile. (Rinkenauer et al. 2015, Press et al. 2017b) Yet, there are still limited numbers of works reported investigating the effects of PEGylation degree on nanocarriers toward hepatic distributions. Herein we developed a series of siRNA polyplex micelles formed using a simple diblock copolymer system with PEG as a hydrophilic block and PAGE as a segment for subsequent cationic binding sites. PEG-*b*-PAGE have been published with their superior ability in drug and siRNA encapsulation, good *in vitro* cellular uptake, and gene interference. However, there is still lacking of detailed reports discussed on their *in vivo* distribution profile in the liver and how the characteristic of this polymer platform affect their *in vivo* PK/PD behaviours.

In this proposed PEG-*b*-PAGE system, the modified PAGE segments with amino groups allow polyion complexation with anionically charged siRNA, forming the core of the polyplex micelles with PEG as a corona. Four diblock copolymers, *i.e.,* EN14_poly, EN15_poly, EN60_poly, EN76_poly were carefully synthesized with different molecular weights of PEG in combination with varying degrees of polymerization for PAGE and were well characterized by SEC and ^{1}H NMR (Figure 3.2). The different molecular weights of PEG and a varied number of PAGE$_{NH2}$ blocks allowed the forming of siRNA polyplex micelles with different corona (PEG): core (PAGE) ratio (CCR). With the relative higher content of PEG and shorter PAGE chain, polyplex micelles EN14 and EN15 exhibit higher CCR than EN60 and EN76 with longer PAGE chain with relative lower content of PEG. In this regard, EN14 depicts the highest CCR (1.88), followed by EN15 (0.66), and EN60 and EN76 have the lower value (016 and 0.13 respectively) (Figure 3.1).

Our studies on characterizing the physicochemical properties of these four proposed polyplex micelles with different CCR reveal a precise result in sizes, zeta potentials,

the signatures in Raman spectra, PCA analysis, and *in silico* DPD simulation. It is confirmed that, by simply altering the length of the base polymer blocks and Mw of PEG, the resulting polyplex micelles exhibit significant differences in their physical properties, thus determining factors affecting their PK/PD. The hydrodynamic diameters of the three polyplex micelles prepared with PEG M_n of 2000 g mol^{-1} (70 nm for EN15, around 100 nm for EN60 and EN76) (Table 3.2) are below the diameter of the reported sinusoid fenestration in the liver of 150 - 175 μm. (Braet and Wisse 2002, Cogger et al. 2015) However, further increase the PEG content by using PEG with M_n of 5000 g mol^{-1}, an average diameter of EN14 at 350 nm with a considerable PDI value of 0.51 was observed, indicating uneven size distribution (Figure 3.4 a). Similar results were also reported in increasing PEG with remaining the same length on the second polymer block results in more giant polyplex micelles and broader size distribution. (Takeda et al. 2017a) This may be due to the repulsive force between the PEG chains when complex into polyplex micelles. (Osada et al. 2010, Tockary et al. 2016) Access amount of PEG in forming polyplex micelles may also result in free polymers (smaller in size) and possible aggregation (substantial size increase), implying the first peak and third peak respectively in size distribution curve of EN14 (Figure 3.4 a). The result of zeta potential with a lower value at 10 mV, further confirms possible aggregation in EN14. The other polyplex micelles (EN15, EN60 and EN76) exhibit zeta potential around 30 mV, a value that generally indicates the stability of suspension to resist coagulation and aggregation. (Foujdar et al. 2020)

The degree of PEGylation on polyplex micelles is always addressed in PEG density that calculated by the size, the thickness of the PEG shell, the surface area and the polymer binding number of the polyplex micelles. (Osada et al. 2010, Perry et al. 2012, Rabanel et al. 2014, Tockary et al. 2016) It is important to note that the nanoparticles reported were relatively larger in size (bigger than 200 nm) or having a bigger and solid core (inorganic substances, pDNA) of the nanoparticles. Therefore, with a very short oligonucleotide (22 bp) compared to pDNA with few thousands basepairs, the core is relatively small and difficult to observe even though cryo-TEM. Calculation using the thickness and the surface area of PEG is not feasible. Thus, to address this characteristic, we defined the corona-core ratios of each type of polyplex micelles by the ratio of M_n between the PEG and PAGE$_{NH2}$ block from corresponding PEG-*b*-

PAGE$_{NH2}$ diblock copolymers. To validate our assumption CCR, we subjected all the polyplex micelles to Raman spectroscopy and analysed the peak area ratio between PEG and PAGE of each polyplex micelle. Raman spectroscopy has been widely established as a characterization approach to distinguish vibrational modes of a bond between atoms and provide structural fingerprints information of macromolecules. (Castiglioni et al. 1993, Muljajew et al. 2021) The orientation and complexation highly influence the frequency and amplitude of this molecular vibration. The Raman peak is unique for each molecular bond; the orientation of the macromolecules will contribute to the signal strength. Thus, both information on the unique molecular fingerprint of the materials and the degree of complexation of certain bonds in macromolecules were obtained by Raman characterization. The relative ratio of the Raman peak intensities provides information about macromolecules' molecular structure within one sample. (Press et al. 2017b) in higher CCR polyplex micelles EN14 and EN15, the vibration peak of siRNA tend to be more suppressed than EN60 and EN76 with lower CCR, indicating a better shielding effect of higher CCR polyplex micelles. Higher Raman Peak intensity on PEG determined peak, and lower intensity on PAGE peak were also observed in EN14 and EN15, further confirmed the significant contribution of PEG content in these polyplex micelles (Figure 3.5 * at 1480 cm^{-1}). While both EN60 and EN76 exhibit an opposite behaviour in higher Raman peak intensity on PAGE peak (651 cm^{-1}) (Figure 3.5 *) with a significant peak of siRNA vibration peak (1036 cm^{-1}) (Table 3.4). All Raman spectra of polyplex micelles, neat polymers and siRNA were subjected to PCA analysis. The PCA results indicated distinct clusters between polyplex micelles, significantly separated along with dimension PC 1 and PC2 with the main contribution of differentiation on PEG vibration determined peak 1480 cm^{-1} and PAGE at 651 cm^{-1}, respectively. The PCA results further confirmed that all polyplex micelles significantly differentiated in respect of PEG and PAGE contributions. Therefore, the peak area of the determined vibration peak of PEG (1480 cm^{-1}) and PAGE (651 cm^{-1}) was evaluated with at least 10 spectra per polyplex micelles. The relative Raman peak areas ratio between PEG and PAGE$_{NH2}$ in one polyplex micelles perfectly reflects with the calculated CCR from M$_n$ of PEG and PAGE$_{NH2}$, except EN14, which can be explained by the inconsistency of the size resulting in different PEG density on the polyplex micelles (Table 3.3).

Moreover, DPD simulations were performed to understand better and further visualize the possibly morphological structure of the polyplex micelles. (Luo and Jiang 2012, Hao et al. 2019) Different modelling structure in all 4 polyplex micelles was observed, as consistent with the findings from PCA (Figure 3.7). In DPD results, EN14 and EN15 with the higher CCR and higher PEG content reveal a thicker and entire PEG corona, better coverage of the PAGE$_{NH2}$ and siRNA core. While EN60 and EN76 show thin layer corona, a disrupted corona in observed in EN76. Simulation results of EN76 reveal destruction in PEG corona integrity results by the big PAGE$_{NH2}$ core, which may further cause exposures of siRNA molecules. The results on the simulated morphological structure of the polyplex micelles are consistent with our finding in Raman peak intensity, in which siRNA peak are more presented in low CCR polymer micelles. It is worthy to note that, the beads displaying in the DPD simulation do not precisely represent the interaction and relations between polymer molecules bonds but rather demonstrate the possible location cloud or arrangement of the specific polymer molecules. Therefore, the DPD results in EN76 do not announce in unsuccessful complexation of the polyplex micelles but rather describe the possible position of siRNA molecules located nearer to the PEG corona than in the middle of the core. Gel retardation assay and EtBr assay have proved the complete complexation of all polyplex micelles with siRNA (Figure 3.3). However, the possible location of siRNA molecules near the surface in EN76 may contribute to the disturbance of PEG corona and could probably propagate the recognition by the reticuloendothelial system.

The surface properties, size, and shape of nanocarriers for DNA or RNA have significantly affected the efficacy of *in vitro* cellular uptake and gene expression/interference. (Tockary et al. 2013, Nuhn et al. 2014, Tangsangasaksri et al. 2016) Dirisala et al. demonstrated that by increasing the PEG density of pDNA polyplex micelles using PEG-PLys platform with same Mw of PEG and different PLys chain, increased the size of the polyplex micelles and thus deteriorated the cellular uptake and gene transfection efficacy. (Dirisala et al. 2014) These findings are consistent with the four polyplex micelles with different CCR. Due to the better shielding on high CCR polyplex micelles, EN14 and EN15 exhibit a slower and low cell internalization compared with the other two, EN60 and EN76 (Figure 3.9). The low

cellular uptake due to the larger diameter of EN14 (360 nm) and their thick PEG corona increased the difficulties of cargo release. EN14 show poor gene silencing efficacy. Nuhn et al. also reported that siRNA encapsulated nanogel with a smaller average diameter size (40 nm) have also been reported to have superior gene silencing efficacy than their larger counterparts (100 nm). (Nuhn et al. 2014) The size effect on gene silencing between EN15, EN60, and EN76 is less pronounced because the size of EN15 (70 nm), EN60 and EN76 (100 nm) are somewhat similar. The variation of their gene silencing ability is mainly accounted on the extent of cellular uptake. Even though EN15 has a low cellular uptake compared with EN60 and EN76, an average of 50% of downregulated mRNA expression from EN15 transfected cells over the three time points is reported, proving sufficient ability of EN15 micelles in cell internalization, endosomal escape and siRNA release (Figure 3.10). EN60 and EN76, with good ability in cell internalization, demonstrated superior gene interference ability in knock down the target gene TLR4. However, *in vitro* study is insufficient to fully explain the uptake ability and accumulation profile of polyplex micelles in the liver during systemic administration.

Most of the gene nanocarriers formulated to express their therapeutic effect in hepatocytes are often sequestered by the local RES (*i.e.,* KC and LSEC), thereby losing their functionality. (Wang et al. 2015) To further demonstrate the effect of CCR on the hepatocyte targeting accumulation and blood circulating profile, the evaluation of *in vivo* distribution profile of these polyplex micelles is therefore performed by intravital microscopy and a new developed mesoscopy imaging technique. The time-lapse IVM imaging results confirmed our hypothesis, owing to the higher corona density or more intact PEG shell, EN15 micelles with the smaller diameter of 70 nm possess preferably accumulation in hepatocyte (Figure 3.12). It has been reported that without any targeting moiety, nanoparticles with the size of over 150 nm are challenging to take up by hepatocytes because the fenestrae pore size of LSEC is around 100 nm-150 nm (Wisse et al. 2008, Zhang et al. 2016) Further increase the CCR as in EN14 with more extensive size distribution, did not show a significant increase in accumulation in hepatocytes than EN15. Due to the uneven size distribution, part of the EN14 with the smaller diameter could still penetrate through LSEC and reach hepatocytes thus, higher accumulation than EN60 and EN76 were

observed (Figure 3.12). Even though the larger counterparts EN60 and EN76 possess a size around 100 nm within the range of fenestrae pore size, their accumulation in hepatocytes is low. EN60 and EN76 were significantly recognized and uptake by KC or circulating immune cells before reaching the hepatocytes (Figure 3.13) due to the lower CCR with more significant cationic charges PAGE core of these polyplex micelles. Nanoparticles with positive surface charges tend to be identified by KC and immune cells. (Zhang et al. 2016) The results showed that the effect of PEG density upfronted the limitation of nanoparticles size in passive targeting hepatocytes. The phenomenon was also shown in EN14; even though the diameter is bigger than EN76, the high PEG content on the shell of EN14 provides a strong shielding effect from KC (Figure 3.13 a).

Since there is no targeting moiety conjugated on the polyplex micelles, the accumulation of polyplex micelles in hepatocytes can only be achieved by passive targeting and cell internalization. Thus increase the blood circulation profile can significantly increase the chance of the polyplex micelles flow toward the hepatocytes. Numerous studies have been published with enhanced blood retention profiles of nanoparticles by PEGylation and increase PEG density. (Fischer et al. 2010, Walkey et al. 2012, Tockary et al. 2013, Dirisala et al. 2014, Cabral et al. 2018, Akinc et al. 2019, Zhang et al. 2021) Our results again emphasized the importance of PEG stealthiness in prolonging the blood circulation efficiency, EN15 with adequate CCR displayed the longest blood circulation among the other polyplex micelles. However, an exception was observed again on EN14; further increasing the CCR did not lead to more prolonged blood circulation, probably caused by the larger diameter of EN14 promoting the clearance by circulating immune cells in the bloodstream (Figure 3.13 b).

IVM using confocal fluorescent microscopy allowed the acquisition of high-resolution images in evaluating the biodistribution profile of polyplex micelles down to intracellular levels. However, it is still insufficient to evaluate the accumulation profile of polyplex micelles across different organs due to conventional fluorescent microscopy's limited field of view. A new developed automated mesoscopic imaging system solved the issue by offering multi-sectional imaging of whole mice. Although

non-invasive approaches such as multi-spectral optoacoustic tomography (MSOT), computed tomography (CT), magnetic resonance imaging (MRI), ultrasound imaging could provide three-dimensional anatomical information in animal models, these approaches are harbouring difficulties in visualizing the detailed structures of the organs or fluorescent tracer distributions. (Terreno et al. 2012) Detailed anatomical images with visualization of a wide range of fluorescence can be obtained by this mescoscopy setup. To further validate the *in vivo* distribution profile in the liver and investigate the clearance pathway of the EN15 and EN76 with the most distinct distribution profile, Cy5-siRNA complexed EN15 and EN76 treated mice were subjected to the mesoscopic imaging. High-resolution multi-sectional RGB and fluorescent images taken on the entire animal section with different organs on the same planar visualized the Cy5 signal in different organs within one single image. This feature effectively reduces the discrepancy of the fluorescent signal between different images and improve the consistency in fluorescent signal quantification. After analysing several slices of mice abdomen, a preferably hepatobiliary clearance for EN15 was discovered, double confirmed the passive targeting capability of higher CCR micelles towards hepatocytes.

Moreover, to better evaluate only the effect of CCR on cell type-specific delivery, we herein simplified the nanocarrier system. In this study, the polyplex micelles are produced without any extra modifications that extensively applied in other siRNA carrier systems, such as endosomal escape (Tangsangasaksri et al. 2016), cholesterol stabilized siRNA used in enhancing interference, conjugation of ligands for better cell-type targeting ability (Wu et al. 2013). Even though *in vitro* experiments show significant cellular uptake and gene interference, the process of systemically administered nanocarriers into the biological body to express their therapeutic effect further is complicated and requires more investigations on other physicochemical properties of nanocarriers. Therefore, further application of these current nanocarriers for *in vivo* silencing has therefore not proceeded.

Nevertheless, the *in vivo* analysis combined both IVM and mesoscopy imaging again proved that the distribution profile does not only rely on single surface property. A good combination of sufficient PEG stealthiness, defined as CCR in this work, and

appropriate size of the nanocarriers are crucial to facilitate a longer circulating time and specific accumulation in hepatocytes. The above findings would serve as a control measure for future alterations on polyplex micelles in surface modification and functionality to facilitate an efficient delivery to target cells. Furthermore, we presented a set of spectroscopic and simulation techniques for analysis of the CCR, opening up a possible solution in evaluating corona stealthiness for future application.

5. Conclusion

The physicochemical properties of nanocarriers are critical for determining efficiency. In this study, we mainly discussed the effect of PEG density, as defined in corona: core ratio (CCR), of a siRNA polyplex micelles on influencing the *in vitro* cellular uptake, gene interference, *in vivo* passive targeting accumulation towards hepatocyte, and the elimination route. In order to validate the CCR in every polyplex micelles, we developed a series of measurement, calculations, and statistically analyses using Raman spectroscopy. The results of Raman spectroscopy validated our calculation of CCR on every polyplex micelles using M_n of the neat polymers. DPD simulation performed on each polyplex micelles revealed that the contents of PEG have a substantial impact on altering the inner structure. We successfully established a series of spectroscopic and *in silico* simulation techniques to analyse the PEG density of siRNA polyplex micelles instead of conventional calculation using PEG shell thickness and polymer binding number. These two approaches provide a potential alternative method to determine the PEG crowdedness of polyplex micelles with a smaller diameter and non-rigid core, making it difficult to measure the PEG shell thickness under cryo-TEM. We have investigated and demonstrated the effect of CCR on altering the cellular uptake and gene silencing ability of polyplex micelles. We also concluded that even though the polyplex micelles with efficient cell uptake and gene interference, do not show superior benefit in targeting hepatocytes when it comes to *in vivo*. Thus, evaluating the *in vivo* biodistribution profile of gene carriers and their *in vivo* PK/PD is compulsory in developing gene nanocarriers. A series of IVM time lapsing imaging was performed to examine the accumulation behaviour of polyplex micelles in the liver. With the aid of in-house developed algorithm, thousands of confocal microscopy images were analysed. The outcomes confirmed our hypothesis that CCR of the polymer micelles positively impact cell-type-specific uptake, passive targeting of hepatocytes was achieved by high CCR polyplex micelles EN15. They were limited by the field of view of conventional fluorescent microscopy, studying the biodistribution profile over several organs problematic. In this regard, we introduced a new mesoscopy imaging technique in tracking the gene carriers by providing high resolution and detailed anatomical images on every animal organs. By using this

system, the elimination route of the polyplex micelles were visualized and quantified. The result again supported the finding from IVM; high CCR micelles preferably follow the hepatobiliary route, confirming the uptake by hepatocytes.

Our overall finding strongly suggests that purposeful modification of CCR may be applied for targeting specific cells and tissues and may be used to modify properties of the carrier, allowing the formation of a stable and intact PEG-corona. The latter was confirmed to protect the polyplex micelles from nonspecific uptake *in vitro* and *in vivo*, leading to a passive accumulation in hepatocytes while avoiding the local and systemic reticuloendothelial system. Furthermore, this proposed platform for delivering siRNA exhibits excellent versatility as it can adapt and deliver any kind of small oligonucleotide. This work introduced a series of new interventions to investigate nanocarriers, including characterizing the surface properties by Raman spectroscopy, visualizing the structural conformation by DPD simulation, determining the clearance pathway by the mesoscopy imaging technique. This study presented a potential methodology to evaluate all drug/ gene delivery system in the future.

6. References

Abe T, Masuda T, Satodate R. 1988. Phagocytic activity of Kupffer cells in splenectomized rats. Virchows Archiv A, 413 (5):457-462.

Agarwal S, Simon AR, Goel V, Habtemariam BA, Clausen VA, Kim JB, Robbie GJ. 2020. Pharmacokinetics and Pharmacodynamics of the Small Interfering Ribonucleic Acid, Givosiran, in Patients With Acute Hepatic Porphyria. Clinical Pharmacology & Therapeutics, 108 (1):63-72.

Akinc A, Maier MA, Manoharan M, Fitzgerald K, Jayaraman M, Barros S, Ansell S, Du X, Hope MJ, Madden TD, Mui BL, Semple SC, Tam YK, Ciufolini M, Witzigmann D, Kulkarni JA, van der Meel R, Cullis PR. 2019. The Onpattro story and the clinical translation of nanomedicines containing nucleic acid-based drugs. Nature Nanotechnology, 14 (12):1084-1087.

Akkermans RLC, Spenley NA, Robertson SH. 2013. Monte Carlo methods in Materials Studio. Molecular Simulation, 39 (14-15):1153-1164.

Arnida, Janát-Amsbury MM, Ray A, Peterson CM, Ghandehari H. 2011. Geometry and surface characteristics of gold nanoparticles influence their biodistribution and uptake by macrophages. Eur J Pharm Biopharm, 77 (3):417-423.

Asrani SK, Devarbhavi H, Eaton J, Kamath PS. 2019. Burden of liver diseases in the world. Journal of Hepatology, 70 (1):151-171.

Ballermann BJ, Dardik A, Eng E, Liu A. 1998. Shear stress and the endothelium. Kidney International, 54:S100-S108.

Balwani M, Sardh E, Ventura P, Peiró PA, Rees DC, Stölzel U, Bissell DM, Bonkovsky HL, Windyga J, Anderson KE, Parker C, Silver SM, Keel SB, Wang J-D, Stein PE, Harper P, Vassiliou D, Wang B, Phillips J, Ivanova A, Langendonk JG, Kauppinen R, Minder E, Horie Y, Penz C, Chen J, Liu S, Ko JJ, Sweetser MT, Garg P, Vaishnaw A, Kim JB, Simon AR, Gouya L. 2020. Phase 3 Trial of RNAi Therapeutic Givosiran for Acute Intermittent Porphyria. New England Journal of Medicine, 382 (24):2289-2301.

Barthel MJ, Schacher FH, Schubert US. 2014a. Poly(ethylene oxide) (PEO)-based ABC triblock terpolymers – synthetic complexity vs. application benefits. Polymer Chemistry, 5 (8):2647-2662.

Barthel MJ, Babiuch K, Rudolph T, Vitz J, Hoeppener S, Gottschaldt M, Hager MD, Schacher FH, Schubert US. 2012. Bis-hydrophilic and functional triblock terpolymers based on polyethers: Synthesis and self-assembly in solution. Journal of Polymer Science Part A: Polymer Chemistry, 50 (14):2914-2923.

Barthel MJ, Rinkenauer AC, Wagner M, Mansfeld U, Hoeppener S, Czaplewska JA, Gottschaldt M, Träger A, Schacher FH, Schubert US. 2014b. Small but Powerful: Co-Assembly of Polyether-Based Triblock Terpolymers into Sub-30 nm Micelles and Synergistic Effects on Cellular Interactions. Biomacromolecules, 15 (7):2426-2439.

Bauer M, Press AT, Trauner M. 2013. The liver in sepsis: patterns of response and injury. Curr Opin Crit Care, 19 (2):123-127.

Beljaars L, Meijer DK, Poelstra K. 2002. Targeting hepatic stellate cells for cell-specific treatment of liver fibrosis. Front Biosci, 7:e214-222.

Benjamini Y, Hochberg Y. 1995. Controlling the false discovery rate: a practical and powerful approach to multiple testing. Journal of the Royal statistical society: series B (Methodological), 57 (1):289-300.

BIOVIA. 2020. Dassault Systèmes, Materials Studio, 19.1.0.219. San Diego: Dassault Systèmes.

Blanco E, Shen H, Ferrari M. 2015. Principles of nanoparticle design for overcoming biological barriers to drug delivery. Nature Biotechnology, 33 (9):941-951.

Böttger R, Pauli G, Chao P-H, Al Fayez N, Hohenwarter L, Li S-D. 2020. Lipid-based nanoparticle technologies for liver targeting. Advanced Drug Delivery Reviews, 154-155:79-101.

Boyer JL. 2013. Bile formation and secretion. Compr Physiol, 3 (3):1035-1078.

Braet F, Wisse E. 2002. Structural and functional aspects of liver sinusoidal endothelial cell fenestrae: a review. Comparative hepatology, 1 (1):1-17.

Byass P. 2014. The global burden of liver disease: a challenge for methods and for public health. BMC medicine, 12:159-159.

Cabral H, Miyata K, Osada K, Kataoka K. 2018. Block Copolymer Micelles in Nanomedicine Applications. Chem Rev, 118 (14):6844-6892.

Cabral H, Matsumoto Y, Mizuno K, Chen Q, Murakami M, Kimura M, Terada Y, Kano MR, Miyazono K, Uesaka M, Nishiyama N, Kataoka K. 2011. Accumulation of

sub-100 nm polymeric micelles in poorly permeable tumours depends on size. Nature Nanotechnology, 6 (12):815-823.

Carthew RW, Sontheimer EJ. 2009. Origins and Mechanisms of miRNAs and siRNAs. Cell, 136 (4):642-655.

Castiglioni C, Del Zoppo M, Zerbi G. 1993. Vibrational Raman spectroscopy of polyconjugated organic oligomers and polymers. Journal of Raman Spectroscopy, 24 (8):485-494.

Chen D, Ganesh S, Wang W, Amiji M. 2020. Protein Corona-Enabled Systemic Delivery and Targeting of Nanoparticles. The AAPS Journal, 22 (4):83.

Cheng S-H, Li F-C, Souris JS, Yang C-S, Tseng F-G, Lee H-S, Chen C-T, Dong C-Y, Lo L-W. 2012. Visualizing Dynamics of Sub-Hepatic Distribution of Nanoparticles Using Intravital Multiphoton Fluorescence Microscopy. ACS Nano, 6 (5):4122-4131.

Choi CHJ, Zuckerman JE, Webster P, Davis ME. 2011. Targeting kidney mesangium by nanoparticles of defined size. Proceedings of the National Academy of Sciences, 108 (16):6656-6661.

Choi HS, Liu W, Misra P, Tanaka E, Zimmer JP, Ipe BI, Bawendi MG, Frangioni JV. 2007. Renal clearance of nanoparticles. Nature biotechnology, 25 (10):1165.

Cogger VC, O'Reilly JN, Warren A, Le Couteur DG. 2015. A standardized method for the analysis of liver sinusoidal endothelial cells and their fenestrations by scanning electron microscopy. Journal of visualized experiments : JoVE, (98):e52698-e52698.

Cunningham AJ, Gibson VP, Banquy X, Zhu X, Jeanne LC. 2020. Cholic acid-based mixed micelles as siRNA delivery agents for gene therapy. International journal of pharmaceutics, 578:119078.

Danaei M, Dehghankhold M, Ataei S, Hasanzadeh Davarani F, Javanmard R, Dokhani A, Khorasani S, Mozafari M. 2018. Impact of particle size and polydispersity index on the clinical applications of lipidic nanocarrier systems. Pharmaceutics, 10 (2):57.

De Matos LL, Trufelli DC, De Matos MGL, Da Silva Pinhal MA. 2010. Immunohistochemistry as an Important Tool in Biomarkers Detection and Clinical Practice. Biomarker Insights, 5:BMI.S2185.

Dias DR, Moreira AF, Correia IJ. 2016. The effect of the shape of gold core–mesoporous silica shell nanoparticles on the cellular behavior and tumor spheroid penetration. Journal of Materials Chemistry B, 4 (47):7630-7640.

Dirisala A, Osada K, Chen Q, Tockary TA, Machitani K, Osawa S, Liu X, Ishii T, Miyata K, Oba M, Uchida S, Itaka K, Kataoka K. 2014. Optimized rod length of polyplex micelles for maximizing transfection efficiency and their performance in systemic gene therapy against stroma-rich pancreatic tumors. Biomaterials, 35 (20):5359-5368.

Dixon LJ, Barnes M, Tang H, Pritchard MT, Nagy LE. 2013. Kupffer cells in the liver. Comprehensive Physiology, 3 (2):785-797.

Dreher MR, Liu W, Michelich CR, Dewhirst MW, Yuan F, Chilkoti A. 2006. Tumor Vascular Permeability, Accumulation, and Penetration of Macromolecular Drug Carriers. JNCI: Journal of the National Cancer Institute, 98 (5):335-344.

Du B, Yu M, Zheng J. 2018. Transport and interactions of nanoparticles in the kidneys. Nature Reviews Materials, 3 (10):358-374.

Elbashir SM, Harborth J, Lendeckel W, Yalcin A, Weber K, Tuschl T. 2001. Duplexes of 21-nucleotide RNAs mediate RNA interference in cultured mammalian cells. Nature, 411 (6836):494-498.

Fischer HC, Hauck TS, Gómez-Aristizábal A, Chan WCW. 2010. Exploring Primary Liver Macrophages for Studying Quantum Dot Interactions with Biological Systems. Advanced Materials, 22 (23):2520-2524.

Földes-Papp Z, Demel U, Tilz GP. 2003. Laser scanning confocal fluorescence microscopy: an overview. International Immunopharmacology, 3 (13):1715-1729.

Foujdar R, Bera MB, Chopra HK. 2020. Chapter 30 - Phenolic nanoconjugates and its application in food. In: Pal K, Banerjee I, Sarkar P, Kim D, Deng W-P, Dubey NK, Majumder K, Hrsg. Biopolymer-Based Formulations. Elsevier, 751-780.

GBD GBoDCN. 2018. Global Burden of Disease Study 2017 (GBD 2017) Burden by Risk 1990-2017. Seattle, United States: Institute for Health Metrics and Evaluation (IHME).

Gebhardt R. 1992. Metabolic zonation of the liver: Regulation and implications for liver function. Pharmacology & Therapeutics, 53 (3):275-354.

Geng Y, Dalhaimer P, Cai S, Tsai R, Tewari M, Minko T, Discher DE. 2007. Shape effects of filaments versus spherical particles in flow and drug delivery. Nat Nanotechnol, 2 (4):249-255.

Gong B, Chen J-H, Yajima R, Chen Y, Chase E, Chadalavada DM, Golden BL, Carey PR, Bevilacqua PC. 2009. Raman crystallography of RNA. Methods, 49 (2):101-111.

Graves EE, Ripoll J, Weissleder R, Ntziachristos V. 2003. A submillimeter resolution fluorescence molecular imaging system for small animal imaging. Med Phys, 30 (5):901-911.

Guo L, Luo S, Du Z, Zhou M, Li P, Fu Y, Sun X, Huang Y, Zhang Z. 2017. Targeted delivery of celastrol to mesangial cells is effective against mesangioproliferative glomerulonephritis. Nature communications, 8 (1):1-17.

Hao L, Lin L, Zhou J. 2019. pH-Responsive Zwitterionic Copolymer DHA–PBLG–PCB for Targeted Drug Delivery: A Computer Simulation Study. Langmuir, 35 (5):1944-1953.

Hoang QT, Heo T-Y, Choi DG, Choi S-H, Shim MS. 2020. Guanidinium-Incorporated Micelleplexes for Low Toxic and Efficient siRNA Delivery. Macromolecular Research, 28 (12):1160-1165.

Hoogerbrugge PJ, Koelman JMVA. 1992. Simulating Microscopic Hydrodynamic Phenomena with Dissipative Particle Dynamics. Europhysics Letters (EPL), 19 (3):155-160.

Hrubý M, Koňák Č, Ulbrich K. 2005. Polymeric micellar pH-sensitive drug delivery system for doxorubicin. Journal of Controlled Release, 103 (1):137-148.

Hu B, Zhong L, Weng Y, Peng L, Huang Y, Zhao Y, Liang X-J. 2020. Therapeutic siRNA: state of the art. Signal Transduction and Targeted Therapy, 5 (1):101.

Huang X, Li L, Liu T, Hao N, Liu H, Chen D, Tang F. 2011. The Shape Effect of Mesoporous Silica Nanoparticles on Biodistribution, Clearance, and Biocompatibility in Vivo. ACS Nano, 5 (7):5390-5399.

Joseph J, Tomaszewski M, Morgan FJ, Bohndiek SE. 2015. Evaluation of MultiSpectral Optoacoustic Tomography (MSOT) performance in phantoms and in vivo. Photons Plus Ultrasound: Imaging and Sensing 2015, 9323:93230J.

Joshi N, Yan J, Levy S, Bhagchandani S, Slaughter KV, Sherman NE, Amirault J, Wang Y, Riegel L, He X, Rui TS, Valic M, Vemula PK, Miranda OR, Levy O,

Gravallese EM, Aliprantis AO, Ermann J, Karp JM. 2018. Towards an arthritis flare-responsive drug delivery system. Nature Communications, 9 (1):1275.

Judge AD, Sood V, Shaw JR, Fang D, McClintock K, MacLachlan I. 2005. Sequence-dependent stimulation of the mammalian innate immune response by synthetic siRNA. Nature Biotechnology, 23 (4):457-462.

Jungermann K, Kietzmann T. 1996. Zonation of parenchymal and nonparenchymal metabolism in liver. Annu Rev Nutr, 16:179-203.

Kataoka K, Harada A, Nagasaki Y. 2001. Block copolymer micelles for drug delivery: design, characterization and biological significance. Advanced Drug Delivery Reviews, 47 (1):113-131.

Kataoka K, Itaka K, Nishiyama N, Yamasaki Y, Oishi M, Nagasaki Y. 2005. Smart polymeric micelles as nanocarriers for oligonucleotides and siRNA delivery. Nucleic Acids Symposium Series, 49 (1):17-18.

Koo V, Hamilton P, Williamson K. 2006. Non-invasive in vivo imaging in small animal research. Analytical Cellular Pathology, 28 (4):127-139.

Kulkarni SA, Feng S-S. 2013. Effects of Particle Size and Surface Modification on Cellular Uptake and Biodistribution of Polymeric Nanoparticles for Drug Delivery. Pharmaceutical Research, 30 (10):2512-2522.

Kunjachan S, Gremse F, Theek B, Koczera P, Pola R, Pechar M, Etrych T, Ulbrich K, Storm G, Kiessling F, Lammers T. 2013. Noninvasive Optical Imaging of Nanomedicine Biodistribution. ACS Nano, 7 (1):252-262.

Lê S, Josse J, Husson F. 2008. FactoMineR: an R package for multivariate analysis. Journal of statistical software, 25 (1):1-18.

Li S, Chen H, Liu H, Liu L, Yuan Y, Mao C, Zhang W, Zhang X, Guo W, Lee C-S, Liang X-J. 2020. In Vivo Real-Time Pharmaceutical Evaluations of Near-Infrared II Fluorescent Nanomedicine Bound Polyethylene Glycol Ligands for Tumor Photothermal Ablation. ACS Nano, 14 (10):13681-13690.

Livak KJ, Schmittgen TD. 2001. Analysis of relative gene expression data using real-time quantitative PCR and the 2− ΔΔCT method. methods, 25 (4):402-408.

Luo Z, Jiang J. 2012. pH-sensitive drug loading/releasing in amphiphilic copolymer PAE–PEG: Integrating molecular dynamics and dissipative particle dynamics simulations. Journal of Controlled Release, 162 (1):185-193.

Marcellin P, Kutala BK. 2018. Liver diseases: A major, neglected global public health problem requiring urgent actions and large-scale screening. Liver International, 38 (S1):2-6.

Mir M, Ishtiaq S, Rabia S, Khatoon M, Zeb A, Khan GM, ur Rehman A, ud Din F. 2017. Nanotechnology: from In Vivo Imaging System to Controlled Drug Delivery. Nanoscale Research Letters, 12 (1):500.

Mitchell MJ, Billingsley MM, Haley RM, Wechsler ME, Peppas NA, Langer R. 2021. Engineering precision nanoparticles for drug delivery. Nature Reviews Drug Discovery, 20 (2):101-124.

Mitra V, Metcalf J. 2012. Metabolic functions of the liver. Anaesthesia & Intensive Care Medicine, 13 (2):54-55.

Mo YZ, Xu JC. 2014. Studies on Mechanical Properties and Optimization Model of PI/SiO2 Nanocomposite Based on Materials Studio. Advanced Materials Research, 1049-1050:54-57.

Morrison C. 2018. Alnylam prepares to land first RNAi drug approval. Nature Reviews Drug Discovery, 17 (3):156-157.

Morrissey DV, Lockridge JA, Shaw L, Blanchard K, Jensen K, Breen W, Hartsough K, Machemer L, Radka S, Jadhav V, Vaish N, Zinnen S, Vargeese C, Bowman K, Shaffer CS, Jeffs LB, Judge A, MacLachlan I, Polisky B. 2005. Potent and persistent in vivo anti-HBV activity of chemically modified siRNAs. Nat Biotechnol, 23 (8):1002-1007.

Mosqueira VC, Legrand P, Morgat JL, Vert M, Mysiakine E, Gref R, Devissaguet JP, Barratt G. 2001. Biodistribution of long-circulating PEG-grafted nanocapsules in mice: effects of PEG chain length and density. Pharm Res, 18 (10):1411-1419.

Muljajew I, Huschke S, Ramoji A, Cseresnyés Z, Hoeppener S, Nischang I, Foo W, Popp J, Figge MT, Weber C, Bauer M, Schubert US, Press AT. 2021. Stealth Effect of Short Polyoxazolines in Graft Copolymers: Minor Changes of Backbone End Group Determine Liver Cell-Type Specificity. ACS Nano, 15 (7):12298-12313.

Mullard A. 2018. FDA approves landmark RNAi drug. Nature Reviews Drug Discovery, 17 (9):613-613.

Nuhn L, Tomcin S, Miyata K, Mailänder V, Landfester K, Kataoka K, Zentel R. 2014. Size-Dependent Knockdown Potential of siRNA-Loaded Cationic Nanohydrogel Particles. Biomacromolecules, 15 (11):4111-4121.

Ogawara K-I, Yoshida M, Furumoto K, Takakura Y, Hashida M, Higaki K, Kimura T. 1999. Uptake by Hepatocytes and Biliary Excretion of Intravenously Administered Polystyrene Microspheres in Rats. Journal of Drug Targeting, 7 (3):213-221.

Onpattro. 2018. Onpattro assessment report. https://wwwemaeuropaeu/en/documents/assessment-report/onpattro-epar-public-assessment-report_pdf.

Osada K, Oshima H, Kobayashi D, Doi M, Enoki M, Yamasaki Y, Kataoka K. 2010. Quantized Folding of Plasmid DNA Condensed with Block Catiomer into Characteristic Rod Structures Promoting Transgene Efficacy. Journal of the American Chemical Society, 132 (35):12343-12348.

Owens DE, Peppas NA. 2006. Opsonization, biodistribution, and pharmacokinetics of polymeric nanoparticles. International Journal of Pharmaceutics, 307 (1):93-102.

Perry JL, Reuter KG, Kai MP, Herlihy KP, Jones SW, Luft JC, Napier M, Bear JE, DeSimone JM. 2012. PEGylated PRINT Nanoparticles: The Impact of PEG Density on Protein Binding, Macrophage Association, Biodistribution, and Pharmacokinetics. Nano Letters, 12 (10):5304-5310.

Poon W, Zhang Y-N, Ouyang B, Kingston BR, Wu JLY, Wilhelm S, Chan WCW. 2019. Elimination Pathways of Nanoparticles. ACS Nano, 13 (5):5785-5798.

Popielarski SR, Hu-Lieskovan S, French SW, Triche TJ, Davis ME. 2005. A nanoparticle-based model delivery system to guide the rational design of gene delivery to the liver. 2. In vitro and in vivo uptake results. Bioconjug Chem, 16 (5):1071-1080.

Press AT, Butans MJ, Haider TP, Weber C, Neugebauer S, Kiehntopf M, Schubert US, Clemens MG, Bauer M, Kortgen A. 2017a. Fast simultaneous assessment of renal and liver function using polymethine dyes in animal models of chronic and acute organ injury. Sci Rep, 7 (1):15397.

Press AT, Ramoji A, vd Lühe M, Rinkenauer AC, Hoff J, Butans M, Rössel C, Pietsch C, Neugebauer U, Schacher FH, Bauer M. 2017b. Cargo–carrier interactions

significantly contribute to micellar conformation and biodistribution. NPG Asia Materials, 9 (10):e444-e444.

Press AT, Traeger A, Pietsch C, Mosig A, Wagner M, Clemens MG, Jbeily N, Koch N, Gottschaldt M, Bézière N, Ermolayev V, Ntziachristos V, Popp J, Kessels MM, Qualmann B, Schubert US, Bauer M. 2014. Cell type-specific delivery of short interfering RNAs by dye-functionalised theranostic nanoparticles. Nature Communications, 5 (1):5565.

Press AT, Babic P, Hoffmann B, Müller T, Foo W, Hauswald W, Benecke J, Beretta M, Cseresnyés Z, Hoeppener S, Nischang I, Coldewey SM, Gräler MH, Bauer R, Gonnert F, Gaßler N, Wetzker R, Figge MT, Schubert US, Bauer M. 2021. Targeted delivery of a phosphoinositide 3-kinase γ inhibitor to restore organ function in sepsis. EMBO Mol Med, 13 (10):e14436.

Priem B, Tian C, Tang J, Zhao Y, Mulder WJ. 2015. Fluorescent nanoparticles for the accurate detection of drug delivery. Expert Opin Drug Deliv, 12 (12):1881-1894.

Probst CE, Zrazhevskiy P, Bagalkot V, Gao X. 2013. Quantum dots as a platform for nanoparticle drug delivery vehicle design. Advanced Drug Delivery Reviews, 65 (5):703-718.

Rabanel J-M, Hildgen P, Banquy X. 2014. Assessment of PEG on polymeric particles surface, a key step in drug carrier translation. Journal of Controlled Release, 185:71-87.

Rietscher R, Czaplewska JA, Majdanski TC, Gottschaldt M, Schubert US, Schneider M, Lehr C-M. 2016. Impact of PEG and PEG-b-PAGE modified PLGA on nanoparticle formation, protein loading and release. International Journal of Pharmaceutics, 500 (1):187-195.

Rinkenauer AC, Press AT, Raasch M, Pietsch C, Schweizer S, Schwörer S, Rudolph KL, Mosig A, Bauer M, Traeger A, Schubert US. 2015. Comparison of the uptake of methacrylate-based nanoparticles in static and dynamic in vitro systems as well as in vivo. J Control Release, 216:158-168.

Roberts M. 2020. Covid-19: Pfizer/BioNTech vaccine judged safe for use in UK.

Rossiter D. 2012. Introduction to the R Project for Statistical Computing for use at ITC. International Institute for Geo-information Science & Earth Observation (ITC), Enschede (NL), 3:3-6.

Ruiz-Morales Y, Romero-Martínez A. 2018. Coarse-Grain Molecular Dynamics Simulations To Investigate the Bulk Viscosity and Critical Micelle Concentration of the Ionic Surfactant Sodium Dodecyl Sulfate (SDS) in Aqueous Solution. The Journal of Physical Chemistry B, 122 (14):3931-3943.

Ryan CG, Clayton E, Griffin WL, Sie SH, Cousens DR. 1988. SNIP, a statistics-sensitive background treatment for the quantitative analysis of PIXE spectra in geoscience applications. Nuclear Instruments and Methods in Physics Research Section B: Beam Interactions with Materials and Atoms, 34 (3):396-402.

Sadauskas E, Wallin H, Stoltenberg M, Vogel U, Doering P, Larsen A, Danscher G. 2007. Kupffer cells are central in the removal of nanoparticles from the organism. Particle and fibre toxicology, 4:10-10.

Sato Y, Murase K, Kato J, Kobune M, Sato T, Kawano Y, Takimoto R, Takada K, Miyanishi K, Matsunaga T, Takayama T, Niitsu Y. 2008. Resolution of liver cirrhosis using vitamin A-coupled liposomes to deliver siRNA against a collagen-specific chaperone. Nat Biotechnol, 26 (4):431-442.

Scott LJ. 2020. Givosiran: first approval. Drugs, 80 (3):335-339.

Scott LJ, Keam SJ. 2021. Lumasiran: First Approval. Drugs, 81 (2):277-282.

Sehgal A, Vaishnaw A, Fitzgerald K. 2013. Liver as a target for oligonucleotide therapeutics. Journal of hepatology, 59 (6):1354-1359.

Sepanlou SG, Safiri S, Bisignano C, Ikuta KS, Merat S, Saberifiroozi M, Poustchi H, Tsoi D, Colombara DV, Abdoli A, Adedoyin RA, Afarideh M, Agrawal S, Ahmad S, Ahmadian E, Ahmadpour E, Akinyemiju T, Akunna CJ, Alipour V, Almasi-Hashiani A, Almulhim AM, Al-Raddadi RM, Alvis-Guzman N, Anber NH, Angus C, Anoushiravani A, Arabloo J, Araya EM, Asmelash D, Ataeinia B, Ataro Z, Atout MMdW, Ausloos F, Awasthi A, Badawi A, Banach M, Bejarano Ramirez DF, Bhagavathula AS, Bhala N, Bhattacharyya K, Biondi A, Bolla SR, Boloor A, Borzì AM, Butt ZA, Cámera LLAA, Campos-Nonato IR, Carvalho F, Chu D-T, Chung S-C, Cortesi PA, Costa VM, Cowie BC, Daryani A, de Courten B, Demoz GT, Desai R, Dharmaratne SD, Djalalinia S, Do HT, Dorostkar F, Drake TM, Dubey M, Duncan BB, Effiong A, Eftekhari A, Elsharkawy A, Etemadi A, Farahmand M, Farzadfar F, Fernandes E, Filip I, Fischer F, Gebremedhin KBB, Geta B, Gilani SA, Gill PS, Gutirrez RA, Haile MT, Haj-Mirzaian A, Hamid SS,

Hasankhani M, Hasanzadeh A, Hashemian M, Hassen HY, Hay SI, Hayat K, Heidari B, Henok A, Hoang CL, Hostiuc M, Hostiuc S, Hsieh VC-r, Igumbor EU, Ilesanmi OS, Irvani SSN, Jafari Balalami N, James SL, Jeemon P, Jha RP, Jonas JB, Jozwiak JJ, Kabir A, Kasaeian A, Kassaye HG, Kefale AT, Khalilov R, Khan MA, Khan EA, Khater A, Kim YJ, Koyanagi A, La Vecchia C, Lim L-L, Lopez AD, Lorkowski S, Lotufo PA, Lozano R, Magdy Abd El Razek M, Mai HT, Manafi N, Manafi A, Mansournia MA, Mantovani LG, Mazzaglia G, Mehta D, Mendoza W, Menezes RG, Mengesha MM, Meretoja TJ, Mestrovic T, Miazgowski B, Miller TR, Mirrakhimov EM, Mithra P, Moazen B, Moghadaszadeh M, Mohammadian-Hafshejani A, Mohammed S, Mokdad AH, Montero-Zamora PA, Moradi G, Naimzada MD, Nayak V, Negoi I, Nguyen TH, Ofori-Asenso R, Oh I-H, Olagunju TO, Padubidri JR, Pakshir K, Pana A, Pathak M, Pourshams A, Rabiee N, Radfar A, Rafiei A, Ramezanzadeh K, Rana SMM, Rawaf S, Rawaf DL, Reiner RC, Jr., Roever L, Room R, Roshandel G, Safari S, Samy AM, Sanabria J, Sartorius B, Schmidt MI, Senthilkumaran S, Shaikh MA, Sharif M, Sharifi A, Shigematsu M, Singh JA, Soheili A, Suleria HAR, Teklehaimanot BF, Tesfay BE, Vacante M, Vahedian-Azimi A, Valdez PR, Vasankari TJ, Vu GT, Waheed Y, Weldegwergs KG, Werdecker A, Westerman R, Wondafrash DZ, Wondmieneh AB, Yeshitila YG, Yonemoto N, Yu C, Zaidi Z, Zarghi A, Zelber-Sagi S, Zewdie KA, Zhang Z-J, Zhao X-J, Naghavi M, Malekzadeh R. 2020. The global, regional, and national burden of cirrhosis by cause in 195 countries and territories, 1990–2017: a systematic analysis for the Global Burden of Disease Study 2017. The Lancet Gastroenterology & Hepatology, 5 (3):245-266.

Simões S, Filipe A, Faneca H, Mano M, Penacho N, Düzgünes N, Pedroso de Lima M. 2005. Cationic liposomes for gene delivery. Expert Opinion on Drug Delivery, 2 (2):237-254.

Souris JS, Lee CH, Cheng SH, Chen CT, Yang CS, Ho JA, Mou CY, Lo LW. 2010. Surface charge-mediated rapid hepatobiliary excretion of mesoporous silica nanoparticles. Biomaterials, 31 (21):5564-5574.

Sun H, Jin Z, Yang C, Akkermans RL, Robertson SH, Spenley NA, Miller S, Todd SM. 2016. COMPASS II: extended coverage for polymer and drug-like molecule databases. J Mol Model, 22 (2):47.

Takeda KM, Osada K, Tockary TA, Dirisala A, Chen Q, Kataoka K. 2017a. Poly(ethylene glycol) Crowding as Critical Factor To Determine pDNA Packaging Scheme into Polyplex Micelles for Enhanced Gene Expression. Biomacromolecules, 18 (1):36-43.

Takeda KM, Yamasaki Y, Dirisala A, Ikeda S, Tockary TA, Toh K, Osada K, Kataoka K. 2017b. Effect of shear stress on structure and function of polyplex micelles from poly(ethylene glycol)-poly(l-lysine) block copolymers as systemic gene delivery carrier. Biomaterials, 126:31-38.

Tangsangasaksri M, Takemoto H, Naito M, Maeda Y, Sueyoshi D, Kim HJ, Miura Y, Ahn J, Azuma R, Nishiyama N, Miyata K, Kataoka K. 2016. siRNA-Loaded Polyion Complex Micelle Decorated with Charge-Conversional Polymer Tuned to Undergo Stepwise Response to Intra-Tumoral and Intra-Endosomal pHs for Exerting Enhanced RNAi Efficacy. Biomacromolecules, 17 (1):246-255.

Team RC. 2013. R: A language and environment for statistical computing.

Terreno E, Uggeri F, Aime S. 2012. Image guided therapy: The advent of theranostic agents. Journal of Controlled Release, 161 (2):328-337.

Tockary TA, Osada K, Motoda Y, Hiki S, Chen Q, Takeda KM, Dirisala A, Osawa S, Kataoka K. 2016. Micelles: Rod-to-Globule Transition of pDNA/PEG–Poly(l-Lysine) Polyplex Micelles Induced by a Collapsed Balance Between DNA Rigidity and PEG Crowdedness (Small 9/2016). Small, 12 (9):1244-1244.

Tockary TA, Foo W, Dirisala A, Chen Q, Uchida S, Osawa S, Mochida Y, Liu X, Kinoh H, Cabral H, Osada K, Kataoka K. 2019. Single-Stranded DNA-Packaged Polyplex Micelle as Adeno-Associated-Virus-Inspired Compact Vector to Systemically Target Stroma-Rich Pancreatic Cancer. ACS Nano, 2019.

Tockary TA, Osada K, Chen Q, Machitani K, Dirisala A, Uchida S, Nomoto T, Toh K, Matsumoto Y, Itaka K, Nitta K, Nagayama K, Kataoka K. 2013. Tethered PEG Crowdedness Determining Shape and Blood Circulation Profile of Polyplex Micelle Gene Carriers. Macromolecules, 46 (16):6585-6592.

Trefts E, Gannon M, Wasserman DH. 2017. The liver. Curr Biol, 27 (21):R1147-r1151.

Tsochatzis EA, Bosch J, Burroughs AK. 2014. Liver cirrhosis. The Lancet, 383 (9930):1749-1761.

Walkey CD, Olsen JB, Guo H, Emili A, Chan WC. 2012. Nanoparticle size and surface chemistry determine serum protein adsorption and macrophage uptake. J Am Chem Soc, 134 (4):2139-2147.

Wang H, Thorling CA, Liang X, Bridle KR, Grice JE, Zhu Y, Crawford DH, Xu ZP, Liu X, Roberts MS. 2015. Diagnostic imaging and therapeutic application of nanoparticles targeting the liver. Journal of Materials Chemistry B, 3 (6):939-958.

Wang R, Hu X, Yue J, Zhang W, Cai L, Xie Z, Huang Y, Jing X. 2013. Luteinizing-hormone-releasing-hormone-containing biodegradable polymer micelles for enhanced intracellular drug delivery. Journal of Materials Chemistry B, 1 (3):293-301.

Wang W, Gaus K, Tilley RD, Gooding JJ. 2019a. The impact of nanoparticle shape on cellular internalisation and transport: what do the different analysis methods tell us? Materials Horizons, 6 (8):1538-1547.

Wang X, Xia Y. 2016. microRNA-328 inhibits cervical cancer cell proliferation and tumorigenesis by targeting TCF7L2. Biochemical and Biophysical Research Communications, 475 (2):169-175.

Wang Y, Wang Z, Xu C, Tian H, Chen X. 2019b. A disassembling strategy overcomes the EPR effect and renal clearance dilemma of the multifunctional theranostic nanoparticles for cancer therapy. Biomaterials, 197:284-293.

Wanless IR, Wong F, Blendis LM, Greig P, Heathcote EJ, Levy G. 1995. Hepatic and portal vein thrombosis in cirrhosis: possible role in development of parenchymal extinction and portal hypertension. Hepatology, 21 (5):1238-1247.

Whitehead KA, Langer R, Anderson DG. 2009. Knocking down barriers: advances in siRNA delivery. Nature Reviews Drug Discovery, 8 (2):129-138.

Whitemore M, Li S, Huang L. 1999. Liposome Vectors for In Vivo Gene Delivery. Current Protocols in Human Genetics, 20 (1):12.18.11-12.18.19.

Wickham H. 2011. ggplot2. Wiley Interdisciplinary Reviews: Computational Statistics, 3 (2):180-185.

Wisse E, Jacobs F, Topal B, Frederik P, De Geest B. 2008. The size of endothelial fenestrae in human liver sinusoids: implications for hepatocyte-directed gene transfer. Gene therapy, 15 (17):1193-1199.

Wolf PL. 1999. Biochemical diagnosis of liver disease. Indian Journal of Clinical Biochemistry, 14 (1):59-90.

Wu J, Sun TM, Yang XZ, Zhu J, Du XJ, Yao YD, Xiong MH, Wang HX, Wang YC, Wang J. 2013. Enhanced drug delivery to hepatocellular carcinoma with a galactosylated core-shell polyphosphoester nanogel. Biomater Sci, 1 (11):1143-1150.

Xie X, Liao J, Shao X, Li Q, Lin Y. 2017. The Effect of shape on Cellular Uptake of Gold Nanoparticles in the forms of Stars, Rods, and Triangles. Scientific Reports, 7 (1):3827.

Yin D, Wen H, Wu G, Li S, Liu C, Lu H, Liang D. 2020. PEGylated gene carriers in serum under shear flow. Soft Matter, 16 (9):2301-2310.

Yin H, Kanasty RL, Eltoukhy AA, Vegas AJ, Dorkin JR, Anderson DG. 2014. Non-viral vectors for gene-based therapy. Nature Reviews Genetics, 15 (8):541-555.

Zhang MM, Bahal R, Rasmussen TP, Manautou JE, Zhong X-b. 2021. The growth of siRNA-based therapeutics: Updated clinical studies. Biochemical Pharmacology, 189:114432.

Zhang Y, Lundberg P, Diether M, Porsch C, Janson C, Lynd NA, Ducani C, Malkoch M, Malmström E, Hawker CJ, Nyström AM. 2015. Histamine-functionalized copolymer micelles as a drug delivery system in 2D and 3D models of breast cancer. Journal of Materials Chemistry B, 3 (12):2472-2486.

Zhang YN, Poon W, Tavares AJ, McGilvray ID, Chan WCW. 2016. Nanoparticle-liver interactions: Cellular uptake and hepatobiliary elimination. Journal of Controlled Release, 240:332-348.

Zhou C, Tan D, Chen L, Xu X, Sun C, Zong L, Han S, Zhang Y. 2017. Effect of miR-212 targeting TCF7L2 on the proliferation and metastasis of cervical cancer. Eur Rev Med Pharmacol Sci, 21 (2):219-226.

Zuckerman JE, Davis ME. 2013. Targeting therapeutics to the glomerulus with nanoparticles. Advances in chronic kidney disease, 20 (6):500-507.

Zuckerman JE, Choi CHJ, Han H, Davis ME. 2012. Polycation-siRNA nanoparticles can disassemble at the kidney glomerular basement membrane. Proceedings of the National Academy of Sciences, 109 (8):3137.

7. Appendix

7.1 Supplementary Tables and Figures

Table A1. The number of duplicates performed in every characterization, *in vitro* and *in vivo* experiment.

Figure	Sample group	Biological replicates	Note
3.3	EN14	8	For each N/P ratio, replicates for each sample group are 8.
	EN15	8	
	EN60	8	
	EN76	8	
3.4	EN14	3	3 measurements for each sample group. Each measurement result was averaged by 20 runs.
	EN15	3	
	EN60	3	
	EN76	3	
3.5 & 3.6	EN14_Poly	13	Each replicate represent a single spectra
	EN15_Poly	11	
	EN60_Poly	7	
	EN76_Poly	16	
	siRNA	6	
	EN14	13	
	EN15	29	
	EN60	10	
	EN76	17	
3.8	Control	15	Each replicate represent a single incubated wells from at least 3 different experiments
	EN14	6	
	EN15	8	
	EN60	6	
	EN76	8	
	Lipo	8	
3.9	Lipo_1h, Lipo_4h	4 each	Individually incubated wells had been considered as replicates from at least 3 different evaluations
	Lipo_12h	5	
	Lipo_24h	3	
	EN14_1h, EN14_12h	5 each	
	EN14_4h	4	
	EN14_24h	3	
	EN15_1h, EN15_4h, EN15_12h	5 each	
	EN15_24h	3	
	EN60_1h, EN60_12h	5 each	
	EN60_4h	4	
	EN60_24h	3	
	EN76_1h, EN76_24h	4 each	
	EN76_4h	5	

	EN76_12h	6	
3.10	control_12	17	Each replicate represent a single incubated wells from at least 5 different experiments
	control_24	37	
	control_48	25	
	EN14_12	14	
	EN14_24	34	
	EN14_48	18	
	EN15_12	5	
	EN15_24	14	
	EN15_48	12	
	EN60_12	5	
	EN60_24	7	
	EN60_48	8	
	EN76_12	5	
	EN76_24	12	
	EN76_48	12	
	Lipo_12	5	
	Lipo_24	18	
	Lipo_48	11	
3.11 & 3.12 & 3.13	EN14	35	Experiments were done on 5 different mice for each sample. For each mouse, 5 to 7 different areas in the liver were analyzed. Since the perfusion and anatomical locations may vary, we consider each position as a replicate.
	EN15	29	
	EN16	29	
	EN76	31	

Figure 3.16

Organs	Sample group	Replicates	Note
Liver	control	150	Experiments were done on 3 different mice for each sample. Each replicate represents each individual ROI one drawn on the fluoresecent images.
	EN15_15min	150	
	EN15_45min	145	
	EN76_15min	150	
	EN76_45min	144	
Gall bladder	control	94	
	EN15_15min	110	
	EN15_45min	73	
	EN76_15min	100	
	EN76_45min	77	
Intestines	control	142	
	EN15_15min	140	
	EN15_45min	120	
	EN76_15min	150	
	EN76_45min	120	

Kidney	control	145
	EN15_15min	172
	EN15_45min	156
	EN76_15min	149
	EN76_45min	130
Bladder	control	96
	EN15_15min	110
	EN15_45min	104
	EN76_15min	130
	EN76_45min	55
Spleen	control	136
	EN15_15min	105
	EN15_45min	130
	EN76_15min	106
	EN76_45min	71
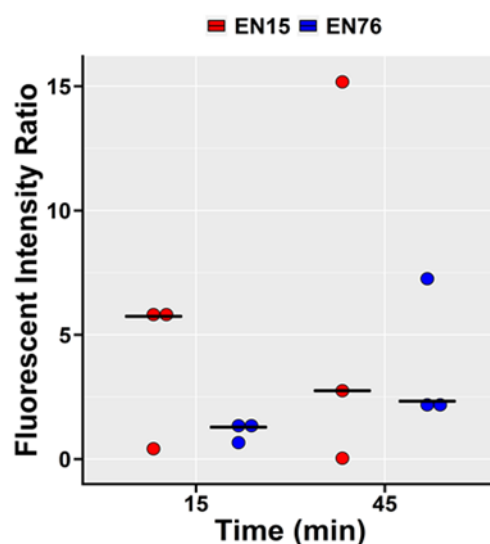
Figure A1. Cy5 fluorescence intensity analysis of liver and kidney involved in the sequestering and excretion of nanocarriers. Graph represented the fluorescence intensity ratio of liver to the kidney for both micelles EN15 and EN76 at time points of 15 min and 45 min.
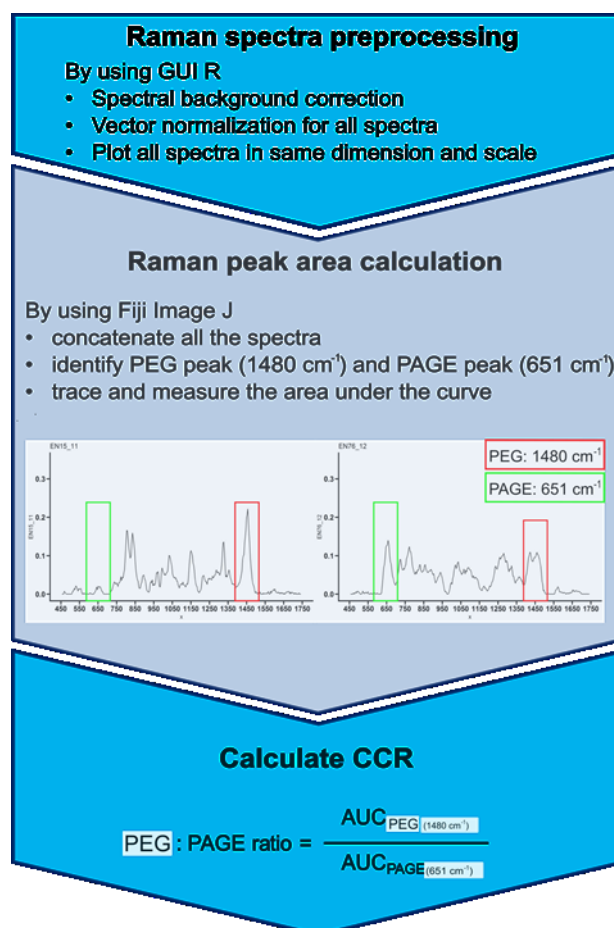
Figure A2. Flowchart represents the preprocessing of all Raman spectra and peak area calculation for Raman vibration peak of PEG and PAGE. The procedure on calculating the CCR ratio of the polyplex micelles.

7.2   Dissipative Particle Dynamic (DPD) Simulation

<u>Programs</u>

All simulations were performed with the program Materials Studio 2020 (MS) and its modules.[1] The Visualizer and Amorphous Cell modules[2] were applied to construct atomistic models, and the Forcite module[3] was used to optimize the structures. All the above steps were performed with COMPASSII force field.[4] The Mesocite module was used for DPD simulations.[5]

<u>Repulsive parameters for DPD calculations</u>

DPD simulations employ coarse-grained models with beads. The most critical parameter is the repulsive parameter α_{ij} between the beads i and j[6]

$$\alpha_{ij} = \alpha_{ii} + 3.27\chi_{ij}\,, \qquad\qquad (1)$$

where α_{ii} is equal to 78 [7] and χ_{ij} is the Flory Huggins parameter.[8] For binary components i and j, the Flory–Huggins parameter χ_{ij} can be estimated by the following equation

$$\chi_{ij} = \frac{V_{bead}}{\kappa_B T}\left(\delta_i - \delta_j\right)^2\,, \qquad\qquad (2)$$

where δ_i and δ_j are the Hildebrand solubility parameters of the components i and j, respectively, and V_{bead} is the volume of a bead (all beads have the same average volume).

In this work, Hildebrand solubility parameters δ were calculated employing atomistic molecular dynamics (MD) simulations. For this, atomistic models of PEG, PAGE, different components of siRNA (four different bases, ribose and phosphoric acid) and water were constructed according to coarse-grained models (see Table A2). Hydrogen atoms were added to saturate dangling bonds. The Hildebrand solubility parameters δ were calculated as listed in Table A2. The repulsive parameters α_{ij} were calculated with equations 1 and 2 (see Table A3).

Coarse-grained models and parameters

The systems simulated in this work were composed of siRNA, PEG$_{42}$-*b*-PAGE$_{n,NH2}$ block copolymer and water. Coarse-grained models of all species involved in these systems are shown in Figure A3. Every two PEG repeat units were coarse-grained into one bead (denoted as E), one PAGE$_{NH2}$ repeat unit was comprised of two beads N and S (one S bead carried a negative charge). The siRNA molecule was coarse-grained into six different types of beads (denoted as A, B, C, G, P, and U), in which A, U, G, and C represented the four different bases of siRNA, B and P represented the ribose and phosphoric acid. The bead of water W contained three water molecules. Based on the Flory-Huggins theory, all beads were assumed to have the same volume. The average volume, mass and radius of each bead was set to 177 Å^3, 113 amu and 3.5 Å, respectively.
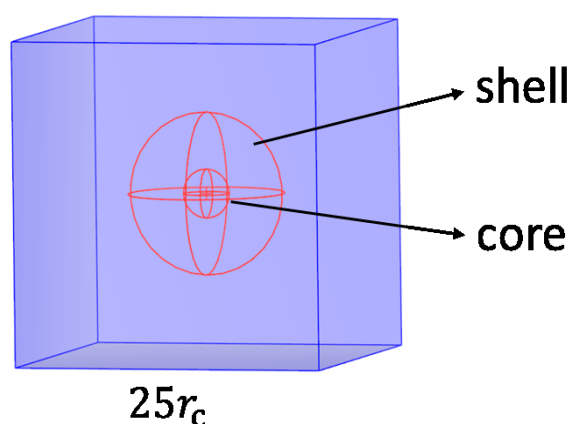
Figure A3. Schematic representation of mesostructured template for DPD simulation.

The length and time scale of DPD simulations in current work, r_c and t_c, were set to 8.1 Å and 0.0047 ns as 1 time step. Cubic simulation cells in the size of 25×25×25 r_c^3 were built. Spring constant was determined as 4.0 and dissipative force parameters as 4.5 for all models using reduced units. In the current work, one cell contained only one micelle with one siRNA molecule. The siRNA molecule was placed in the cell as the core, and block copolymer molecules formed a shell with a radius from 15 to 70 Å. The rest of the space in the cell was filled with water. All cells were simulated for 20000 time steps. The beads-based summation method was applied for electrostatic interactions of beads.

Details of DPD calculations

The evolution of the positions and impulses of all interacting beads over time complies with Newton's second law[9]

$$\frac{dr_i}{dt} = v_i, \ m_i \frac{dv_i}{dt} = F_i \tag{1}$$

where r_i, v_i, and m_i denote the position vector, velocity, and mass of bead i, respectively. F_i represents the total force acting on bead i. For simplicity, the masses of all beads are set to 1 DPD unit.[10] The total force exerting on bead i includes three non-bonded parts from its neighbors: a conservative force F_{ij}^C, a dissipative force F_{ij}^D, and a random force F_{ij}^R. Thus, the total force F_i acting on bead i is described as:

$$F_i = \sum_{j \neq i}\left(F_{ij}^C + F_{ij}^D + F_{ij}^R\right). \tag{2}$$

All forces are short-range with a fixed cutoff radius r_c, which is set to 1 as the length scale of the system. The following formulas give the different parts of the forces:

$$F_{ij}^C = \begin{bmatrix} a_{ij}(1 - r_{ij})\hat{r}_{ij} & (r_{ij} \leq 1) \\ 0 & (r_{ij} \geq 1) \end{bmatrix}, \tag{3}$$

$$F_{ij}^D = \left[-\gamma\omega^D(r_{ij})(v_{ij}\hat{r}_{ij})(\hat{r}_{ij})\right], \tag{4}$$

$$F_{ij}^R = \left[\sigma\omega^R(r_{ij})\xi_{ij}\hat{r}_{ij}\right], \tag{5}$$

where $r_{ij} = \left|\vec{r}_i - \vec{r}_j\right|$, $\hat{r} = \vec{r}_{ij}/r_{ij}$, r_i and r_j are the positions of bead i and bead j, $v_{ij} = \left|\vec{v}_i - \vec{v}_j\right|$, where v_i and v_j are the velocities of bead i and bead j, respectively. a_{ij} is a constant which describes the maximum repulsive force between the interacting beads. ξ_{ij} denotes a randomly fluctuating variable with zero mean and unit variance; γ and σ represent the dissipation and noise strengths, $\omega^D(r_{ij})$ and $\omega^R(r_{ij})$ are weight functions of F_{ij}^D and F_{ij}^R forces, respectively.[9]

$$\sigma = \sqrt{2\gamma\kappa_B T} \qquad (6)$$

$$\omega^D(r_{ij}) = 1 - \frac{r_{ij}}{r_c} \qquad (7)$$

$$\omega^D(r_{ij}) = \left[\omega^R(r_{ij})\right]^2 = (1 - \frac{r_{ij}}{r_c})^2 \quad (8)$$

where T is the system temperature and κ_B is the Boltzmann constant. In DPD simulations, $\kappa_B T = 1$ as the reduced unit of energy. Moreover, a spring force F_i^S is introduced to describe the constraint between the bonded particles in molecules. For example, the spring force acting on the beads of a chain is given by:

$$F_i^S = \sum_j C r_{ij}, \qquad (9)$$

where C is the spring constant, and the sum runs over all particles to which particle i is connected. C is set to 4.0 in current work according to the study by Groot and Warren.[9]

The repulsive parameter α_{ij} between bead i and j lies on the underlying atomistic interactions which is linearly related to the Flory-Huggins parameters as given by the following formula [6]
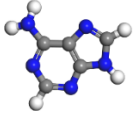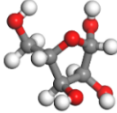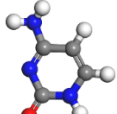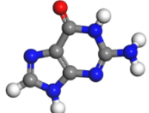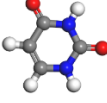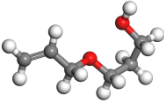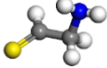
$$\alpha_{ij} = \alpha_{ii} + 3.27\chi_{ij}, \qquad (10)$$

where α_{ii} is equal to 78.[7] For binary components i and j, the Flory–Huggins parameter χ_{ij} can be estimated as

$$\chi_{ij} = \frac{V_{bead}}{\kappa_B T}\left(\delta_i - \delta_j\right)^2, \qquad (11)$$

where δ_i and δ_j are the Hildebrand solubility parameters of components i and j, respectively, and V_{bead} is the volume of a bead (all beads having the same average volume).

Table A2. Atomistic structures and Hildebrand solubility parameters *δ* of DPD beads.

Beads	Atomistic structure	$\delta\ (\sqrt{MPa})$
A		30.1
B		32.8
C		41.0
G		40.3
P		43.6
U		34.6
N		22.4
E		20.7[a]
W		47.8[a]
S		19.4

○H ●C ●N ●O ●S ●P

a) Parameters from ref. 11

Table A3. Interaction parameters α_{ij} between different DPD beads.

	A	B	C	G	P	U	N	E	S	W
A	78.00									
B	79.05[a]	78.00								
C	94.67[a]	87.36[a]	78.00							
G	92.75[a]	85.94[a]	78.06[a]	78.00						
P	103.57[a]	94.28[a]	78.95[a]	79.48[a]	78.00					
U	80.90[a]	78.46[a]	83.67[a]	82.57[a]	89.26[a]	78.00				
N	88.48	96.15	131.59	128.10	146.81	102.40	78.00			
E	90.40	98.65	135.82	132.20	151.59	105.28	78.08	78.00		
S	94.15	103.41	143.62	139.76	160.36	110.72	78.61	78.25	78.00	
W	122.16	109.61	84.57	85.87	80.52	102.44	175.68[a]	78.98	191.71	78.00

a) Parameters taken from ref. 11

References

1. BIOVIA, Dassault Systèmes, Materials Studio, 19.1.0.219, San Diego: Dassault Systèmes, 2020.

2. Akkermans, R. L. C.; Spenley, N. A.; Robertson, S. H., Monte Carlo methods in Materials Studio. *Mol Simulat* **2013,** *39* (14-15), 1153-1164.

3. Mo, Y. Z.; Xu, J. C., Studies on Mechanical Properties and Optimization Model of PI/SiO2 Nanocomposite Based on Materials Studio. *Adv Mater Res-Switz* **2014,** *1049*, 54-57.

4. Sun, H.; Jin, Z.; Yang, C. W.; Akkermans, R. L. C.; Robertson, S. H.; Spenley, N. A.; Miller, S.; Todd, S. M., COMPASS II: extended coverage for polymer and drug-like molecule databases. *J Mol Model* **2016,** *22* (2).

5. Ruiz-Morales, Y.; Romero-Martinez, A., Coarse-Grain Molecular Dynamics Simulations To Investigate the Bulk Viscosity and Critical Micelle Concentration of the Ionic Surfactant Sodium Dodecyl Sulfate (SDS) in Aqueous Solution. *J Phys Chem B* **2018,** *122* (14), 3931-3943.

6. Li, Y. M.; Guo, Y. Y.; Bao, M. T.; Gao, X. L., Investigation of interfacial and structural properties of CTAB at the oil/water interface using dissipative particle dynamics simulations. *J Colloid Interf Sci* **2011,** *361* (2), 573-580.

7. Nie, S. Y.; Zhang, X. F.; Gref, R.; Couvreur, P.; Qian, Y.; Zhang, L. J., Multilamellar Nanoparticles Self-Assembled from Opposite Charged Blends: Insights from Mesoscopic Simulation. *J Phys Chem C* **2015,** *119* (35), 20649-20661.

8. Mark, J. E., *Physical properties of polymers handbook*. 2nd ed.; Springer: New York, 2006; p xix, 1076 p.

9. Groot, R. D.; Warren, P. B., Dissipative particle dynamics: Bridging the gap between atomistic and mesoscopic simulation. *J Chem Phys* **1997,** *107* (11), 4423-4435.

10. Groot, R. D.; Madden, T. J., Dynamic simulation of diblock copolymer microphase separation. *J Chem Phys* **1998,** *108* (20), 8713-8724.

11. Xie, X. N.; Xu, S. P.; Pi, P. H.; Cheng, J.; Wen, X. F.; Liu, X.; Wang, S. N., Dissipative Particle Dynamic Simulation on the Assembly and Release of siRNA/Polymer/Gold Nanoparticles Based Polyplex. *Aiche J* **2018,** *64* (3), 810-821.

7.3   Quantitative automated image analysis

Confocal images of time series recordings and endpoint snapshots were evaluated in Fiji built on ImageJ 1.52s to ImageJ 1.53c.[1, 2] A custom-written ImageJ macro based on the ACAQ platform[3] was applied to carry out the automated image analysis tasks. The time series confocal images were utilized at two wavelengths: the autofluorescence channel, resulted in mainly by NAD(P)H fluorescence, and the Cy3 channel, depicting the location of the Cy3-siRNA polyplex micelles. The former indicated the hepatocytes' location and the sinusoids; the latter characterised the accumulation of the Cy3-siRNA polyplex micelles.

For the time series analysis, the autofluorescence images were utilized to determine the localization of the hepatocytes, the canaliculi, and the sinusoids. On the other hand, the liver-resident macrophages were identified directly from the Cy3 images. The step-by-step segmentation process for all four object types is depicted in Figure A4. The regions of interest (ROI) corresponding to these four objects were stored in memory and used to calculate the mean Cy3 fluorescence intensity within these ROIs, thus describing the kinetic behaviour of the hepatocytes, canaliculi, sinusoids and the Kupffer cells in terms of their Cy3-siRNA polyplex uptake and release.

The image analysis started with identifying the area occupied by the hepatocytes and the canaliculi. First, the autofluorescence images were pre-processed: the random noise was removed with a median filter and the images were normalized by dividing them by the per-image maximum intensity value. The images were then auto-thresholded, filtered and eroded with a morphological filter using a disk element (Figure A4). This outlined the general area occupied by the hepatocytes and the canaliculi (Figure A5). The latter were approximated by calculating the skeleton structure of the foreground area, whereas a refined approximation of the hepatocytes was provided by subtracting the canaliculi area from the first approximation of the hepatocyte's region. Next, the sinusoids were identified with a process similar to the hepatocytes plus canaliculi region, but thresholding for the darker areas as foreground. The erosion step that followed for the sinusoids segmentation was more pronounced than for the other compartments (see figure legends of Figure A4 for more details), to avoid including any non-vessel pixels in the analysis of the plasma level kinetics of the

cargo distribution. Finally, the Kupffer cells were segmented from the Cy3 fluorescence channel after the same pre-processing steps as before, completed with morphological filtering that identified the Kupffer cells based on their shape, size and specific localization inside and near the sinusoids.

In addition to the mean fluorescence intensity of the regions corresponding to the hepatocytes, canaliculi, sinusoids and Kupffer cells, the number of segmented objects was also calculated for the autofluorescence-based analysis of the sinusoids, hepatocytes, and canaliculi to characterise the stability of the segmentation method. The number of segmented objects was important to establish because the confocal microscopy technique only detected the fluorescence signal from a limited depth of field (approximately one micrometre). Thus the drifting or shifting of the detection plane due to organ movement could have moved the sinusoids, hepatocytes, and canaliculi in- and out-of-focus. However, based on our data, the vast majority of the ROI curves were flat, indicating stable experimental conditions.

The time series analysis was carried out on a per micelle-type basis, using the workflow in Figure A4, with representative results shown in Figure A5 for hepatocytes, canaliculi, sinusoids and Kupffer cells. Because the Kupffer cells could only be identified from the Cy3 fluorescence channel, tracking the individual cells over time was not possible. Instead, the population average was calculated for each image of the time series; Figure A5 shows the result of the maximum intensity projection of the identified Kupffer cells for a representative dataset.
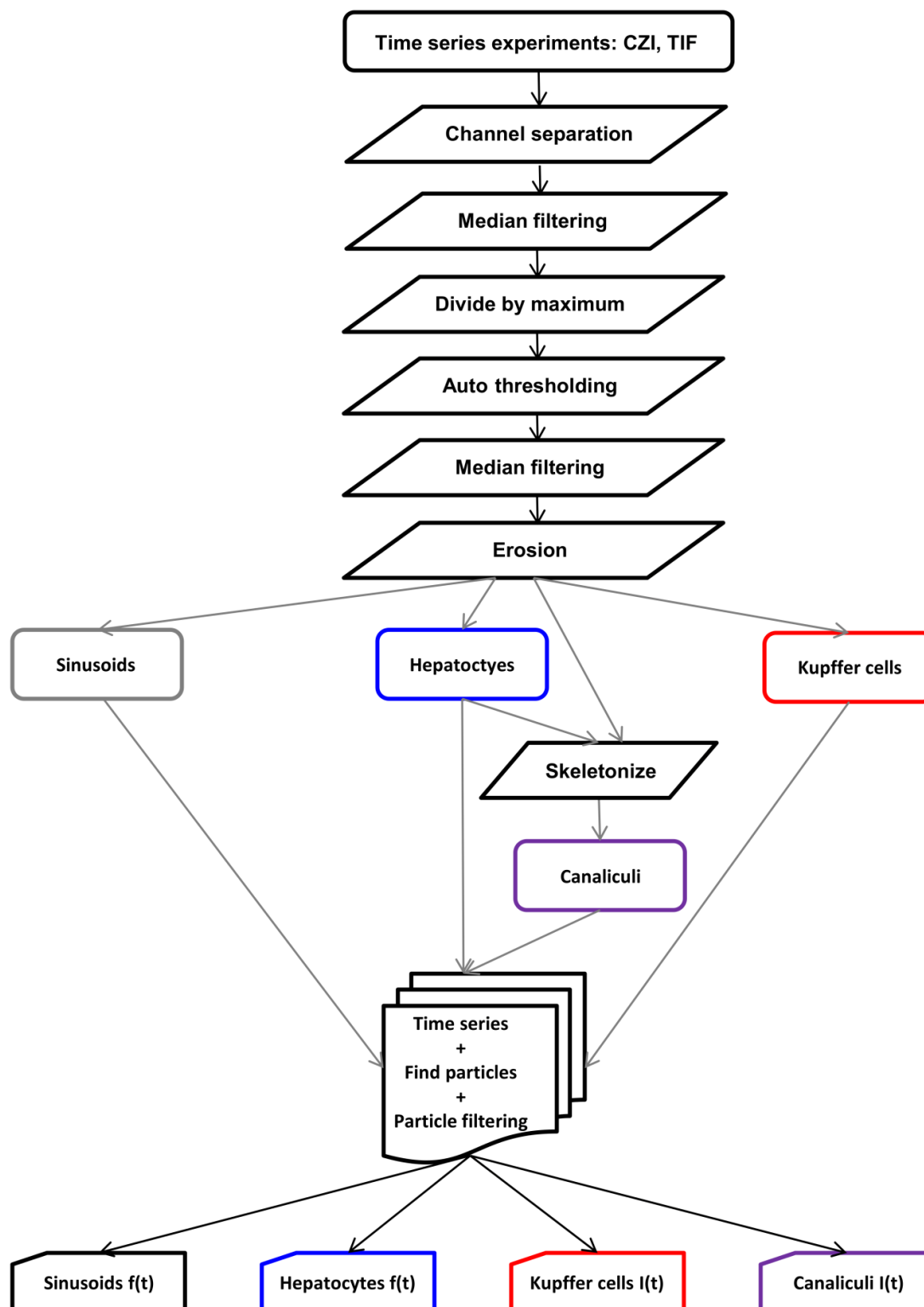
Figure A4 Flowchart of the automated image processing algorithm for time-series experiments. The workflow processed both CZI and TIFF-format microscopy images. The specifications of the applied algorithms (radii are in pixel units) were as follows: Median filtering: 5px; auto thresholding algorithm: Li; 2nd median filtering: 3px (Despeckle); erosion: 7px (sinusoids), 1px (hepatocytes, canaliculi), 2px (Kupffer cells).
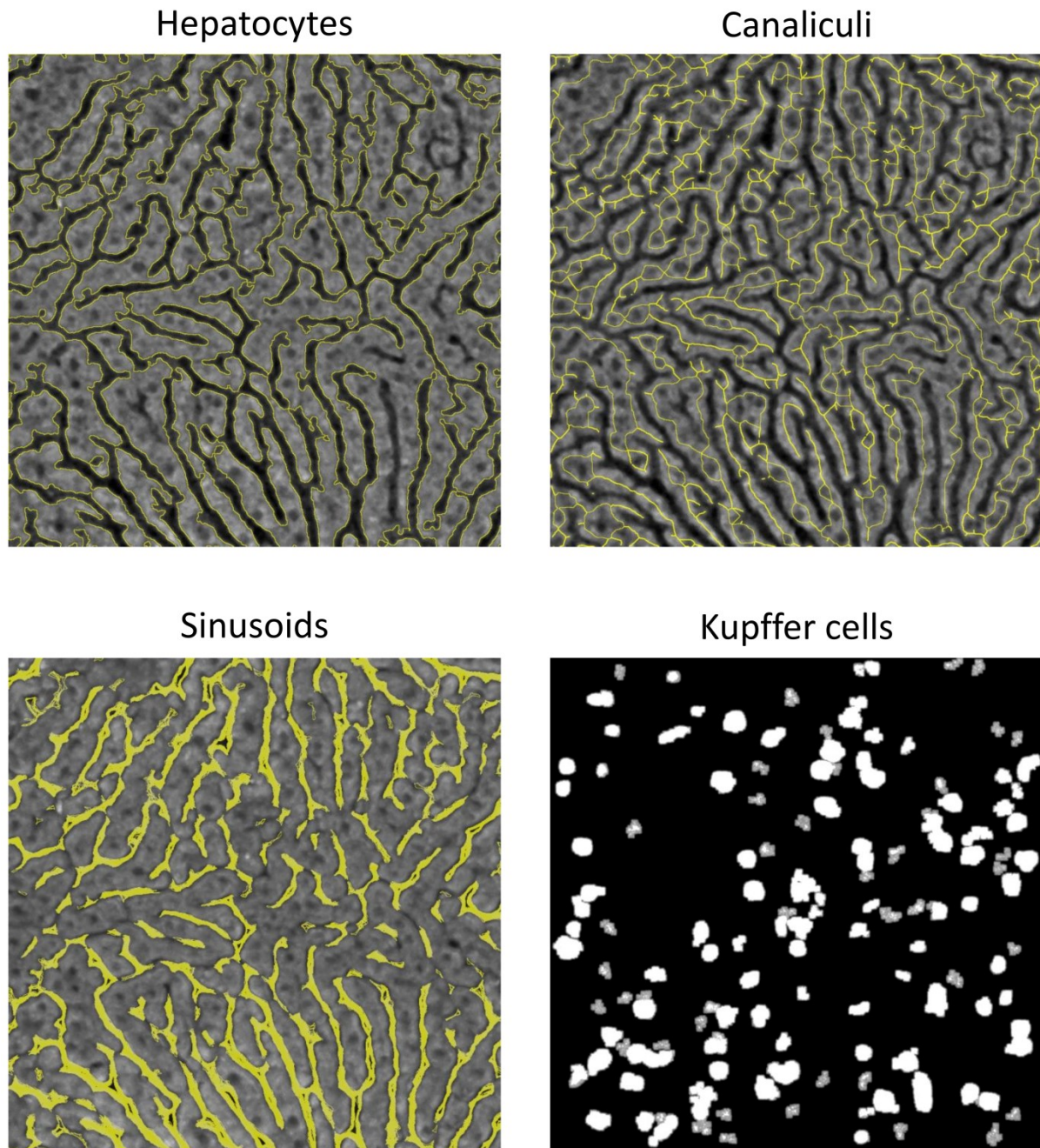
Figure A5. Representative images of the time series analysis workflow shown in Figure A4 applied on an image series from an EN15 dataset. The hepatocytes are outlined as 2D ROIs bordered by solid yellow line. The canaliculi are indicated with a 1 px broad yellow line as provided by a skeletonization algorithm. The individual snapshots of the sinusoids and canaliculi are from time frame 35 of the 47 total time points. The sinusoids are painted yellow based on the average projection of the segmented image's entire time series (47 time frames). The Kupffer cells are shown as maximum intensity projections of the entire time series.

<u>References</u>

1. Rueden, C. T.; Schindelin, J.; Hiner, M. C.; DeZonia, B. E.; Walter, A. E.; Arena, E. T.; Eliceiri, K. W., ImageJ2: ImageJ for the next generation of scientific image data. *BMC Bioinformatics* **2017,** *18* (1), 529.
2. Schindelin, J.; Arganda-Carreras, I.; Frise, E.; Kaynig, V.; Longair, M.; Pietzsch, T.; Preibisch, S.; Rueden, C.; Saalfeld, S.; Schmid, B.; Tinevez, J. Y.; White, D. J.; Hartenstein, V.; Eliceiri, K.; Tomancak, P.; Cardona, A., Fiji: an open-source platform for biological-image analysis. *Nat Methods* **2012,** *9* (7), 676-82.
3. Cseresnyes, Z.; Kraibooj, K.; Figge, M. T., Hessian-based quantitative image analysis of host-pathogen confrontation assays. *Cytometry Part A* **2018,** *93* (3), 346-356.

List of Figures

List of Tables

Ehrenwörtliche Erklärung

Hiermit erkläre ich, dass mir die Promotionsordnung der Medizinischen Fakultät der Friedrich-Schiller-Universität bekannt ist,

Ich die Dissertation selbst angefertigt habe und alle von mir benutzten Hilfsmittel, persönlichen Mitteilungen und Quellen in meiner Arbeit angegeben sind,

mich folgende Personen bei der Auswahl und Auswertung des Materials sowie bei der Herstellung des Manuskripts unterstützt haben:

- Prof. Dr. med. Michael Bauer, Jun-Prof. Dr. rer. nat. Adrian T. Press: Diskussion und Interpretation der Ergenniss, Redigieren der Dissertiation.
- Dr. Moritz Köhler, Dr. Carsten Rössel, Prof. Dr. Felix H. Schacher: Polymersynthese und Charakterisierung.
- Dr. Anuradha Ramoji: Raman Spektroskopie und Interpretation.
- Yingfeng Teng, Mingzhe Chi, Prof. Dr. Marek Sierka: DPD Simulation.
- Dr. Zoltán Cseresnyés, Prof. Dr. Marc Thilo Figge: Bildanalyse und Quantifizierung.
- Alexander Wiede, Sebastian Bierwirth, Dr. Walter Hauswald: Technisches Design, Konstruktion und Software Lösungen des Mesoskopie-Bildgebungssystems.
- PD. Dr. Stephanie Höppener: TEM Charakterisierung.

die Hilfe eines Promotionsberaters nicht in Anspruch genommen wurde und dass Dritte weder unmittelbar noch mittelbar geldwerte Leistungen von mir für Arbeiten erhalten haben, die im Zusammenhang mit dem Inhalt der vorgelegten Dissertation stehen,

dass ich die Dissertation noch nicht als Prüfungsarbeit für eine staatliche oder andere wissenschaftliche Prüfung eingereicht habe und

dass ich die gleiche, eine in wesentlichen Teilen ähnliche oder eine andere Abhandlung nicht bei einer anderen Hochschule als Dissertation eingereicht habe.

_____   _____
Ort, Datum   Unterschrift des Verfassers

Acknowledgement

Curriculum Vitae

WanLing FOO

Contact: +491628552143, wanling025@gmail.com

EDUCATION

Friedrich Schiller University Jena, Germany   *Dec 2017 - Present*
Ph.D of Molecular Medicine
Dissertation: Tuning the Corona: Core Ratio of Polyplex Micelles for Selective Oligonucleotide
Delivery to Hepatocytes or Hepatic Immune Cells

The University of Tokyo, Japan   *Oct 2013 – Oct 2015*
Master of Bioengineering
Thesis: Minimization of the polyplex micelle size for treatment of stroma-rich pancreatic cancer

Nanyang Technological University (NTU), Singapore   *Jul 2005 – Jul 2009*
Bachelor of Materials Science and Engineering
Thesis: Developing multilayered microparticles for sustainable drug release

PROFESSIONAL EXPERIENCES

Research Associate & Doctoral Degree   *Dec 2017 - Present*
University Hospital of Jena, Germany
DFG Research Training Group CRC 1278 PolyTarget.
Research on selective targeting gene delivery systems towards hepatocytes to restore critical
cellular signaling functions

Research Associate   *Jul 2016 – Oct 2017*
National University of Singapore, School of Medicine
Department of Obstetrics & Gynaecology
Working on the research of intrauterine haemopoietic stem cell transplantation.

Research Assistant   *Nov 2009 – Mar 2013*
Nanyang Technological University
Temasek Lab, Division of Advanced Materials
Responsible in the research & development of polymeric hybrid materials for the camouflage
military application and transparent display.

CERTIFICATES

FELASA-B
Humboldt University of Berlin, Germany
Certificate (Responsible Care and Use of Laboratory Animals), IACUC
National University Singapore

PUBLICATIONS

- *W. L. Foo et. al. Biomed. Opt. Express 2022, 13 (7), 3723-3742.*
- *T. A. Tockary, W. L. Foo et. al. ACS Nano. 2019 Nov 26;13(11):12732-12742*
- *M. Layani, P. Darmawan, W. L. Foo, et. al., Nanoscale, 2014.*
- *Y. Lu, W. L. Foo, et. al, J. Mat. Chem. C 2013, 1, 3651-3654.*
- *X. Wang, A. Sumboja, W. L. Foo, et. al., RSC Advances 2013, 3(36), 15827-15833.*
- *W. L. Lee, W. L. Foo, et. al., Acta Biomaterialia 2010, vol. 6, pp. 1342-1352.*

CONFERENCE PROCEEDINGS

- Controlled Release Society (CRS) Virtual Annual Meeting (2020) Poster
- ICYRAM (International Conference of Young Researchers on Advanced Materials) Singapore (2012), Poster
- 64th Symposium on Macromolecules, Japan (2015), Oral presentation
- Graduate School of Engineering Conference, The University of Tokyo, Japan (2015), Poster
- Bio-UT symposium, Tokyo Japan (2015)
- 25th Bio-macromolecules Symposium, Tokyo Japan (2015)

AWARDS

Master Fellowship Award   *Apr 2013 – Oct 2015*
AJINOMOTO® Postgraduate Scholarship, Japan 2013 (Recipient of Malaysia)

PERSONAL SKILLS

Language Proficiency

Mandarin Chinese   English   Malay   Japanese   German

Research Skills
- Data analysis (GNU R, Inkscape, ChemBioDraw, Origin, KaleidaGraph & etc.)
- Preclinical animal experiments (microinjection, IV & IP injection, aseptic surgery etc.)
- General molecular biological techniques (Western blot, PCR, ELISA, gene extraction)
- 2D and 3D Cell culture techniques (*in vitro*)
- Polymer synthesis, nanoparticles synthesis
- Physical properties characterization (TEM, cryo-TEM, FESEM, CLSM, DLS, DSC, etc.)